UNIVERSITÀ DELLA CALABRIA

UNIVERSITA' DELLA CALABRIA

Dipartimento di Ingegneria per l'Ambiente e il Territorie e Ingegneria Chimica - DIATIC

Dottorato di Ricerca in

Scienze e Ingegneria dell'Ambiente, delle Costruzioni e dell'Energia - SIACE

CICLO

XXXIII

TITOLO TESI

Theoretical Models for Membrane Capacitive Deionization for the design of Modular Desalination Processes

Settore Scientifico Disciplinare: CHIM06 – Chimica Organica

Coordinatore: Ch.mo Prof. Salvatore Critelli

Firma Firma oscurata in base alle linee guida del Garante della privacy

Supervisore/Tutor: Ch.mo Prof. Bartolo Gabriele Dott. Alberto Figoli

Firma Firma oscurata in base alle linee guida del Garante della privacy ma Firma oscurata in base alle linee guida del Garante della privacy

Prof. Dr.-Ing. Jan Hoinkis

Firma Firma oscurata in base alle linee guida del Garante della privacy

Dottorando: Ulrich Hellriegel

Firma Firma oscurata in base alle linee guida del Garante della privacy

UNIVERSITÀ DELLA CALABRIA

Dipartimento di Ingegneria per l'Ambiente e il Territorio e Ingegneria Chimica - DIATIC

Theoretical Models for Membrane Capacitive Deionization for the design of Modular Desalination Processes

Dottorato di Ricerca in
Scienze e Ingegneria dell'Ambiente,
delle Costruzioni e dell' Energia

by Ulrich Hellriegel

Supervisors:
Prof. Bartolo Gabriele[1],
Dr. Alberto Figoli[2],
Prof. Jan Hoinkis[3]

[1]Dept. of Chem. and Chem. Tech., University of Calabria (UNICAL), Arcavacata di Rende, Italy

[2]Research Institute on Membrane Technology (ITM-CNR), Arcavacata di Rende, Italy

[3]Karlsruhe University of Applied Sciences (HKA), Germany

Arcavacata di Rende, Italy / Karlsruhe, Germany,
November 2017 until April 2021

Typesetting and production:

LaTeX *with MiKTeX 2020 and TeXstudio 2.12.6*
Document class: *scrbook*
Font: *Computer Modern, 12 pt*; Type area: *DIV 15, BCOR 14 (print)*; Line spacing: *1.2*

Print Date \ Place: *December 8, 2021 , 2nd edition \ Karlsruhe, Germany*

Declaration

I hereby certify that I have written this thesis by myself, that I have not used any sources or aids other than those indicated, and that I have marked all passages in the thesis that have been taken over verbatim or analogously.

Karlsruhe, December 8, 2021

Ulrich Hellriegel

Acknowledgements

First of all, I want to thank my supervisors Prof. Bartolo Gabriele from UNICAL, Italy and Dr. Alberto Figoli from CNR-ITM, Italy, who brought to me the possibility to carry out these studies and attend in the PhD course as well as for helping me forming the subject and goals of the thesis and for their support in the laboratories on the UNICAL campus as well as for the help with the publications - Grazie mille!
Furthermore, special thanks to my supervisor Prof. Jan Hoinkis from HKA, Germany, who helped me throughout the whole project with any questions arising in laboratory work and writing the thesis. Prof. Thomas Westermann and Prof. Alessio Caravella, who supported me, especially in the beginning, to find a good access to the subject of theoretical modelling.

Moreover, I would like to thank my colleagues in my office, Sneha De, Ephraim Gukelberger, Talha Atiye and in remote office Tan Vu Luong, for the support, constant motivation and the creation of a very comfortable working atmosphere, especially Edgardo Cañas Kurz, my partner in the project, for the very helpful work related and off-topic discussions, it was and is a great pleasure to work with you in the same projects.

Particularly, I want to thank my wife Uiara, for being there, also in the very busy stages of the work, her great help and motivational words during my thesis work, which always cheered me up.
Additionally, I thank my family and friends, for their understanding and support during the whole PhD-time.

In the end, acknowledgments go to the Federal Ministry of Education and Research, Germany and the Karlsruhe University of Applied Sciences, which funded these studies.

'All models are wrong, but some are useful'

- George Edward Pelham Box

Abstract

Due to climate change, water scarcity will be exacerbated around the globe. To increase the water availability in regions at risk, water desalination plants can be a solution. Especially in rural areas, energy efficient technologies are needed so that an operation with renewable energy as photovoltaic modules can be feasible.
Recent publications showed that the novel technology *membrane capacitive deionization* (MCDI) can achieve a lower specific energy consumption (SEC) than reverse osmosis (RO), for brackish water desalination with salt concentrations below 2.5 $\mathrm{g\,L^{-1}}$.
There is still a gap in research between laboratory operation and applied commercial scaled desalination, regarding experimental but also theoretical model studies. Therefore the latter is elaborated in the present PhD thesis. Hereby, existing models are reviewed, adapted and further developed to fit to applied MCDI operation for drinking water production.
Two dimensional finite element methods (FEM) modelling of ion transport, according to the Gouy-Chapman-Stern theory for electrical double layers (EDL) as well as computational fluid dynamics (CFD) is combined with an adjusted semi-analytical modified Donnan (mD) model, with a constant excess chemical potential $\mu_{\mathrm{att}} = 2.33$ kT, for the electrosorption of ions into porous active carbon electrodes. It predicts the effluent salt concentration time-dependently for different inputs of applied electrical currents I_{cell} and voltages as well as inlet concentrations and volume flows. Applied MCDI operation was optimized for drinking water production with practical experiments, which support the evaluation of the theoretical findings. The model fits to experimental data for $I_{\mathrm{cell}} = 20\ A$, however the equations for the voltage over the electrodes need to be re-assessed so that the model fits for further input parameters.
A CFD model of the water flow through large scaled MCDI modules (> 50 pairs of electodes) shows the need of constructing spacer thicknesses δ_{Sp} small enough, to ensure equal retention times of the water between the electrodes in the module, which is important for stable diluate concentrations.
Furthermore, an analytical calculation tool is developed, by adjusting the mD model and introducing an effective salt adsorption capacity $\Gamma_{salt,\eta}$, to predict the maximum efficient charging time $t_{\mathrm{max,ch}}$, removal- and recovery rate as well as SEC values for optimized operation of applied MCDI processes. The model reaches an accuracy of 87% for the prediction of salt removal, 86% for $t_{\mathrm{max,ch}}$ and 75% for SEC values, compared with an experimental study and thus can be used to optimize the process design of applied MCDI desalination plants.

Contents

List of Figures

List of Tables

1 Introduction

1.1 Background and motivation

Clean water and sanitation is the sixth sustainable development goal of the United Nations (UN: The General Assembly, 2015), however a trend of water shortage can be seen worldwide (UNESCO, 2006). The salinization of groundwater due to the rising of the sea level and the following seawater intrusion does a big part to it. Well settled conventional membrane technologies as reverse osmosis (RO) give solutions to make it usable. More energy efficient desalination processes are highly wanted, so water treatment plants can be operated decentralized powered by renewable energy systems like photovoltaic and wind power generators.
Research work as reported by Zhao et al. (2013a) show that electrochemical treatment processes like capacitive deionization (CDI) have a lower energy consumption for desalinating water with a salt concentration of $c < 2.5\ \mathrm{g\,L^{-1}}$ than the classical RO. Porada et al. (2020) confirms this with theoretical calculations, assuming optimal CDI operational parameter are used. Hence, for brackish water this technology becomes very attractive. Water is desalinated by a CDI cell with its porous electrodes. Saline water is flowing by (or through) a pair of electrodes. After applying a low voltage ($U < 2$ V, DC), one electrode is positively the other negatively charged. Salt ions are attracted by the electrodes and are stored in their pores. The CDI behaves like a capacitor. In this charging phase, the effluent has a lower concentration of salt ions than the inflowing water. In a second step, the voltage has to be cut and the ions get released again. In this discharging phase, the effluent water is higher concentrated than the feed water (Porada et al., 2012). To improve the performance, ion exchange membranes (IEM) are placed in front of the porous electrodes (Zhao et al., 2013b). This technology is called Membrane Capacitive Deionization (MCDI). Now for the discharge phase, the voltage can be reversed without ions migrating into the opposite electrodes. Furthermore, the membranes help retaining the salt and inside the pores.

For a successful future design of water treatment plants including MCDI modules, computer based models are very helpful and are needed to be developed. There are existing finite element method (FEM) models for the flow by of the electrodes through the spacer, which describe the mass transport of the ions through the cell in behalf of diffusion, migration and convection (e.g. Hemmatifar et al., 2015). Jeon et al. (2011) introduces an FEM-model for the adsorption by the spacial resolution of single cavities as pores. Biesheuvel et al. (2011a) shows a model for the ion exchange membrane and for the porous electrodes in Biesheuvel et al. (2014), where simplification steps are used to avoid extensive computational resources and to find analytical solutions.

The state-of-the-art-models of MCDI cells, calculate the salt concentration in the single parts of the module (spacer, IEM, porous electrode) and energy consumption using different operational parameters. These models can reproduce the experimental data gained from tests from lab scaled MCDI plants. What is still missing is a holistic model which can predict the performance and energy consumption of large scale MCDI modules (for private or industrial applications) (Suss et al., 2015; Dykstra et al., 2016), to help designing water treatment plants for drinking water production or hardness reduction, where not only different dimensional scales but also different operation modes are applied.

1.2 Goals of the thesis

In order to close the gap between lab and applied MCDI operation with commercial scaled modules, following goals were set in the present PhD thesis:

- Practical experiments need to be carried out, which optimize applied MCDI operation and generate realistic data for the evaluation of the models
- existing models need to be reviewed, adjusted and adapted to fit applied MCDI experimental data
- the difference between lab scale and applied operation of MCDI need to be pointed out
- a calculation tool is to be developed, which allows the prediction of optimum operational parameters, salt removal, water recovery and specific energy consumption of the commercially applied MCDI process.

2 Fundamentals of desalination with membrane capacitive deionization

A salt like for instance sodium chloride (NaCl) is regularly dissociated in two ions when it is dissolved in water. The high permittivity of water (relative to vacuum or air, $\epsilon_{\text{Water}} = 78.3$) reduces the force needed holding the two ions together and they get dissolved in water by binding to the dipole of the molecule H_2O (Hamann and Vielstich, 2005). Therefore, salt in water is present as dissolved ions of a negative and of positive charge, bound to water molecules which build their hydration shell around the ion. Thus, a Na^+ ion has a bare radius of $r = 0.095$ nm and a hydrated radius of 0.36 nm (Israelachvili, 2011).
To remove salt from the water, different technologies can be used, with different types of energy input. To remove these very small ions with filtration, the most dense membranes are needed, like those in the reverse osmosis (RO) technology. Hereby, pumps which can apply high pressures are needed to work against the osmotic pressure, which develops with the concentration difference between the pure and concentrated volume.
Another approach is to remove the salt electrochemically (for instance with membrane capacitive deionization, MCDI), by attracting the charged ions with counter charged electrodes. Due to it is an electrical potential driven process this technique does not need high pressures, but has to put in an electrical charge to balance the charge density created by the salt ions.
Both technologies use membranes, although in MCDI it is not the main functional part in the process. In RO, water and in MCDI, ions are moved through the membrane. The fundamentals of the latter is summed up in the following sections.

Membrane capacitive deionization is an electrochemical desalination technology, in which salt ions are adsorbed by porous electrodes. The process is driven by an electrical potential and not by physical pressure as in conventional desalination technologies like reverse osmosis. Several pairs of electrodes are stacked together in series or parallel inside MCDI modules, through which the feed water is flowing. Thus the processes in this technology are based on electrochemical and fluid dynamical laws.

2.1 Electrochemical processes

The main electrochemical processes inside an MCDI module are ion movement caused by an electrical field and the development of the electrical double layer.

2.1.1 Electrical double layer

An electrical double layer (EDL) is shaped at the solid-liquid interface from electrode to electrolyte, if an electrical potential is applied at the electrode and thus getting negatively charged with electrons or positively with the absence of them (Probstein, 1994). The charged salt ions get attracted by the counter-charged electrodes, to balance the charge of its surface, a concentration of ions next to the carbon surface and thus the EDL is build up. It plays a significant role in modelling adsorption processes in an MCDI cell and thus needs to be elaborated further. The EDL can be described by the simplified HELMHOLTZ model or more detailed by the GOUY-CHAPMAN-STERN model (GCS) (Butt et al., 2006). The latter is pictured in figure 2.1.

It can be seen that also co-ions are present closer to the electrode, although the number of counter-ions is predominating. The GOUY-CHAPMAN-STERN model is considering the finite size of an ion. Thus, directly adjacent to the electrodes wall, the Stern layer is present. Closer no ion can move to the counter-charge in the electrode. The potential decrease from the solid interface over the Stern layer is linear. The further decline is approximately potential. In this diffusive layer the thermal voltage U_T can allow counter-ions to leave and co-ions to enter the layer at the distance λ_D, the DEBYE length. Theoretically, at absolute zero with the temperature $T = 0$ K only counter-ions would be present in the same amount of charge as the applied potential at the electrode. Thus λ_D is an indicator for the influence range of the EDL.

In the EDL, no charge neutrality is given and thus

$$\sigma = \sum_i z_i \cdot c_i \neq 0 \tag{2.1}$$

is valid, where σ is the charge density, z the valency and c the concentration of an ion species i.

In a mathematical expression the EDL can be described for example with the Poisson-

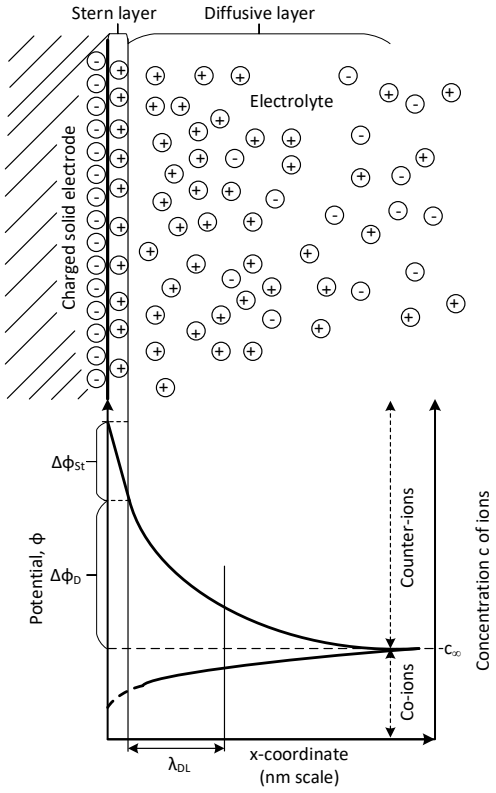

Figure 2.1. Schematic of the electrical double layer

Boltzmann equations (Butt et al., 2006) as follows:

$$\nabla^2\phi = -\frac{\sigma}{\epsilon_0\epsilon_r} \tag{2.2}$$

$$c_i = c_{i,\infty} \cdot e^{-W_i/(k_B T)} \ . \tag{2.3}$$

It applies that ϕ is the potential, $\epsilon = \epsilon_0\,\epsilon_r$ the permittivity of the dielectricum, c_∞ the concentration outside the EDL, W the work needed to move the ion towards the electrode and k_B the Boltzmann constant. The two equations combine the relation between electric potential and charge density (eq. 2.2) with the theory of Boltzmann statistics for the spacial distribution of ions in eq. 2.3. Eq. 2.2 can be changed in a one dimensional case and due to $\rho = z \cdot c$ to

$$\frac{d^2\phi}{dx^2} = F \cdot \frac{z\,c}{\epsilon} \ . \tag{2.4}$$

The potential energy of a mole of ions is (Hamann and Vielstich, 2005)

$$W = -F\,z\,\phi\ , \tag{2.5}$$

where F is the Faraday number. Combining eq. 2.4 and eq. 2.5, an equation for the energy needed to move an ion over the x-coordinate can be found as described by

$$\Delta W = -\frac{F^2\,z^2\,c\,x^2}{2\,\epsilon}\ . \tag{2.6}$$

The above mentioned Debye length λ_D can now be determined if ΔW is set equal to the thermal energy $R \cdot T$ (where R is the universal gas constant) per mole, defining the distance x from the electrodes surface where the thermal voltage is high enough, ions can escape the influence of the EDL (Probstein, 1994). This is described by eq. 2.7.

$$\lambda_D = \sqrt{\frac{\epsilon\,R\,T}{2\,F^2\,z^2\,c}} \tag{2.7}$$

The Debye length can be taken as a characterization of the EDL. Eq. 2.7 shows, that for example an increase in concentration leads to a decrease of the EDL size.

2.1.2 Ion mobility

In desalination processes the investigation of the ion transport is needed for theoretical predications of resulting parameters like the potential of salt removal and the energy needed for it. In conventional filtering technologies like reverse osmosis, the movement is based on a balance between osmotic and applied pressure. In desalination with MCDI, the driving gradient is the electrochemical potential and the induced electrical field. The magnitude of attraction of a charged ion depends on its mobility and is mainly divided in diffusion and migration.
The ion mobility u in a infinite diluted solution is defined as a specific velocity of ions in an electrical field, without its magnitude and given by for instance Hamann and Vielstich (2005) as

$$u = \frac{z\,e_0}{6\,\pi\,\eta\,r_1}\ , \tag{2.8}$$

where e_0 is the elementary charge, η the viscosity of the solvent, and r_1 the radius of the ion. If the mobility is multiplied by the strength of the electrical field E, it results

in the drift velocity v of the ion. Eq. 2.8 results from the balance of forces on a moving ion. On the one hand the driving electrical force ($z\,e_0\,E$) and on the other the breaking STOKES friction force ($6\,\eta\,r_1\,v$) on spheres. The velocity in m s^{-1} of the ions can also be expressed as a mass flow $\dot{m}$ in kg s^{-1} or a molar flow $\dot{n}$ in mol s^{-1}. The specific molar flow depending on the cross section is the flux J in mol m^{-2} s^{-1}.
It can be seen that the mobility is dependent on the radius of the ion or on the hydrated radius respectively. The ion velocity is furthermore proportional to its conductivity κ and its induced electrical current I. The molar conductivity of an electrolyte solution ξ_m hence is (Hamann and Vielstich, 2005)

$$\xi_\mathrm{m} = \frac{\kappa}{c} \ . \tag{2.9}$$

It has to be mentioned, that κ is changing non-linearly with the concentration of a solution. Firstly, with higher concentrations, κ is increasing. This can be derived from the definition of the electrical current:

$$I = \frac{dq}{dt} = A\,e_0\,N_\mathrm{A}\left(\sum_i z_i\,c_i\,v_i\right) \ , \tag{2.10}$$

with N_A being the AVOGADRO constant. The definition explains I as the change of charge q per time t, which can be also described as an amount of ions $c_i \cdot N_\mathrm{A}$ moving through a reference area A with the speed v. This equation shows that I and thus the electrical conductivity needs to increase with higher concentrations c.
After firstly increasing for all salts, for some compounds it is possible it decreases with higher concentrations again (see figure 2.8 in Hamann and Vielstich, 2005, p. 20), due to stronger electrostatic attraction forces K in between ions, resulting from the COULOMB's law:

$$K = \frac{q_1\,q_2}{\epsilon\,r^2} \ , \tag{2.11}$$

where both, higher valency and higher concentration increases the charge q and thus also the inter ion attraction force, which decreases the mobility of the ions and hence also the electrical conductivity.

The reciprocal of the conductivity, together with the volume of the electrolyte is representing the resistance of the electrolyte, which further plays a role for the energy demand of the system.

The ion mobility is leading to two different kinds of ion transport. Through

1. diffusion (due to a concentration gradient)
2. electromigration (due to an electrostatic potential gradient).

2.1.3 Ion transport through diffusion

According to the first law of FICK, the flux is reversed proportional to the concentration gradient by a factor D, which is the diffusion coefficient, following eq. 2.12

$$J = -D\nabla c \ , \tag{2.12}$$

since the Boltzmann statistics (Butt et al., 2006) reveal that ions are more likely moving towards lower concentrations ($\nabla c < 0$). Hence the diffusion coefficient D describes the strength of ion movement in between concentration differences similar to the conductivity in for example heat transfer problems.
Another description of the diffusion coefficient was made by EINSTEIN and SMOLUCHOWSKI by defining

$$D = u\, k_\mathrm{B}\, T \ . \tag{2.13}$$

Combining this equation with eq. 2.8 and q being the electrical charge of an ion ($z\, e_0$), results into

$$D = \frac{u\, k_\mathrm{B}\, T}{q} = \frac{k_\mathrm{B}\, T}{6\, \pi\, \eta\, r_1} \ , \tag{2.14}$$

which is called the STOKES-EINSTEIN-equation (Probstein, 1994) and highlights the relation of ion mobility and diffusion.

2.1.4 Ion transport through electromigration

As for diffusion, the gradient of concentration results in ion transport. A gradient in electrical potential $\nabla\phi$ causes ion movement as well. The force affecting the ion can be defined as its charge times the negative electrical potential gradient ($-z\, F\, \nabla\phi$) (Probstein, 1994). Like for the transport through diffusion, the flux is proportional to the force with a factor u, the mobility of the ion and thus

$$J = -u\, z\, F\, c\, \nabla\phi \ . \tag{2.15}$$

The movement of ions is inducing an electrical current $I = F \sum_i z_i J_i$ and if no concentration gradient is present, this results in

$$I = -\kappa \nabla \phi, \quad \text{with} \quad \kappa = F^2 \sum_i z_i^2 u_i c_i \ , \tag{2.16}$$

where κ is the electrical conductivity of the solution (Probstein, 1994).

The equations for diffusion and electromigration are part of the NERNST-PLANCK-equation, which is used in this thesis for theoretical modelling (see sec. 3.3.1).

2.1.5 Faradaic reactions

In an electrochemical system where electrodes are present, faradaic reactions are taking place, thus as well in MCDI technology (Zhang et al., 2018). Mostly unwanted, they can decrease the overall efficiency and lifespan of an MCDI cell. The main salt removal process happens through non-faradaic ion adsorption in the EDL, especially when active carbon electrodes are being used (see sec. 2.3). Nevertheless, faradaic pseudocapacitance effects contribute to store the ions and thus can also enhance the efficiency. Hence, faradaic reactions can be harmful or advantageous to the desalination process. These reactions take place at the electrode-electrolyte-interface, when applied electrical potentials plus the overvoltage locally exceed the standard electrode potential E° of the reacting element, relative to the standard hydrogen electrode (SHE). In table 2.1, possible faradaic reaction inside an MCDI cell are listed (Zhang et al., 2018). The oxidation and reduction reactions at the anode and cathode respectively, are decreasing the desalination efficiency, by using the electrical charge without any adsorption of salt ions. At the anode itself it is the carbon oxidation of the electrode, which is taking place at a low potential of $E^\circ = 0.21$ V already and thus in the normal operational range of MCDI cells. This is affecting the lifespan of each electrode. The oxidation of HClO (product of potential Cl^- oxidation) to ClO_3^- does need a low potential as well. However, before this hypochlorous acid is present, the oxidation of chloride ions need to happen firstly, which needs higher potentials. More of a problem can become the water oxidation, with $E^\circ = 1.23$ V. Due to this is the thermodynamical value and no overpotential is yet added, electrodes can be applied with potential up to $U = 1.5..1.6$ V that no oxygen is created (Hamann and Vielstich, 2005). The carbon reduction at the cathode was up to date not confirmed conclusively (Zhang et al., 2018) and thus no E° is known yet.

Table 2.1. Faradaic reactions inside and MCDI cell

Faradaic reactions

Electrode	**Reaction**	E° in V / SHE
Anode	C→COOH (Carbon oxidation)	0.21
	Cl^- →HClO (Chloride oxidation)	1.36
	HClO→ClO_3^- (Chloride oxidation)	0.64
	H_2O→O_2 (Water oxidation)	1.23
Cathode	O_2→H_2O_2 (Oxygen reduction)	0.69
	O_2→H_2O (Oxygen reduction)	1.23
	C→CH (Carbon reduction)	-

Faradaic ion storage - pseudocapacitance effects

Electrode	**Reaction**	E° in V / SHE
Anode (Ag)	Ag+Cl^-↔AgCl (Cl^- capture)	-
Anode (BiOCl)	Bi+Bi_2O_3+Cl^-↔BiOCl (Cl^- capture)	-
Cathode ($Na_{0.44}MnO_2$)	$Na_{0.44-x}MnO_2$+Na^+↔$Na_{0.44}MnO_z$ (Na^+ capture)	-
Cathode ($Li_xMn_2O_4$)	$Li_{1-x}Mn_{1-x}^{III}Mn^{IV}O_2$+Li↔$LiMn^{IV}Mn^{III}O_4$ (Li capture)	-

If no active carbon electrodes are used in MCDI (see sec 2.3) faradaic pseudocapacitance effects can occur at the electrodes. For instance Cl^- ions can be intercalated by silver- or Na^+ by sodium manganese oxide electrodes. By using both, active carbon and so called faradaic electrodes, the salt adsorption capacity (SAC) can be strongly increased (Suss et al., 2015). However is the fabrication of such more complicated and thus cost intensive (Zhao et al., 2020).

2.2 Fluid dynamics

On a larger scaled prospect, the water flow through the MCDI module can be described with classical fluid dynamics. Depending on the complexity of the geometrically arrangement of electrodes inside an MCDI module, the volume flow of a solution through it can be inhomogeneous and thus feed the electrodes with a different amount of salt. To investigate the influence of different module geometries on the salt removal, some

fundamental fluid dynamics have to be defined for a later application in theoretical models.

As the salt is completely dissolved in water, it is a liquid consisting of one phase. A single-phase flow can be divided into compressible and incompressible flows. Since in the case under investigation a liquid is considered and no large changes in temperature, pressure and velocity are to be expected in the space under consideration, this is an incompressible flow. This means that the density of the fluid remains constant during the entire observation period. With an incompressible flow, the volume flow $\dot{V}$ always remains constant. This can be calculated from the cross sectional area A and the average speed $\bar{c}$ prevailing (Bohl and Elmendorf, 2014), as stated in following equation:

$$\dot{V} = A \cdot \bar{v} \tag{2.17}$$

Furthermore, a distinction can be made between two further flow forms, a laminar and a turbulent flow. At low flow velocities v the flow usually has a small REYNOLDS number:

$$Re = \frac{v \cdot L}{\nu} \tag{2.18}$$

where ν is the kinematic viscosity and L is the characteristic length or hydraulic diameter (for a pipe flow its diameter) of a flow geometry. If it is assumed that the cross section of the spacer in between the electrodes is rectangular, a different L according to eq. 2.19 needs to be determined.

$$L_{\text{rect}} = 2 \cdot \frac{h \cdot b}{h + b} \ , \tag{2.19}$$

where h and b are the side lengths of the rectangular. For small gaps between two parallel plates, where $\lim_{b \to \infty}$ can be assumed (Bohl and Elmendorf, 2014, p. 232), L changes to

$$L_{\text{gap}} = 2 \cdot h \ , \tag{2.20}$$

with h being the distance between the plates. In this thesis, this assumption is used if $L_{\text{rect}} \approx L_{\text{gap}}$.

If the REYNOLDS number is smaller than the critical REYNOLDS number

$$Re < Re_{\text{crit}}, \tag{2.21}$$

it is a laminar flow (Bohl and Elmendorf, 2014). Then the layers of the water current, flow side by side without exchanging fluid particles. If the REYNOLDS number is higher than the critical REYNOLDS number, it occurs a turbulent flow. There is a large ex-

change of fluid particles between the layers and the flow carries out irregular crosswise movements and turbulence. It is $Re_{\text{crit}} = 2320$ for a pipe flow and $Re_{\text{crit}} = 3 \cdot 10^5$ for flows over a flat plate (Boeswirth and Bschorer, 2012; Schlichting and Gersten, 2006, p. 176 and p. 12 respectively).
A water flow between electrodes in an MCDI cell, can as well be pictured as a flow in between two plates, if the cross section can be considered as rectangular with the width being much longer than the height (see eq. 2.20). In this case $2200 < Re_{\text{crit}} < 3600$ is valid (VDI-Gesellschaft, 2013, p. 820).

The velocity of a flow is zero directly next to the boundary. Towards more distant layers from the wall, the flow speed increases parabolically; for a turbulent much quicker than for a laminar flow. This means that close to the wall, there are changes in velocity from one flow layer to the next.
Another important differentiation is that, between a stationary and a transient flow. In the case of a stationary flow, the track of it is not dependent on time. This is always the case with a single-phase flow, as long as all external influence parameters are not changed in the period under consideration.
As the salt ions move independently from the water in different spacial dimensions, the flow can be seen as a two-phase flow and thus as time dependent. However, in this study the simulation of the fluid flow serves as a transport model for the ions and thus for the convective part of their movement. This is again a time independent problem and subsequently the modelling of the fluid flow can be simplified as a single-phase flow.

2.3 Materials

In fig. 2.2, the main parts of a membrane capacitive deionization-cell are illustrated. The electrodes are the most significant of them and responsible for the desalination, thus as well the object with the main research focus in the field of CDI (Zhao et al., 2020). The working medium is either flowing by (fig. 2.2 a-c) or through the electrodes (fig. 2.2 d). MCDI cells are built up of porous electrodes (mostly consisting out of active carbon) with mounted cation exchange membranes in front of the cathode and anion exchange membranes vice-versa. The two electrodes are divided by a woven spacer, which allows the water flow by the electrodes in *flow-between electrodes* setup (fig. 2.2 a-c) of a MCDI cell (Suss et al., 2015). Another option is the *flow-through electrodes* principle (fig. 2.2 a-c) in which the water flows orthogonally and through the stacked electrodes. Here, no

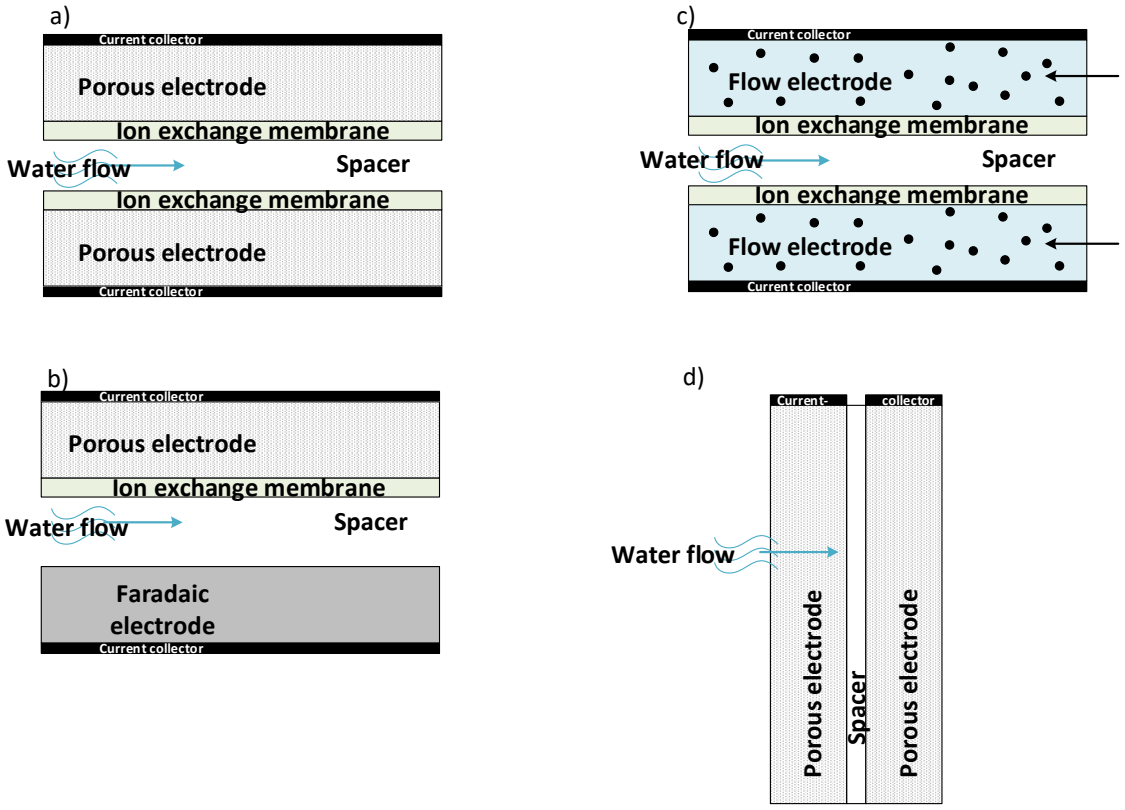

Figure 2.2. Different setups for electrodes and ion exchange membrane for MCDI applications. a)-c) flow-by principle, d) flow-through principle

ion-exchange membrane (IEM) can be used and this principle is therefore not longer considered in this thesis. The principle of the *flow-between electrodes* is subsequently also called *flow-through the MCDI cell*.

The mounting of IEMs enhances the desalination significantly compared to the former capacitive deionization (CDI) technology (see section 2.4). The electrodes are divided by a spacer (Porada et al., 2012), which separates the electrical charges and builds the channel for the water flow.

2.3.1 Electrodes for CDI

The adsorption effect inside CDI and MCDI cells, is depending on the electrodes used. They are mainly made up of porous active carbon, where EDLs are formed in the pores (Zhao et al., 2020; Suss et al., 2015). The distribution of macro-, meso- and micropores (with widths of $b > 50$ nm, $b = 2 - 50$ nm and $b < 2$ nm respectively) are

hereby defining the efficiency of desalination (Han et al., 2014; Porada et al., 2013). Due to the small width of micropores smaller than the usual Debye-length of the EDLs (see fig. 2.1), they are practically overlapping, which can hinder the further desorption process (Zhao et al., 2020). However, this is where the main part of ion adsorption takes place (Porada et al., 2012).
The used materials for electrodes can be categorised in (Zhao et al., 2020)

- electrostatic double-layer capacitors (EDLC)
- pseudocapacitors / faradaic electrodes
- flow electrodes.

The EDLCs adsorb the ions in their electrical double layer and are the most used electrodes for MCDI (Zhao et al., 2020). The disadvantage is that only desalination of low saline water is possible, however they are cheaper to produce and there is a high availability on the market. The storage amount is not as high as with pseudocapacitors. The ratio micropores / mesopores is higher for active carbon than for mesoporic carbon (Tsouris et al., 2011). The higher the micropore fraction, the higher the increased active surface due to porosity, however the slower the adsorption and desorption of the ions. Thus the optimized ratio in microporosity plays a significant role in EDLCs (Han et al., 2014).
Pseudocapacitors store the ions through faradaic charge transfer and not through capacitance effects (Suss et al., 2015). Like this, the ion does not have a direct bound to the electrode but is adsorbed due to a change in its charge through faradaic reactions. Hence, they are also called faradaic electrodes (Pasta et al., 2012). They consist of metallic layers coated on carbon (Wang et al., 2018b; Li and Park, 2018), MXene (Srimuk et al., 2016; Naguib et al., 2013) or Prussian blue analogues (Lee et al., 2017). The best adsorption efficiency is reached by hybrid systems using capacitive EDLCs together with faradaic electrodes (Suss et al., 2015).
Another option is to use flowing electrodes (Kastening, 1988) like in the flow capacitive deionization (FCDI) technology (see fig. 2.2 and Jeon et al. (2013)). Here the electrodes consist of a slurry like liquid, a solution with carbon particles, which is able to be pumped. With these electrodes, salt ions can be adsorbed continuously with a higher adsorption rate per time, but the electrode liquid needs to be treated in a second remediation cell. Thus this technology shows similarities to electrodialysis (Tanaka, 2015a).

2.3.2 IEMs and spacer for MCDI

The other two main functional parts in MCDI are the ion-exchange membranes and the spacer.
The IEMs are crucial for the enhancement of desalination efficiency by capacitive deionization. They are attached directly on top of the electrodes (see fig. 2.2) and hinder co-ions to pass through. Thus less co-ions are stored in the pores of the electrodes, which increases the efficiency while desalination and regeneration of the electrodes (see section 2.4). In the regeneration phase, the IEMs hinder the ions of being adsorbed at the counter electrode on opposite site. This increases the regeneration phase and less water is needed to flush out the ions, which subsequently rises the η_{vol} (eq. 2.22). With a higher recovery rate, more product water can be created, which again decreases the specific energy consumption *SEC* measured as used energy in kWh per produced m^3 of product water (Ramachandran et al., 2019).
The main structure of IEMs is mostly made up of styrene copolymers (Tanaka, 2015b). For cation exchange membranes (CEM), negatively charged groups like sulfonic acids, phosphonic acids or phenolic hydroxide groups are fixed on the framework. Now positively charged ions can pass and negatively charged are rejected by the membrane barrier. For anion exchange membranes (AEM), ammonium or phosphonium groups are used (Vogel and Meier-Haack, 2014).

Spacers separate the two electrodes from each other and allow a water flow next to them. The preferred material used is a woven mesh of nylon or glass fibre (Zhao et al., 2012; Han et al., 2014; Fritz et al., 2019). Recent studies by Lado et al. (2021) show experiments, using spacer frames, which keep the most of the gap empty and force the water on pre-simulated optimized streamlines.

2.4 Desalination process

The desalination with capacitive deionization is other than to the salt removal with conventional membrane technologies, no pressure driven process. In section 2.3 several types of CDI technologies have been introduced. The work of this thesis is focused on the commercially most occurring version and thus in applications most used one, the membrane capacitive deionization with active carbon electrodes and the flow-by-the-electrodes principle (fig. 2.2, a).

In different spacial scales, different processes can be observed. For a modelling approaches, these has to be taken into account and it needs to be evaluated, which scale and which processes are essential and which can be omitted.

2.4.1 Medium scale - working principle

In this thesis, the scale where the main processes are taking place, is defined as the medium scale. Here the main processes take place which define the desalination steps and needs to be investigated first.
The desalination with the MCDI cell (fig. 2.2, a) is conducted in two alternating steps and illustrated schematically in fig. 2.3. Water flows between the electrodes while a

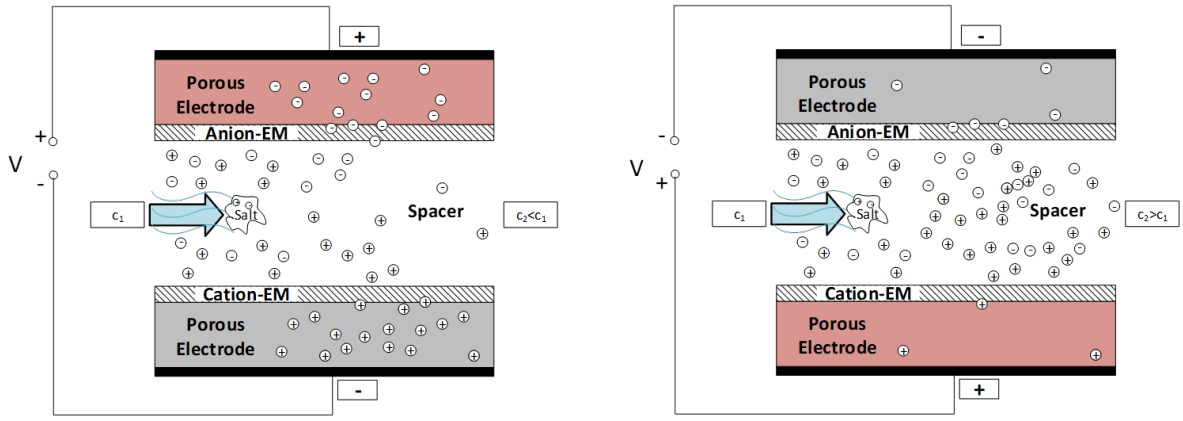

Figure 2.3. The principle of desalination with MCDI. Left, desalination; right, regeneration

voltage is applied to the cell and one electrode gets positively the other negatively charged. Salt ions are attracted by the electrodes and are stored in their pores. The CDI behaves like a capacitor. In the charging phase, the effluent has a lower concentration of salt ions (diluate) than the inflowing water (feed). After the porous electrodes are fully charged and no further salt can be adsorbed, they need to be discharged in a regeneration process. Hereby, the voltage has to be cut and the ions get released. In this discharging phase, the effluent water is higher concentrated (denoted as concentrate) than the feed water (Porada et al., 2012). This process is called 0V-discharge. To speed up this phase, especially in CDI with attached IEMs (MCDI), the voltage can also be reversed (rV-discharge). Now the IEMs hinder the ions to adsorb in the opposite electrode instead.

In this way, less water is lost during this regeneration step and the recovery rate

$$\eta_{\mathrm{vol}} = \frac{V_{\mathrm{dil}}}{V_{\mathrm{tot}}}, \quad \text{with} \quad V_{\mathrm{tot}} = V_{\mathrm{dil}} + V_{\mathrm{conc}} \tag{2.22}$$

is increased. Hereby, V_{dil} is the volume of the diluate, V_{conc} of the concentrate and V_{tot} is the total volume.
Not only in the discharge phase but also during desalination, the IEMs increase the efficiency of the process by not letting pass the co-ions for each electrodes. Hence, the co-ions do not affect the charge inside the adsorbing pores and the applied voltages on the electrodes can be used solely used for ions attraction. Thus, by applying IEMs in front of the electrodes in CDI increases the overall efficiency of the desalination process (Zhao et al., 2013b).

The desalination process can be operated in constant voltage (CV) or constant current (CC) mode. The main difference is the desalination behaviour (effluent salt concentration over time), which is constant during the charge phase at CC operation due to a constant electrical current forces a constant salt adsorption rate. If CV operation is applied, the salt adsorption rate is not constant and thus the effluent salt concentration characteristics show a peak. Hence the CC operation is used if a constant product quality in the effluent stream is pursued.
Furthermore, Qu et al. (2016) shows that the CC operation in a flow through CDI cell (fig. 2.2, d) bears a lower energy consumption than a CV operation. Dykstra et al. (2018) presents with a validated model that the energy consumption of both are the same, nevertheless if the principle of energy revocery is used (Długołęcki and van der Wal, 2013), the CC mode is more energy efficient.

2.4.2 Small scale processes

In a small scale, processes inside the pores of the electrodes are observed. There are different ion transport phenomena, which are influencing the efficiency of the desalination. Like mentioned in section 2.1, ions are transported by diffusion and electromigration into the porous electrodes and through the mesopores of the active carbon. Here the ions are adsorbed in the EDLs (section 2.1). Although IEMs are mounted in front of the electrodes, a small co-ion leakage is usual in MCDI applications (Zhao et al., 2013b) and thus they also appear in the adsorption material. Subsequently not only different

counter-ion adsorption, but also co-ion expulsion events are taking place inside the micropores (Suss et al., 2015). Here, the ionic charge density (eq. 2.1) needs to balance the charge density in the electrode. In other words, for every electron migrating inside the electrode towards the electrode-electrolyte-interface, a counter-ion needs to migrate into the micropore towards the interface inside the electrolyte from the other side as well. Alternatively, a co-ion can move out of the micropore to balance the charge (see fig. 2.4). Especially on low voltages or high ion concentrations, first the co-ions are

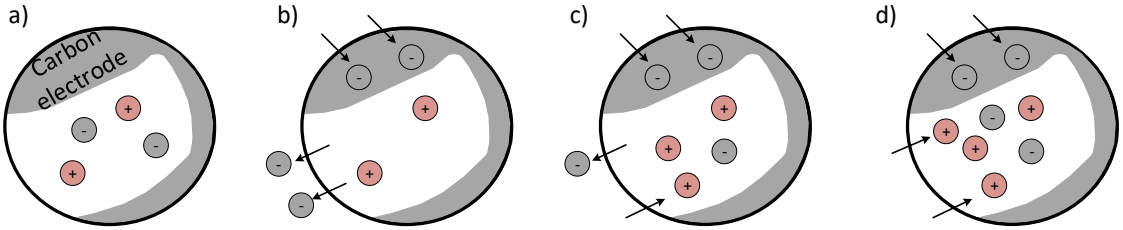

Figure 2.4. Schematic of micropore charge balance events

expulsed from the micropores instead of counter-ions are adsorbed (Deschamps et al., 2013), which does not contribute to the desalination (fig. 2.4, b or c). Only after all co-ions are pushed out of the pores, the full input of electrons (electrical charge) can be transferred into desalination performance. This occurrence plays a major role in the desalination efficiency of an MCDI module. For its description, the most important parameter is the charge efficiency Λ, which is defined as the ratio of the electrical charge input Q (in the units $\mathrm{A} \cdot \mathrm{s} = \mathrm{C}$) and the ions attracted in mol, times the Faraday-number, which is an electrical charge equivalent in C:

$$\Lambda = \frac{Q}{n\,F}\ , \tag{2.23}$$

where Q is the electrical charge and n the molar amount of substance. The total amount of adsorbed ions per gram of electrode during a charge phase (salt adsorption capacity, SAC) is defined by Γ_{salt} in $\mathrm{mg\,g^{-1}}$. The total electrical charge per weight of electrode is Σ in $\mathrm{C\,g^{-1}}$ and thus the charge efficiency can also be expressed as

$$\Lambda = \frac{\Gamma_{\mathrm{salt}}}{\Sigma}\ . \tag{2.24}$$

2.4.3 Large scale - technical application

Considering a larger scale, MCDI pairs of electrodes (cells) are combined in parallel or in series to form an MCDI module. Hereby, also constructive limits determine the general structure. The geometry designed, determines the flow of the saline water through the cells. A good design holds a low pressure drop Δp through the module and distributes the water in equal amounts to several cells. The latter is important as it defines the amount of ions each electrode is fed with. Material and operational parameters are mostly the same for every pair of electrodes. Thus the highest efficiency of desalination can be reached with an equal distribution of feed water. At large scale, except of diffusion and migration of ions (section 2.1), also the convection of ions (section 2.2) needs to be considered.
Commercial producers offer radial and rectangular stacked solutions (see fig. 2.5). The electrical connection of the several modules, plays a role for the applicable voltage which can be used. For each pair of electrodes, the voltage of $U = 1.5\,\mathrm{V}..1.6\,\mathrm{V}$ should not be exceeded, to prevent water electrolysis (see 2.1). With a parallel electrical connection the summed up applied voltage can be higher than U_{We}, which can be advantageous for the efficiency of their power supply. Furthermore, an increasing number of modules can produce more desalinated water per time.

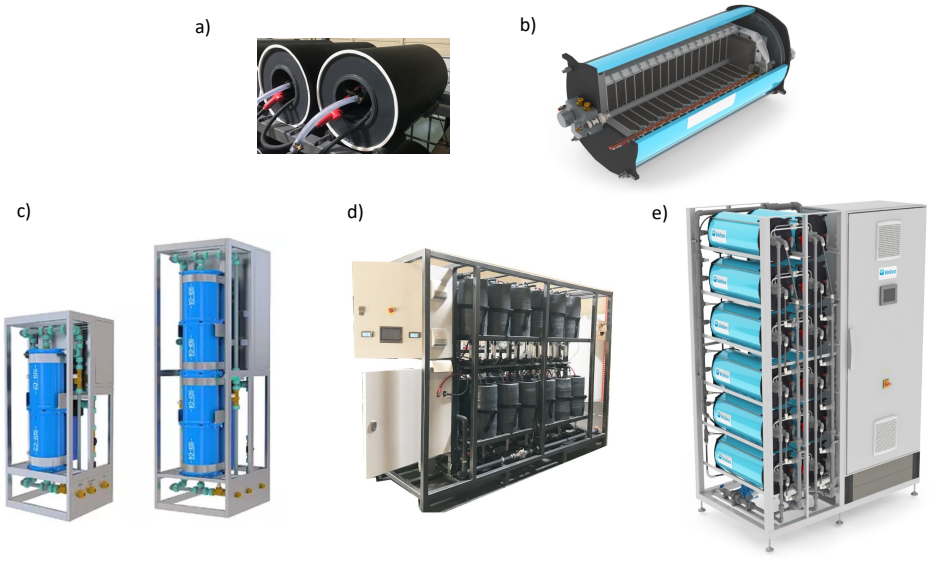

Figure 2.5. Applied geometries of commercial MCDI modules. a) Atlantis Technologies - USA, single radial module b) Voltea Inc. - USA, cut of single module c) Siontech co., Ltd. - Korea, combined systems d) Antlantis Technologies - USA, combined radial system in industrial scale e) Voltea Inc. - USA, combined industrial system (all pictures ®by each company)

3 Fundamentals of model building

Creating theoretical models for technical applications is necessary for their design, so constructive and operational parameters can be defined before the actual device is built. Another advantage of computer-based models is that more complex and oversized geometries can usually be modelled faster, than a test rig can be set up with a real model. After the calculation with a simulation algorithm, the results must be validated and compared with the real case. Subsequently, changes and adaptions in geometry or in boundary conditions (BC) are more easily and quickly made during the simulation phase than at a real model.
Modelling of physical phenomena is following a given procedure, which is schematised in fig. 3.1. Theoretical models are described with mathematical equations, which are derived from physical conditions and are valid for certain parts in the application. They need to be traced out and their boundaries defined, which again have certain fixed conditions, in a shape of constant values, variables or derivatives. These single parts are also called domains Ω, in which the equations are valid. At the boundaries, where the in- and output parameters are set, the results can be transferred into a neighbouring domain, where different conditions and physical models are defined (e.g. Westermann, 2010).

A crucial step while defining the physical conditions is to define, which one will influence the result and which can be omitted. This will determine the quality of the results as well as the feasibility and time needed to solve the equations. The more simple a physical system can be described the less mathematical equations need to be used. On the one hand this can mean that a before impossible to solve equations system can be calculated and the calculation times are reduced. On the other hand, it can lead to getting wrong or low quality results, which cannot be further processed or even conclude in false assumptions for the technical system.
The simplification process has to be done also for defining the domain and its boundaries, when the simulation is extended in spacial dimensions. Hereby, the same rule applies,

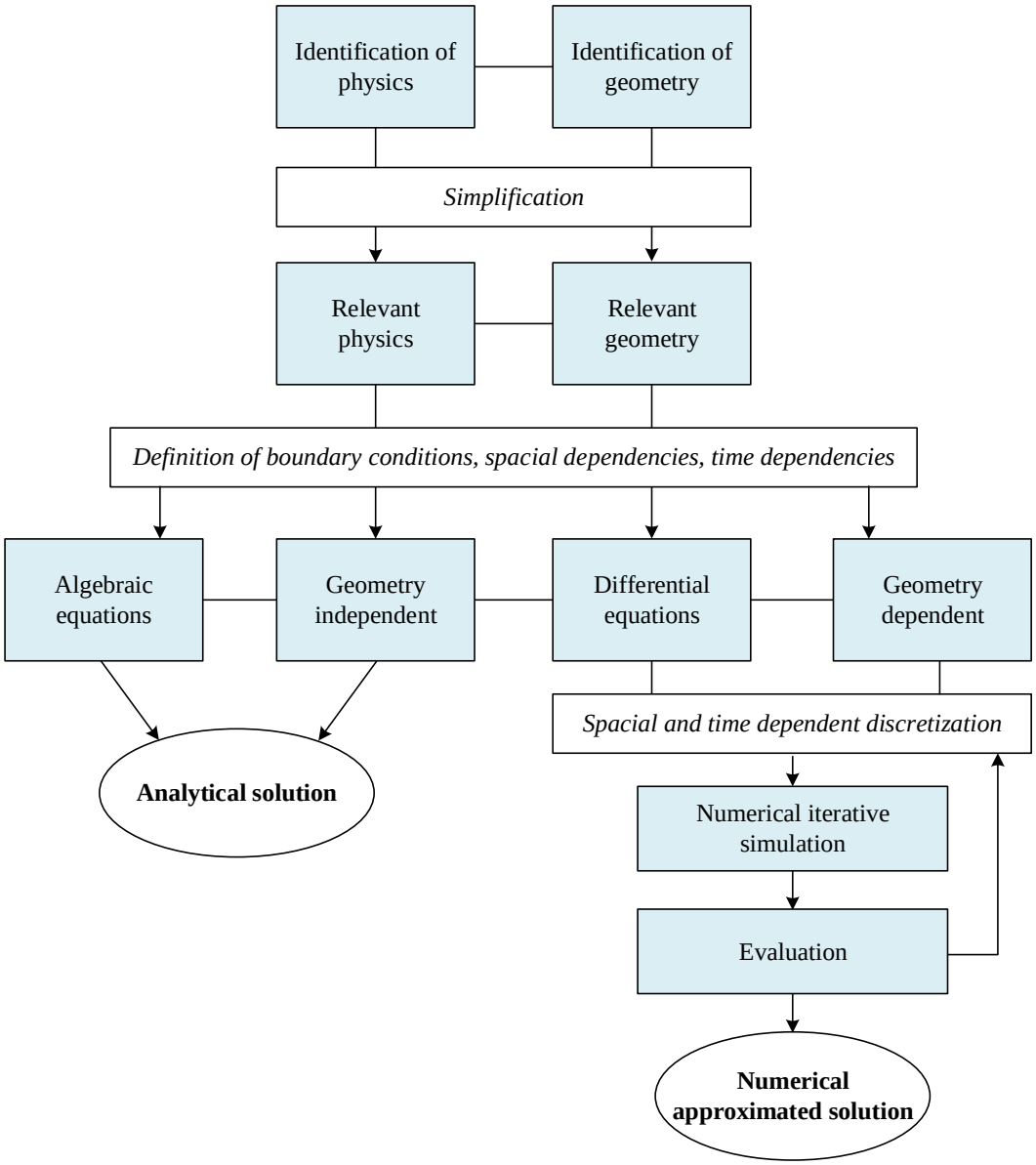

Figure 3.1. Procedure of modelling

that the less dimensions need to be considered the higher the feasibility to solve the mathematical problem, but the lower the quality of the results.

At last it needs to be defined, if the physical problem is stationary or time-dependant. For the latter, appropriate time steps need to be introduced to solve the time-dependant equation. Especially in multi-dimensional spacial systems, this can lead to exponential higher calculation times.

3.1 Analytical and semi-analytical approaches

If enough independent equations can be found, which describe all variables of the physical system sufficiently and they are not differential equations, the system often can be solved analytically. These equation systems are time-independent and do not extend in spacial dimensions (no differential equations with respect to time or space) and thus are subsequently also called *0D*-models. The results of analytical models are always exact and not approximated as in numerical calculations. It also means, that the equations are valid for the whole domain Ω and its boundaries.

If non-linear transcendental functions are involved, like for instance

$$f(x) = e^x - ax - b \ ,$$

the system can be solved semi-analytically with very simple iterative algorithms, in this case for example with the LAMBERT W function (Corless et al., 1996) or other numerical approaches like the NEWTON's method (Munz and Westermann, 2012), which can always be solved correctly with simple calculator- or spreadsheet programs (e.g. *Goal Seek* function; see sec. 5.1). If possible, to find pure analytical or semi-analytical ways of modelling is always preferred over solving differential equations with pure numerical approaches, as long the estimated equations picture the physical problem accurately enough. It is also possible to combine analytical equations with more complex numerical results.

3.2 Numerical simulation with the finite element method

Solving non-linear differential equation systems is not feasible for most cases without the help of a computational algorithm. Hereby, numerical approaches are capable to provide approximated solutions (Munz and Westermann, 2012). Most of natural occurring phenomena need to be described with partial differential equations (PDE), stating gradients in different spacial dimensions or in time, for example the two FICK's laws

(see sec. 2) in a 3D-space:

$$1) \qquad J = -D\,\nabla c = -D\,\frac{\partial c}{\partial x} + \frac{\partial c}{\partial y} + \frac{\partial c}{\partial z} \tag{3.1}$$

$$2) \qquad \nabla J = \frac{\partial J}{\partial x} + \frac{\partial J}{\partial y} + \frac{\partial J}{\partial z} = -\frac{\partial c}{\partial t}\ . \tag{3.2}$$

Especially if the results shall give statements to the distribution of the concentration in space and if Ω has different boundary conditions, for example if a different output concentration is expected than for the input, these equations can be solved with the finite-element-method (FEM).

3.2.1 Pre-processing

In FEM, the domain is divided into finitely large and many elements with a defined length Δx (in the 1D case), which is also called the discretisation of the space (or later in the FEM application software also *meshing*). The PDE system is thus discretized into a discontinuous and approximated linear or non-linear equation system for each knot between the elements, which can be integrated and solved iteratively for each edge of element (Laurien and Oertel, 2018). These steps of discretizing belong to the *pre-processing* of a simulation (Westermann, 2010). An example is given by discretizing eq. 3.1 in the 1D case at place x_i to

$$J_{x_i} = -D\frac{\mathrm{d}c}{\mathrm{d}x}\Big|_i = -D\ \lim_{\Delta x \to 0} \frac{c_{\mathrm{i}+1} - c_{\mathrm{i}}}{\Delta x}\ , \tag{3.3}$$

when D is homogenous in all Ω. This equation shows that the result is more accurate the smaller Δx becomes, which on the other hand results in a higher amount of elements (also called cells). This causes that more equations need to be solved and the calculation time is increased. Hence, as for analytical approaches (sec. 3.1), also for FEM models the optimum balance between accuracy and thus quality of the result and the calculation time needs to be found.

To be able to solve the problem this way, boundary conditions (BC) need to be set. This can be known constant values (e.g. a concentration, velocity or temperature), which is called a Dirichlet BC or known derivatives of conditions (e.g. a change in concentration / velocity or a heat flux) which is called a Neumann BC (Westermann, 2010). A combination of both boundary conditions is a Robin BC.

Fig. 3.2 shows the discretization schematically, by using the forward difference method.

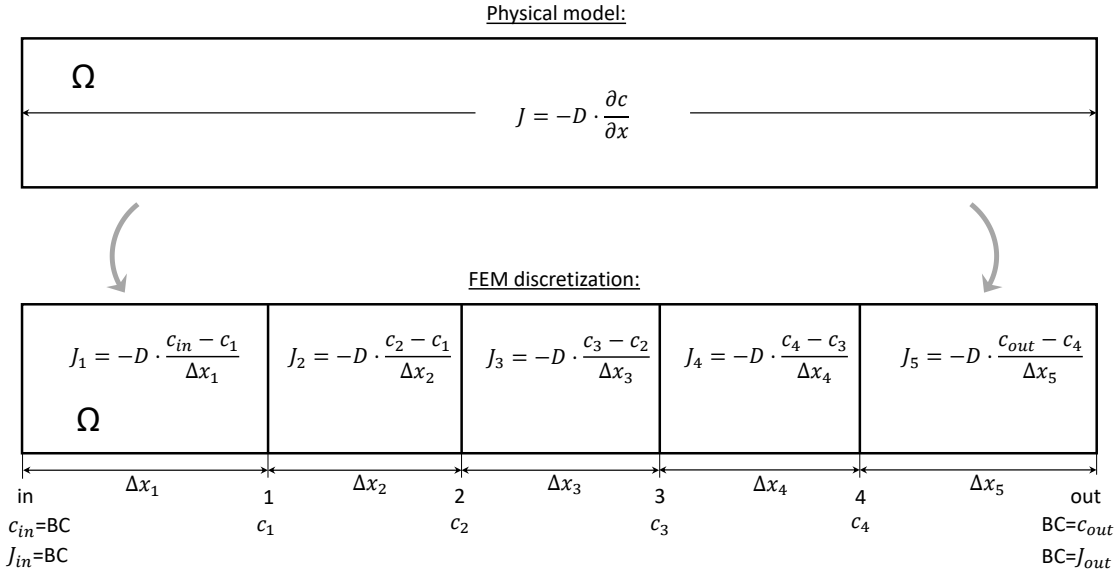

Figure 3.2. Schematic of discretization of the physical model to an FEM model

Eq. 3.3 can be approximated for every Δx with the forward difference to c_i'. The forward, backward and the central difference approximation is respectively

$$c_i' \approx -D \frac{c_{\mathrm{i}+1} - c_{\mathrm{i}}}{\Delta x}\ , \quad c_i' \approx -D \frac{c_{\mathrm{i}} - c_{\mathrm{i}\text{-}1}}{\Delta x} \text{ and } \quad c_i' \approx -D \frac{c_{\mathrm{i}+1} - c_{\mathrm{i}\text{-}1}}{2 \cdot \Delta x}\ . \tag{3.4}$$

All three approaches have different degrees of accuracy, which differ depending on the application. For example, if an ion transport at the place i is expected in positive x-direction, the forward difference method is more likely to succeed. Most simulation programs (sec. 5.1) have inbuilt algorithms which determine automatically which method is used, to find most accurate results (COMSOL AB, 2017c).

The choice of the size and shape of each element highly depends on the physics involved and is made after the geometry of the domain has been determined. Hereby, the geometrical construction is transferred to a mesh of grid points suitable for calculation with the FEM method.

In case of building a model for MCDI, it has to be investigated, which spacial dimensions are needed to fully picture the physical phenomena. For instance the flow-through CDI electrode (fig. 2.2, d) can be regarded as a 1D problem, as convectional transport is occurring in the same direction as diffusion and electromigration events. A model

for an MCDI module operated by the flow by principle (fig. 2.2, a), needs to consider a 2D geometry. Hereby, a further simplification step which needs to be evaluated, is the potential symmetry in geometry and ion transport. Thus, to consider half the cell, meaning one electrode, can be sufficient if solely 1:1 salts as NaCl are dissolved in the water.

As a shape for the cells in a discretised domain (mesh), mostly triangles or rectangles are used (Laurien and Oertel, 2018). As an example for spacial discretising, two different meshes of an FEM model of an MCDI module are pictured in fig. 3.3. Here

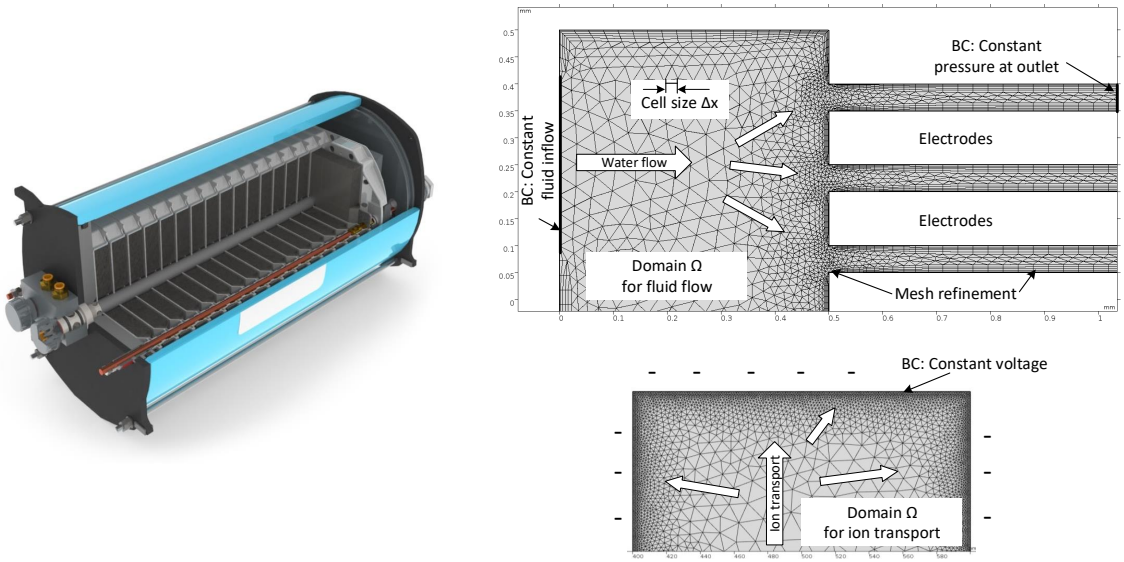

Figure 3.3. Example of spacial discretisation. Left: Cut of a commercial MCDI cell, License: ®Voltea B.V.; right: simplified geometries and meshes for fluid flow and adsorption in pores with set boundary conditions (BC).

it can be noticed that at the edges of the geometry, the sizes of the cells have to be refined, because quicker flows and stronger changes in direction are expected. The cell size is important to picture the geometry of the domain correctly (which needs to be considered especially at round shapes), but also to resolve the physics, in this case the fluid flow, accurately. Next to a wall (no flow, infinite friction), the fluid flow character changes more quickly with higher REYNOLDS numbers Re (sec. 3.3.2), thus with higher volume flows and smaller cross sections. For this reason, the mesh needs to be refined at this boundary layer as well. Schlichting and Gersten (2006, p. 520) introduces the indicator y^+, as a characteristic dimensionless wall coordinate, to determine the size of

the first cell next to a wall, by defining

$$y^+ = \frac{y}{\delta_\mathrm{v}} \text{ ,with } \quad \delta_\mathrm{v} = \frac{h_\infty}{\mathrm{Re}} \ . \tag{3.5}$$

Hereby is δ_v the wall layer, where no fluid movement is occurring, y the size of the first boundary layer and h_∞ the size of the cell in the bulk flow. For the indicator y^+, optimum values are presented by FEM software programs and automatically suggested when meshing a domain (e.g. COMSOL AB, 2017a).
To evaluate the space discretization, a mesh analysis has to be executed. Hereby, the grid is refined after calculation and the new results are compared. If the difference is in an acceptable range, the mesh is fine enough. Thus calculation times are optimized while the solution has a high quality.
Simulation programs are often capable of evaluating the mesh by analysing automatically

- number of cells
- cell grow rate at refined regions
- skewness (internal angles of the cells)

thus the quality of the mesh and subsequently algorithms can enhance the mesh structure by adjusting cell sizes and shapes that also the grow rates and skewness factors are within the operation range of used solver.

A further *pre-processing* step is to discretise the time, if this dimension needs to be considered. In the case of FICK's second law (eq. 3.2), this results in

$$\nabla J_{t_i} = -\frac{\mathrm{d}c}{\mathrm{d}t}\bigg|_i = -\frac{c_{i+1} - c_i}{\Delta t} \tag{3.6}$$

It needs to be mentioned that ∇J_{t_i} is also a function of c due to eq. 3.1, which also depends on time. As in space partition, also for time discretization there exist different methods (e.g. Laurien and Oertel, 2018) to find a solution to eq. 3.6. For instance the forward EULER (eq. 3.7) and backward EULER method (eq. 3.8) described as follows:

$$\nabla J_i = -\frac{c_{i+1} - c_i}{\Delta t} \tag{3.7}$$

$$\nabla J_{i+1} = -\frac{c_{i+1} - c_i}{\Delta t} \ . \tag{3.8}$$

Both cases are subsequently solved with the forward difference method. Hereby the approximation error grows with increasing Δt. Expected error calculations after TAYLOR series expansion, can be found in e.g. Laurien and Oertel (2018, pp. 81).
Furthermore, the time step Δt is depending on the cell size Δx and has to be chosen small enough that the concentration can be resolved correctly by every element and its finite size. As an example the convection of ions is subsequently considered. If the velocity of the fluid flow v forces a convection to the ions, they are transported approximated with similar speed parallel to it. Thus, the time step needs to relate to

$$\Delta t = \frac{\Delta x}{v} \ , \tag{3.9}$$

so that no interpolation between the steps is necessary, which can cause approximation errors. The smaller the cell, the smaller the time step and the higher the calculation times.

3.2.2 Processing the simulation

After the physical equations and their boundary conditions as well as the geometry and mesh of the domains are set, the solving methods can be defined and the simulation processed. The equations can be solved segregated or coupled, which is determined by their dependencies to each other. For example a water flow in MCDI can be solved stationary and segregated and the result of the velocity field can be used as an input for the convection term of the ion transport equation (eq. 3.10). Subsequently, the ion movement can be calculated, which is highly depending on the electric field inside an electrode cell (sec. 2.1) and vice versa (if no electro neutrality is given), thus the ion transport equation has to be solved coupled with the equation for the electric field equation (eq. 3.11), time dependently.

For the solver settings in FEM programs, different properties can be adjusted. For the NEWTON method, damping factors can be set, if solutions cannot be found. Furthermore, the maximum iteration number and -error can be determined, with which the ending point of the solver can be defined.

When stationary calculations are running in an FEM program, the quality of the steps made in the pre-processing can be observed by convergence diagrams. They present the error between the iteration steps over the iteration number. If the maximum number of iterations is reached or the tolerance for error, the solver stops calculating.

For time-dependent simulation, automated algorithms can be used to adapt the time steps if no solution can be found. Then, the reciprocal values of the chosen time step for each iteration can give information about convergence of the calculation. Hereby, the solver can be adjusted to skip to the next time step, if this value goes below a set tolerance.

3.2.3 Post-processing

After the calculation of the model, the post-processing follows. In a 2D model, the solution of every cell can be pictured in surface plots, cross sections as line plots or certain values in the domain as well as boundaries can be forwarded to different models. To compare the results with existing experimental data is crucial, to evaluate the quality of the solution. Due to the numerical approximations, they can be far away from reality. Consequently, the models have to be rethought or the discretizing steps refined. The choice of different solvers or the adjustment of their working parameters like iteration step damping or error tolerance can improve the results as well.

3.3 Theoretical background for (M)CDI modelling

Firstly all physical phenomena inside an MCDI cell need to be addressed and their relevance evaluated. Figure 3.4 gives an overview of the main physics occurring inside an MCDI cell. Like highlighted in sec. 2.4, different scales in the MCDI process are responsible for different effects influencing the desalination performance.
In a large scale perspective, the water flow through the module is predominant. It plays the role of feeding the cells with dissolved salts, simplified explained with the physics of convection and can be relevant for a model, which needs to consider different module sizes and geometries.
The water flow through the MCDI module can be described with classical fluid dynamics and numerically with the Navier-Stokes-Equations (sec. 3.3.2). Hereby, geometrical influences on the supply of the electrodes with water and hence amount of ions can be determined also time dependently.

The EDL plays a significant role in modelling adsorption processes in an MCDI cell and thus needs to be examined on a closer look. One way to describe the adsorption of ions is to picture an appropriate model of the EDL as their storage volume. This layer

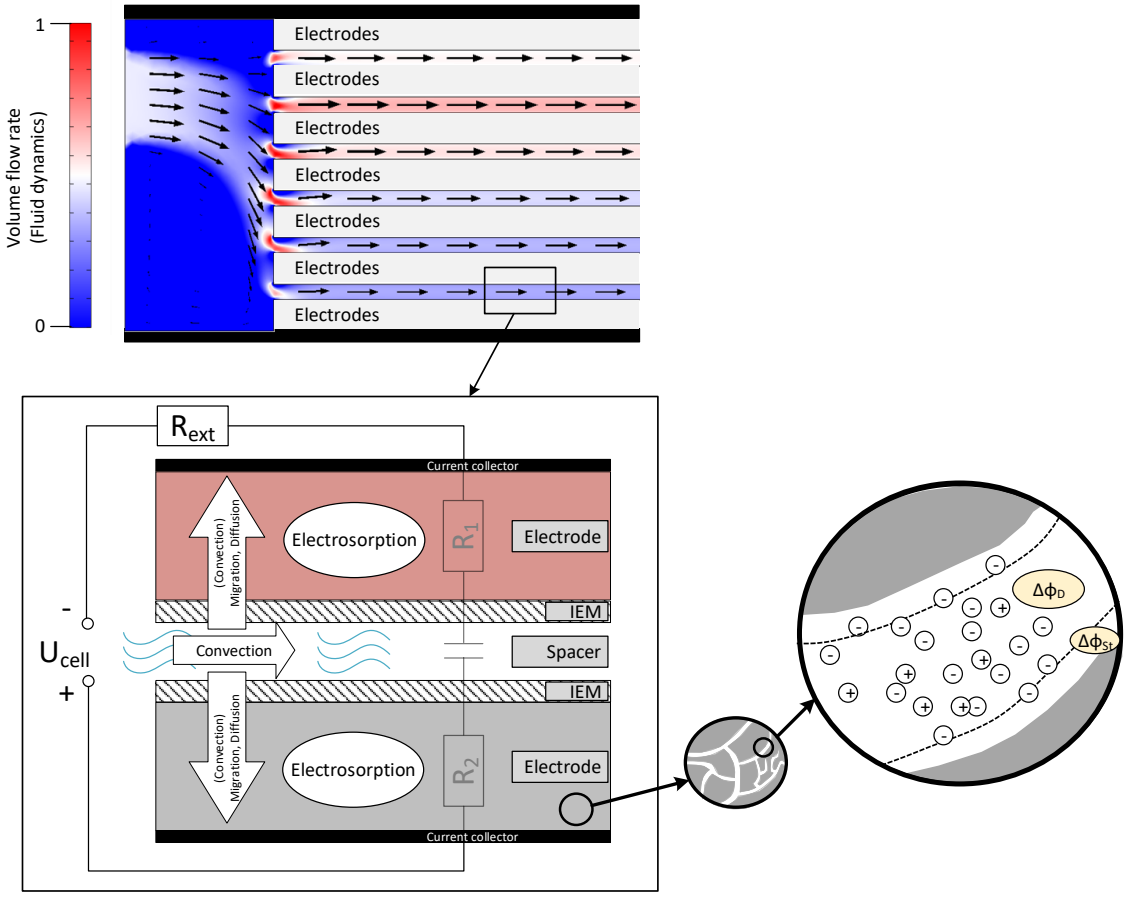

Figure 3.4. Overview of the physics in an MCDI cell

can be described by the simplified Gouy-Chapman-Stern (GCS) model (fig. 2.1) and in a mathematical expression for example with the Poisson-Boltzmann equations (eq. 2.2 and eq. 2.3). It combines the electric potential and charge density relation with the theory of Boltzmann statistics for the spacial distribution of ions (Butt et al., 2006). Another way to describe the ion movement and their distribution is the combination of the Poisson equation with the Nernst-Planck equation (sec. 3.3.1), which describes their diffusion, migration and convection part.

After applying electrical voltage to the cell, the movement of salt ions towards and inside the electrodes is mainly affected by (electro)migration and diffusion. The active carbon electrodes have pores, which can be divided in macro-, meso- and micropores. Biesheuvel et al. (2014) found that salt ions are mainly adsorbed in the micropores through the EDL at the boundary to the active carbon. The macro- and mesopores transport the ions through diffusion and migration.

In the following subsections, the transfer of fundamental physics, the ion and water transport inside an MCDI cell, to applicable mathematical models is made. Furthermore the solution diffusion model for calculating desalination problems with NF and RO membranes is specified.

3.3.1 Ion transport model

Ion transport in an electrochemical system is given by the physics of convection, diffusion and migration (sec. 2.1). Partly derived from Fick's laws (eq. 2.12), the ion movement in an MCDI module can be described with the NERNST-PLANCK equation (Maex, 2014). It combines diffusion, migration and convection influences (sec. 2.1) on the ion movement like described in eq. 3.10.

$$J_i = -D_i \nabla c_i - D_i c_i \frac{z_i F}{RT} \cdot \nabla \phi + c_i \vec{v} \quad \text{and} \quad \nabla J_i = -\frac{\partial c_i}{\partial t} \ , \tag{3.10}$$

where J is the flux of the ion i, D the diffusion coefficient c the concentration of the ion, z the valency of the ion, F the Faraday constant, R the universal gas constant, T the temperature, ϕ the electrical potential, $\vec{v}$ the velocity vector of the surrounding fluid and t the time.

The distribution of the electrical field between two electrodes in dependency of the charge density caused by the ion's concentration is described by the POISSON equation (Butt et al., 2006), stated as follows:

$$\nabla^2 \phi = -\frac{\sigma}{\epsilon_0 \epsilon_r} \ , \tag{3.11}$$

with σ being the charge density and $\epsilon = \epsilon_0 \epsilon_r$ the permittivity of the dielectricum.
If these two equations, subsequently called NERNST-PLANCK-POISSON (NPP) equations, are coupled, via ϕ and

$$\sigma = F \ \Sigma_i (z_i \cdot c_i) \ , \tag{3.12}$$

they form a partial differential equation (PDE) system, which can be solved for instance with the finite-element-method. Like that, the spacial distribution of ions caused by electrodiffusion can be determined.
These NPP equations are successfully used in many models (see sec. 4). They are the basic of ion transport inside the MCDI model and thus considered in this thesis.

3.3.2 Computational fluid dynamics

Water flows that occur in reality can usually only be calculated analytically with great effort or not at all. The same applies to the flow through the MCDI cell discussed in this thesis. Many assumptions have to be made in the analysis, which simplify the flow pattern and thus make it calculable. In order to achieve a sufficiently accurate solution, numerical approaches must be chosen for complex flows. A frequently used approach is that of NAVIER and STOKES. The so-called NAVIER-STOKES equations are thus subsequently discussed in more detail.

Firstly, an infinitesimally small volume through which a fluid flows is considered. The laws of conservation of mass, momentum and energy are applied to it. This means that no mass, momentum forces and energy are lost when flowing through the considered volume. This further means that in all three spacial directions the incoming mass flows, momentum and energies are equal to the outgoing ones. Laurien and Oertel (2018) describes the mass conservation over the volume with

$$\frac{\partial \rho}{\partial t} + \frac{\partial(\rho\, u)}{\partial x} + \frac{\partial(\rho\, v)}{\partial y} + \frac{\partial(\rho\, w)}{\partial z} = 0 \tag{3.13}$$

Here $\partial\rho/\partial t$ is the change in density over time and the other three summands are the changes in mass fluxes (density times velocity fraction) in all three-dimensional directions: x, y and z, with

$$\begin{pmatrix} u \\ v \\ w \end{pmatrix} = \vec{v}\ . \tag{3.14}$$

In the case of incompressible flows (liquid flows), the density remains constant over time and space.

The momentum $\vec{p}$ is defined by

$$\vec{p} = m \cdot \vec{v}\ , \tag{3.15}$$

with m being the mass. Related to the considered volume, its change in time corresponds to:

$$\frac{\partial(\rho \cdot dx \cdot dy \cdot dz \cdot \vec{v})}{\partial t} \tag{3.16}$$

The change of momentum during time corresponds to the difference of the entering and outgoing momentum currents, as well as the sum of the shear and normal stresses τ acting on the surfaces of the volume element and its volume forces such as gravity, with

the gravitational acceleration g, electric forces and magnetic forces. Put together, the momentum equation in the z-direction results in:

$$\frac{\partial(\rho \cdot w)}{\partial t} + \frac{\partial(\rho \cdot w \cdot u - \tau_{xz})}{\partial x} + \frac{\partial(\rho \cdot w \cdot v - \tau_{yz})}{\partial y} + \frac{\partial(\rho \cdot w^2 + p - \tau_{zz})}{\partial z} - \rho \cdot g_z = 0 \quad (3.17)$$

The momentum equations for the x-, and the y-direction are constructed analogously. The exact derivation of these equations can be found for example in Lecheler (2009).

The energy conservation equation corresponds to the first law of thermodynamics with E being the total energy, W the work and Q the heat:

$$\frac{\partial E}{\partial t} = \dot{E}_{\text{in}} - \dot{E}_{\text{out}} + \dot{W}_g + \dot{W}_p + \dot{W}_\tau + \dot{Q}_{\text{in}} - \dot{Q}_{\text{out}} \ . \quad (3.18)$$

Hereby, the difference of the total energies is the difference of the energy supplied and taken away by the mass flow, $\dot{W}_g$ is the work flux of the mass force, $\dot{W}_p$ is the work flux of the pressure force and $\dot{W}_\tau$ is the work flux of the friction force. If this equation is applied to the temporal change in the infinitesimally small volume, after derivation and transformation it yields the energy conservation equation:

$$\begin{aligned}
&\frac{\partial}{\partial t} \cdot [\rho \cdot (e + \frac{1}{2} \cdot \vec{u}^{\,2})] \quad (3.19)\\
&+\frac{\partial}{\partial x} \cdot [\rho \cdot u \cdot (h + \frac{1}{2} \cdot \vec{u}^{\,2}) - (u \cdot \tau_{xx} + v \cdot \tau_{xy} + w \cdot \tau_{xz}) - \lambda \cdot \frac{\partial T}{\partial x}]\\
&+\frac{\partial}{\partial y} \cdot [\rho \cdot v \cdot (h + \frac{1}{2} \cdot \vec{u}^{\,2}) - (u \cdot \tau_{yx} + v \cdot \tau_{yy} + w \cdot \tau_{yz}) - \lambda \cdot \frac{\partial T}{\partial y}]\\
&+\frac{\partial}{\partial z} \cdot [\rho \cdot w \cdot (h + \frac{1}{2} \cdot \vec{u}^{\,2}) - (u \cdot \tau_{zx} + v \cdot \tau_{zy} + w \cdot \tau_{zz}) - \lambda \cdot \frac{\partial T}{\partial z}]\\
&\qquad -\rho \cdot (u \cdot g_x + v \cdot g_y + w \cdot g_z) - \rho \cdot \dot{q}_S \ = \ 0 \ ,
\end{aligned}$$

with e and q being the specific energies related to mass and λ the heat coefficient of the material. The exact derivation of the equation can be found in Lecheler (2009) or Laurien and Oertel (2018).

These three conservation equations together form the NAVIER-STOKES equations, which are used to solve complex flow problems numerically. Together they form a non-linear system of equations which can only be solved iteratively. This means that the equations are first solved with a starting value and then recalculated with the solution value.

If the considered flow case is turbulent (see sec. 2.2), further turbulence equations are added. These equations are model approaches that calculate a so-called turbulence viscosity factor (Ferzinger and Perić, 2008). It simulates the energy dissipation caused by the turbulence at certain points. There are models that calculate this factor with zero, one or two additional equations. An example for the latter is the k-ϵ model. It consists of the equation for the kinetic energy of the turbulence k and the equation for the turbulence dissipation ϵ.

The resulting system of equations is finally solved in a finite number of points in the flow domain as a function of their spacial coordinates (FEM).

4 Literature review and state of the art of (M)CDI modelling

This chapter gives an overview of the state-of-the-art of (M)CDI modelling, based on a literature research and subsequently narrows down the models, which can be used in this thesisin sec. 4.10.
For the emerging technology, many different models have been developed and no predominant approach, which is widely used and evaluated for small or industrial scale desalination plants, is existing. The models mainly describe processes inside single parts of the module, with the goal to enhance efficiencies of those. For instance to increase salt adsorption rates for electrodes or decrease electrical resistance of ion-exchange-membranes and other parts in the module. No model, with the purpose of predicting desalination characteristics and performance while different operational parameters are used, which is valid for different module sizes as well as no tool which makes a handy use of it possible, has been developed.

For this reason, different modelling strategies for membrane capacitive deionization are compared and the most promising, which are taken into account for the use in this thesis project are highlighted.

4.1 Energy and RC-models

4.1.1 Theory

Electrically, an MCDI-cell can be considered as a serial and parallel connection of resistor-capacitor (RC) units. To simulate the electrical behaviour and calculate the energy consumption of an MCDI-unit, an RC model can be used. Hereby, the RC links can determine usable, non-usable and possibly recoverable electrical energy in the system. Andres et al. (2017) make an approach by modelling a CDI cell with unipolar

and bipolar RC connections. They found that three parallel connections of RC links are sufficient to describe the EDL in one pair of electrodes of a CDI (see fig. 4.1) and can substitute complex connections of impedance and capacitors (ZC). An additional

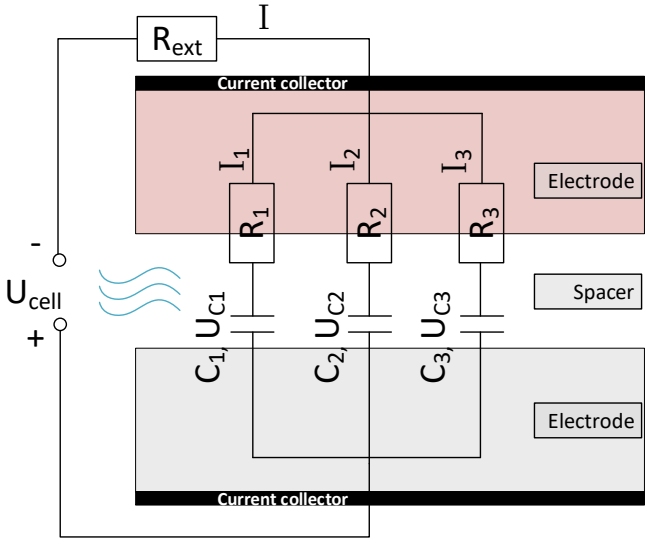

Figure 4.1. RC model of a CDI cell according to Andres et al. (2017)

external resistance is linked to model leakage currents and losses in the periphery. These packs of three can be linked in series or parallel to represent bipolar or unipolar connections of CDI electrodes. Subsequently, the voltages and electrical currents can be calculated by OHM's laws:

$$U_{\text{elec}} = U_{\text{cell}} - R_{\text{ext}} \cdot I \ , \qquad I = \sum_{e} I_e \ , \qquad R_e \, C_e \, \frac{\mathrm{d}U_{\text{C,e}}}{\mathrm{d}t} + U_{\text{C,e}} + U_{\text{elec}} = 0 \ , \tag{4.1}$$

where R_{ext} represents the external electrical resistance and the subscript e marks the single RC-links of a cell. The subscript 'elec' marks the sum of the three links 'e'.

To study the effect of the pore structure and micropore-macropore ratio on electrode performance, Suss et al. (2013) developed a different RC-model for the micropore distribution inside the electrode. They model the macropore (transportation pore) as impedance links (Z) in series and the micropores as parallel connected C and CZ-links, to model the impedance behaviour of a CDI electrode.

4.1.2 Study results

As an experimental setup, Andres et al. (2017) used single and uni- or bipolar connected multiple CDI pairs of electrodes, filled with an NaCl solution with an electrical conductivity of $\kappa = 5.5\ \mathrm{mS\,cm^{-1}}$. The electrodes were charged with a constant voltage $U = 1.2$ V (6 V for bipolar system). Their model showed agreement of the charge and discharge behaviour of unipolar and bipolar linked CDI cells with experimental data and they found that a bipolar connection has lower resistance and thus is more energy efficient.
Nevertheless, they only showed the electrical behaviour of the CDI cell and cannot give information about the desalination performance and its efficiency, since no transport models were included.

To evaluate their impedance model, Suss et al. (2013) fabricated several hierarchical carbon aerogel monolith (HCAM) electrodes with controlled pore distribution and used electrochemical impedance spectroscopy (EIS) to measure the porous electrode impedance. With their model they plot complex impedance distribution, for an EDL capacitance of the storage- and the transport pores of $C_s = 1$ F and $C_t = 0.01$ F respectively, as well for the transport pore resistance of $R_t = 1\ \Omega$. R_s of the storage pore (micro pore) is varied. The plot shows agreement with the EIS measurements and they found that a very small R_s compared to R_t is important to decrease the overall resistance of an electrode. Furthermore they show that the EIS measurements and their model is valid to quickly characterize porous CDI electrodes concerning their pore size distribution. However, they can give no statement towards desalination efficiency.

4.2 Response surface methodology

4.2.1 Theory

Jeong et al. (2020) used the response surface methodology (RSM) to picture the behaviour of their total pilot plant consisting of a combined system out of NF and MCDI. With this method, experimental data is collected while significant variables of the system are changed (for instance with the Box-Behnken design of Box and Behnken (1960)) and the response of the system is measured (Bezerra et al., 2008). The experimental data was used to fit the linear, interaction and quadratic coefficients, β_i, β_{ij} and

β_{ii} respectively, of the following equation

$$\hat{y} = \beta_0 + \sum_{i=1}^{k} \beta_i \, x_i + \sum_{i=1}^{k} \beta_{ii} \, x_i^2 + \sum_{1 \leq i \leq j}^{k} \beta_{ij} \, x_i \, x_j + \epsilon \; . \tag{4.2}$$

Hereby, $\hat{y}$ are the predicted variables, in the case of Jeong et al. (2020) the specific energy consumption (SEC) and effluent salt concentration of the hybrid system, β_0 a constant term and ϵ the residuals to experimental data. The received regression curve is analysed for its residuals and root mean square errors and stated valid for the desalination system.

4.2.2 Study results

The experimental setup of Jeong et al. (2020) uses NF membranes combined with a commercial available MCDI module (E-100, Siontech Co., Korea) with 200 pairs of electrodes (*sic*) and a CC with $I = 2$ A of charge and discharge currents for each 300 s duration is applied, due to the stable effluent salt concentrations (sec. 2.4), which is forced by CC operation and needed for the RSM. Model water with six different compositions was treated: NaCl + $MgSO_4$ -solutions with c_i = 0-10 mM and $c_{\mathrm{tot}} = 10$ mM as well as a 35 g L^{-1} sea water solution.
The model showed an agreement with experimental data (coefficient of determination $R^2 > 0.93$ and root mean square error $RMSE < 0.09$). With the RSM they examined the effects of feed concentration, recovery rate of the NF system and MCDI water flow on the SEC and effluent salt concentration of the combined system and thus an optimization of the system was possible. With this method, they theoretically compare the application of NF-MCDI-, with conventional RO systems. The disadvantage of this model is that it fits only for the present MCDI system and extensive experimental testing needs to be foregone, to fit the coefficients of the response equation. The advantage is that a very quick solution can be derived, which can be calculated by simple spreadsheet software (e.g. the ones mentioned in sec. 5.1.1).

4.3 Modified Donnan model

Up to date, concerning the amount of published peer-reviewed articles in the area of CDI modelling, research is mainly focused on the adsorption process of ions in the electrodes,

with the goal of improving the adsorption material to increase efficiency of the MCDI process. A very promising approach for ion adsorption is the modified DONNAN (mD) model and thus presented subsequently.

4.3.1 Theory

Basser and Grodzinsky (1993) showed that the statistical, mechanical model of the EDL, described by the POISSON-BOLTZMANN equations (eq. 2.2 and eq. 2.3) and their developed thermodynamic DONNAN model, describe same phenomena. Furthermore, the electrolyte charge densities at an electrode interface can be calculated with both approaches, for low ionic strengths. They describe the ideal DONNAN potential by an electrostatical potential difference like the chemical potential with

$$\Delta\phi_{\mathrm{D}} = -\frac{RT}{F}\ln\left(\frac{c_0}{c_i}\right) \ , \tag{4.3}$$

where c_0 and c_i are the two different ion concentrations in the different phases.
A very promising further development of this model, for the application on CDI cells, is the modified DONNAN model, which is used successfully in many studies (see sec. 4.3.2).

It follows a simplification of describing the EDL inside micropores, where the main part of ion adsorption takes place (Porada et al., 2012). Due to the width of micropores are defined as $b < 2$ nm (e.g. Porada et al., 2013) and thus smaller than the usual Debye-length of the EDLs, they are practically overlapping and hence can be approximated to a constant Donnan-potential $\Delta\phi_{\mathrm{D}}$ (Biesheuvel et al., 2011a, 2014). A schematic is illustrated in fig. 4.2. This simplification makes it possible to compute the equations used for a model quicker, since they can now be solved semi-analytically (one analytical part and a transcendental equation, which can be solved iteratively e.g. with GAUSSIAN elimination). The DONNAN-potential $\Delta\phi_{\mathrm{D}}$, develops out of the difference between the ion concentration outside and inside the micropore (Kastening and Heins, 2005). The DONNAN model is modified by two parameters to fit for desalination with MCDI and subsequently called modified DONNAN (mD) model. To consider the finite size of an ion and thus the charge inside the electrode and the ion cannot get infinite close, a Stern layer capacity C_{St} is introduced in this model. Furthermore, a factor for additional attractive forces from adsorption effects, which are not caused by the electric field, in shape of a chemical potential μ_{att} is added to the model.
With this model the BOLTZMANN statistics (eq. 2.3 or eq. 4.4) can be combined with

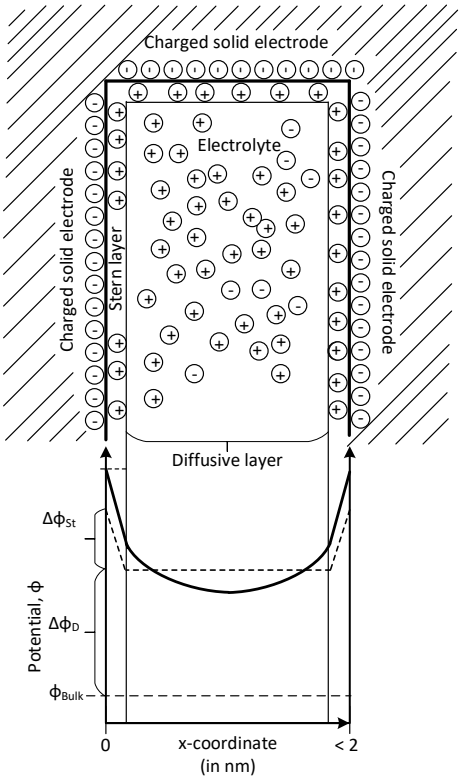

Figure 4.2. Schematic of overlapping EDLs inside an MCDI micropore

the voltage applied to the MCDI cell (eq. 4.8), via the relation of charge density and Stern potential (eq. 4.6). After inserting eq 2.5, which defines the work needed to move an ion towards the electrode into the BOLTZMANN equation eq. 2.3, the concentration of the salt ions in the micropores $c_{\mathrm{mi,i}}$ is given as follows:

$$c_{\mathrm{mi,i}} = c_{\infty,\mathrm{i}} \ \exp(-z_{\mathrm{i}} \cdot \Delta\phi_{\mathrm{D}} + \mu_{\mathrm{att,i}}) \ , \tag{4.4}$$

where $c_{\infty,i}$ is the ion concentration outside of the pore, z its valency and the spacial constant $\Delta\phi_{\mathrm{D}}$ is the dimensionless DONNAN potential, divided by the thermal voltage

$$U_{\mathrm{T}} = \frac{RT}{F} \ . \tag{4.5}$$

Furthermore, the excess chemical potential $\mu_{\mathrm{att},i}$ has been added to the electrochemical potential $\mu_{\mathrm{elchem}} = z_i \cdot \Delta\phi_{\mathrm{D}}$.

The additional Stern layer capacity is responsible for a STERN potential $\Delta\phi_{\mathrm{St}}$ directly next to the interface of the electrode. Assuming that the charge density in the micropores σ_{mi} is equal to the negative charge density σ_{el} in the electrodes, the relation

between those and the STERN potential is given in the following eq. 4.6.

$$-\sigma_{\mathrm{el}} = \sigma_{\mathrm{mi}} = \sum_i (z_i \cdot c_{\mathrm{mi,i}}) = -C_{\mathrm{St,vol}} \cdot \Delta\phi_{\mathrm{St}} \cdot \frac{U_T}{F} \ . \tag{4.6}$$

The volumetric STERN layer capacity in (Farad m^{-3}) can only be determined empirically throughout experiments and is depending on material constants of the used active carbon (α and $C_{\mathrm{St},0}$ of eq. 4.7). It is hereby defined as e.g. Biesheuvel et al. (2014)

$$C_{\mathrm{St,vol}} = C_{\mathrm{St},0} + \alpha \cdot \sigma_{\mathrm{mi}}^2 \ , \tag{4.7}$$

where $C_{\mathrm{St},0}$ is the STERN layer capacity in non charged state and α a fitting parameter to define its increase.

The magnitude of the DONNAN potential together with the STERN potential appearing next to the electrode's interface, equals the voltage applied to the electrodes U_{cell}, as shown in eq. 4.8.

$$\frac{U_{\mathrm{cell}}}{U_T} = |\Delta\phi_D + \Delta\phi_{\mathrm{St}}| \ . \tag{4.8}$$

Leading back to mechanical adsorption forces, the factor $\mu_{\mathrm{att},i}$ can be determined with different approaches, for instance, by its empirical adjustment to fit experimental data or with the theory of image forces. For the latter, Biesheuvel et al. (2014) found that μ_{att} cannot be assumed constant, but as a function of c_{mi}. It is explained with the additional occurrence of image forces inside the micropore. The EDLs are overlapping because the λ_{D} is smaller than the pore width b. The DEBYE length is also correlating with the BJERRUM length λ_{B}, which tells similar to λ_{D}, when electrical- is equal to thermal energy (see sec. 2.1). Meaning, when electrical charges are closer to each other than λ_{B}, COULOMB interactions are strong and additional attractive forces need to be considered. The BJERRUM length is defined as

$$\lambda_{\mathrm{B}} = \frac{e_0^2}{4\,\pi\epsilon_{\mathrm{r,mi}}\,k_{\mathrm{B}}\,T} \ , \tag{4.9}$$

where $\epsilon_{\mathrm{r,mi}}$ is the relative permittivity inside the micropore. λ_{B} is within the width b of a micropore and thus ions inside have additional image force attractions to the electrode (Biesheuvel et al., 2014). This attracting energy (COULOMB energy) is considered as constant for an ion in the middle of a micropore. Nevertheless, the more ions are present the more this image force is shared by many and the electric field in the micropore is decaying more quickly. Thus, depending on the pore volume (characteristically $V_{\mathrm{mi}} = b^3$)

and the pore concentration c_{mi}, this attractive force is decreasing and μ_{att} is given as

$$\mu_{\mathrm{att}} = \frac{E_{\mathrm{att}}}{c_{\mathrm{mi}}} \tag{4.10}$$

$$\text{with} \quad E_{\mathrm{att}} = z^2 \, k_{\mathrm{B}} \, T \, \lambda_{\mathrm{B}} \, b^{-4} \, . \tag{4.11}$$

After implementing a c_{mi} dependent instead of a constant μ_{att}, the model is called improved mD (imD) model.

4.3.2 Study results

Biesheuvel et al. (2014) describes the modified DONNAN model for the porous electrodes, where simplification steps are used to avoid extensive computational resources and to find analytical solutions. It is used in many studies as e.g. in Biesheuvel et al. (2011a, 2014); Dykstra et al. (2016); Hassanvand et al. (2017); Wang et al. (2018a); Porada et al. (2020).
Zhao et al. (2010); Biesheuvel et al. (2011a, 2014) use the same experimental data and materials that are inter alia commercial carbon electrodes from *Voltea B.V.* (The Netherlands), which hold the characteristics showed in tab. 4.1, where p is the porosity. The

Table 4.1. Characteristics based on a commercial porous carbon electrode from *Voltea B.V.*

p_{mi}	ρ_{elec}	$C_{\mathrm{St,0}}$	α	E
0.3	0.55	0.145 GF m^{-3}	30 F m^3 mol^{-2}	300 kT mol m^{-3}

feed water is an NaCl solution within c = 5-20 mM and during charge phase constant U = 0.2-1.4 V were applied.
Firstly, Zhao et al. (2010) show that the experimental data of salt adsorption equilibrium can be reproduced with the GCS model (fig. 2.1) and the PB equations (eq. 2.2 and 2.3). Subsequently, Biesheuvel et al. (2011a) prove that the mD-model can reproduce the same results with much less effort after C_{St0}, α and μ_{att} (eq. 4.10) were determined empirically. Biesheuvel et al. (2014) further state that the results of the effluent salt concentration after CV charging and 0V discharging, can be reproduced even more exactly with the imD model, by making the additional attractive potential dependent on the micropore ion concentration (eq. 4.10). In the latter approach, $V_{\mathrm{mi}} \approx b^3$ (for eq. 4.11) needs to be defined through experimental data. This improvement is especially visible

for the experiment with the smaller influent salt concentrations $c_{\mathrm{in}} = 5$ mM than for $c_{\mathrm{in}} = 20$ mM, where they point out that the influent salt concentration ($c_{\mathrm{in}} = c_{\infty}$) has a lower impact on the charge efficiency Λ than expected after analysing the mD-model in Biesheuvel et al. (2011a). The better fitting of the imD model is further true for high concentrations $c_{\mathrm{in}} > 60$ mM, comparing the dependencies of the total salt adsorption Γ_{salt} and electrical charge Σ and thus of Λ (eq. 2.24) from c_{in}.

This additional attractive term is stated to be responsible for ion adsorption, also in uncharged active carbon. To investigate the validity of the imD approach for $\mu_{\mathrm{att}}(c_{\mathrm{mi}})$ in this case, further experiments to determine salt adsorption over the external salt concentration c_{∞} were made in Biesheuvel et al. (2014). Hereby, the study showed no agreement for the mD- and only limited for the imD model (for $c_{\infty} < 25$ mM).

An overview of the validity of different modified DONNAN models is given by tab. 4.2 in the following section.

4.4 Amphoteric Donnan model

4.4.1 Theory

Another approach to determine the additional attractive forces from the modified Donnan model (section 4.3) and eventually further extend the applicable range of the imD model, is to see the activated carbon electrode as an amphoteric ion adsorbent, which can possess acid and basic properties (Dykstra et al., 2017; Biesheuvel, 2015; Duval et al., 2001). The activated carbon electrodes receive them from charged layers at the solid-liquid interface, which thereby have attracting or rejecting effects on the ions in the micropores. As for the acid layer, carboxyl acid groups formed on the carbon (see tab. 2.1) are most responsible (Montes-Morán et al., 2004) and are negatively charged. The addition of a basic layer can occurre through positively charged hydrogen ions, which develop through water electrolysis (tab. 2.1). One electrode in MCDI can possess both layers. This is how the amphoteric model explains the excess chemical potential μ_{att}, an additional attractive force, from the modified Donnan model and is substituting it with a fixed chemical charge σ_{chem}, existing in the micropore and being caused by the amphoteric effects (Biesheuvel, 2015).

This approach implies that the relation from eq. 4.6 changes to

$$-\sigma_{\mathrm{el,j}} - \sigma_{\mathrm{chem,j}} = \sigma_{\mathrm{mi,j}} \ , \tag{4.12}$$

where j stands for the region, where either acidic or basic layers are coating the electrode. Subsequently, the ratio of regions where positive charged layer are present and vice versa has to be defined and adjusted to fit experimental data, since this distribution cannot be predicted (Montes-Morán et al., 2004; Boehm, 1994). The division in positive and negative charged surface regions means further that

$$c_{\mathrm{i,mi}} = \sum_{j} \gamma_{\mathrm{j}}\, c_{\mathrm{i,j}} \ , \tag{4.13}$$

where γ is the volumetric amount of region j in the micropore volume. If acidic and basic spaces are equally distributed this means $\gamma_{\mathrm{j}} = 0.5$.

4.4.2 Study results

Using this approach and the same experimental data from sec. 4.3.2, Biesheuvel (2015) show an agreement of the amD model during 0V adsorption for the total range of bulk salt concentrations 5 mM $< c_\infty <$ 250 mM and thus better validity than the imD model as well as same agreement for the same range for charge efficiency. The latter they proved further for the same concentrations of a $CaCl_2$ solution instead of NaCl.
Applying the amD model, the fixed chemical charge σ_{chem} need to be empirically defined instead of the μ_{att} from the mD model.

The validity of the mD models can thus be summarized as follows in tab. 4.2.

Table 4.2. Validity (ranges of NaCl bulk concentrations) of mD models concerning charge efficiency Λ and 0V adsorption (0VC)

Ref. to	**mD model**	**imD model**	**amD model**
Λ	10 mM $< c_\infty <$ 40 mM	5 mM $< c_\infty <$ 250 mM	5 mM $< c_\infty <$ 250 mM
0VC	-	5 mM $< c_\infty <$ 25 mM	5 mM $< c_\infty <$ 250 mM

4.5 Models for faradaic reactions

To model the faradaic reactions inside a CDI cell, can be further helpful to determine additional ion attractive terms like in the mD models (sec. 4.3-4.4) and efficiency degrees of the desalination process more accurately, since they can increase or decrease the (M)CDI performance (sec. 2.1, Faradaic Reactions). Furthermore, they can be helpful to predict pH changes inside an electrochemical cell.
Dykstra et al. (2017) hereby uses the Frumkin-Butler-Volmer (FBV) equation (as in Biesheuvel et al. (2011b)), which takes into account an additional faradaic current J_F based on the oxidation and reduction reactions in the acidic and basic regions of the electrode (sec. 2.1) defined by

$$J_\mathrm{F} = k_\mathrm{R}\, c_\mathrm{O}\, \exp\left(-\frac{1}{2}\,\Delta\phi_\mathrm{St}\right) - k_\mathrm{O}\, c_\mathrm{R}\, \exp\left(+\frac{1}{2}\,\Delta\phi_\mathrm{St}\right)\ . \tag{4.14}$$

Hereby is k_R and k_O the kinetic rate for reduction and oxidation reaction respectively and c_O and c_R the concentration of a oxidized and reduced species respectively. With the fluxes induced by convection, diffusion and migration as well as the additional one through faradaic reactions they estimate through equilibrium calculations the pH change between influent and effluent.

By changing the applied voltages at the MCDI cell, Dykstra et al. (2017) found that including the faradaic reactions, the pH change is much higher in both, the model and experimental data.
The change of pH is not directly affecting the desalination performance and thus no focus is put in this thesis.

4.6 Model for ion exchange membranes

4.6.1 Theory

Biesheuvel et al. (2011a) and Dykstra et al. (2017) show inter alia a model for the ion exchange membrane, where a membrane capacity X is introduced, which results from its fixed charges. With this, the difference of Donnan potential $\Delta\phi_\mathrm{D,M}$ between both

sides of the membrane can be determined, which adds up to the total $\Delta\phi_{\text{cell}}$ of the pair of electrodes:

$$\Delta\phi_{\text{D,M}} = \operatorname{arcsinh}\left(\frac{\omega X}{2\, c_{\text{s}}}\right) , \tag{4.15}$$

where ω is the sign of the IEM (positively or negatively charged).
Furthermore, they use an adapted diffusion coefficient inside the IEM of 10% of D_i in water, to adjust the ion transport into the electrodes. For the latter, the NERNST-PLANCK equations (eq. 3.10) without the convection term are used inside the membrane. Flow entrance effects in the membranes, which are seen as thin diffusion layers, are hereby not considered, as it was found in the study of Pawlowski et al. (2014) for reverse electrodialysis applications.

4.6.2 Study results

The model data which is presented in Biesheuvel et al. (2011a) is equilibrium data from constant voltage operation, meaning the cell potential $U_{\text{cell}} = \Delta\phi_D + \Delta\phi_{\text{St}}$ inside the electrode and no potential gradients due to transport are considered. The influent NaCl concentration was $c_{\text{in}} = 20$ mM and the constant charging voltage $U_{\text{ch}} = 1.2$ V. Despite the model for the IEM, they use the NPP equations (sec. 3.3.1) as a transport model and the mD model for ion adsorption.
Biesheuvel et al. (2011a) compare the desalination behaviour (accumulating effluent salt concentration) of CDI and MCDI with zero- and reversed voltage discharge (see sec. 2.4). For the latter, the model data does not fit quantitatively for the characteristics of the discharge phase. They evaluated the model for total cumulative salt adsorption during CV operation depending on the influent salt and found that MCDI is able to remove 20% more salt than CDI and MCDI in rV mode another 20% more.

4.7 FEM models

There are existing FEM models (see sec. 3.2) for CDI, which describe the mass transport of the ions through the cell in behalf of diffusion, migration and convection (sec. 3.3.1) in a fully discretized space. For instance, Hemmatifar et al. (2015) shows a solution to these equations in two dimensions for the first time. They couple double layer equations in the electrodes with transport equations for the flow in between. Hereby three parameters are used, which need to be defined empirically in practical experiments. These are a

micro pore capacitance, depending on the micro- and macro porosity, an additional non electrostatic ion attractive potential and the macropore porosity.

These fixed parameters are valid throughout all calculations of different operations with the module. With the model, they can define salt adsorption capacity, near-equilibrium cumulative stored salt and charge efficiency. Hemmatifar et al. (2015) use for their experimental data constant charging voltages between $U_{\mathrm{ch}} = 0.4$-1 V and an influent salt concentration of $c = 20$ mM. The flow rate through the cell was $Q = 0.42$ mL min^{-1}. The solutions of the model can picture the experimental data in a single CDI cell and a constant voltage charge until the electrodes are fully loaded with ions, concerning time dependent salt adsorption and desorption. Furthermore, they state the electrical resistance between current collector and active carbon electrodes as the highest and thus the only considered electrical resistance in the system (see also fig. 3.4). No statements of calculation time needed was made.

Jeon et al. (2011) introduce an FEM-model for the adsorption by the spacial resolution of single cavities as pores. This study focused only on the theory and no experimental data for the model evaluation was used. Here, the Poisson and Nernst-Planck equations were used (sec. 3.3.1) to calculate salt removal from a solution flow. It was found that to reach convergence, the equations have to be solved coupled-implicit (sec. 3) and not decoupled. Furthermore, a careful approach for the relation of pore size and salt removal rate and thus potential relative costs have been made.
This model can only be considered as basic and needs more further development for a use as calculation tool.

4.8 Comparison of different computational procedures

4.8.1 Theory

Ramachandran et al. (2018) presents a comparison of a numerical, semi-analytical and analytical model (see sec. 3). For the numerical approach they use the mathematical description of the GCS model (sec. 2.1) plus a so called Coulombic efficiency

$$\eta = \frac{J_{\mathrm{ion}}}{J_{\mathrm{charge}}} \ , \tag{4.16}$$

which is implemented due to the leakage currents (not used for desalination) according to the FBV equation (eq. 4.14).
In their semi-analytical model they approximate this η being constant and to calculate the DEBYE length from the GCS model, the latter is simplified with an RC equivalent. This reduces the number of ordinary differential equations (ODE) in the system and it can be solved semi-analytically.
In the analytical approach they assume also λ_D to be constant, which further simplifies the equation systems into algebraic expressions.

4.8.2 Study results

As an experimental setup, Ramachandran et al. (2018) used five pairs of active carbon electrodes with a thickness of $\delta = 300$ µm. As influent salt water, they used a KCl solution with $c = 20$ mM. The volume flow was varied between $Q = 3 - 12$ mL min^{-1}and the constant electrical charging current between $I = 50 - 100$ mA.
Eventually the numerical model was used to fit the (semi-)analytical approaches. The models where evaluated correctly with the absolute salt removal of experimental data and partly with the specific energy consumption of a CDI cell in CC mode. All models could picture the effluent salt concentration with different Q correctly. The *SEC* value was predicted as linear depending on the cell minimum voltage, however was increasing in the experimental data. Furthermore, they showed that the effluent concentration characteristics do not differ with same I_{ch}/Q ratios. The analytical model shows that the charge efficiency during constant current operations is mainly depending on the given voltage thresholds and not much on $I_{\mathrm{ch}}$and$Q$ as well as the *SEC* values only differ when Q or I_{ch} was changed.

4.9 Other studies combining models

4.9.1 Theory

A combination of models for flow by MCDI is presented by Hassanvand et al. (2017). They use the modified Donnan model for ion adsorption (sec. 4.3), Nernst-Planck-Poisson equations (sec. 3.3.1 for the concentration in the bulk and the IEM model (sec. 4.6) for the membranes. As simpflifications, they assume same chemical potentials

and thus relative ion activities at the interfaces to the membrane as in the solution diffusion model for reverse osmosis problems (eg. Rautenbach, 1997; Hoinkis, 2015) and the electrical potential in the spacer to be linear, due to its small thickness. Thus, the electrical potential of the POISSON equation (eq. 2.2) across the spacer can be approximated to

$$\frac{\partial \phi}{\partial y} \approx \frac{2\,\Delta\phi_{\text{spacer}}}{\delta_{\text{Spacer}}} = \frac{I}{\kappa_{\infty}} \tag{4.17}$$

and thus equalized to the ratio of the electrical current I and the conductivity κ of the bulk solution (see eq. 2.16).

4.9.2 Study results

Hassanvand et al. (2017) use home made porous carbon electrodes ($\delta = 150$ µm) and IEMs from *Neosepta* (AMX, CMX), to form a flow by MCDI cell with one pair of electrodes. As model water they used a NaCl solution with $c = 10$ mM. To verify the model, the effluent salt concentration was measured and compared with the results of the transport model. The results show an agreement of the model with their time-dependant experimental data. To fit the model the three parameters μ_{att}, C_{St0} and α (additional attractive adsorption potential, STERN layer capacitance at zero cell voltage and charge dependence of STERN capacitance) need to be manually adjusted. Furthermore, they vary the water flow and thus influence the residence time of the water volume in the electrode cell and show that there is a maximum residence time, when not more salt is adsorbed and only the water recovery (eq. 2.22) is decreasing.

The same models were used successfully beforehand by Dykstra et al. (2016) for modelling desalination process of a MCDI CC operation. They used a KCl solution with concentrations of $c = 20$ mM, $c = 100$ mM and $c = 500$ mM, which is led through the four MCDI cells with $Q = 7.5$ mL min^{-1}per cell. The constant current was varied between $I = 0.25 - 1$ A and the maximum cell voltage was at $U = 1.4$ V. The model agreed with time-dependent effluent salt concentrations and cell voltage distributions. For the mass transport inside the spacer they descretized the room in only few subcells in flow direction and solved the ion transport with the simple concentration balance in these elements. The other PDEs were solved only for the direction perpendicular to the flow direction, hence towards the electrode and current collector. The goal of this study was to highlight the resistances in different parts of the MCDI cell and compare it with different electrode thicknesses. They found, that the highest resistance is in the

spacer and in the external connectors as well as that a different electrode size does not play a relevant role towards it. However the latter increases desalination time but does not decrease energy needed for desalination. No statement was made concerning the calculation time.

4.10 Summary of state-of-the-art models and conclusion for model selection

The literature review of the existing models for (M)CDI modules (sec. 4.1 - 4.9) reveals many different approaches pursuing different goals. A summary can be found in tab. 4.3.

Table 4.3. Overview of existing MCDI models

Advantages (+)	**Disadvantages (-)**
RC&Z models (e.g. Andres et al., 2017; Suss et al., 2013)	
+ easily scaleable,	- no desal. behaviour
+ analytical solutions	- no desal. efficiency
+ electrical behaviour	
+ material design	
IEM models (e.g. Biesheuvel et al., 2011a; Dykstra et al., 2016, 2017)	
+ incl. extra resist. to MCDI	- more calculative effort
+ more accurate ion transport	- more approx. errors
+ especially relevant for multivalent salts	
RSM (Jeong et al., 2020)	
+ quick and easy calculation	- limited accuracy
+ extrapolation of experiments possible	- valid for one exp. setup
	- many practical tests needed

Transport models (NPP)

(e.g. Dykstra et al., 2016; Hassanvand et al., 2017; Ramachandran et al., 2018)
(Hemmatifar et al., 2015; Jeon et al., 2011, ...)

+ physically accurate description of ion transport	- high calculative effort (numerical approach) possible
+ proven validity in many studies	- only EDLC effects considered

mD model

(e.g. Dykstra et al., 2016; Wang et al., 2018a; Hassanvand et al., 2017)
(Biesheuvel et al., 2014; Porada et al., 2020, ...)

+ sufficient accuracy for lab scale (M)CDI	- empirical determination of system depending coefficients
+ semi-analytical approach possible	
+ low calculation times	- convection, diffusion and electrostatic migration not considered

amD model

(e.g. Biesheuvel, 2015)

+ simplified approach for additional attraction potential from mD	- same disadvantages as mD

Models for faradaic reactions

(e.g. Biesheuvel et al., 2011b; Dykstra et al., 2017)

+ defines non electrostatic attraction forces	- high calculative effort
+ higher accuracy in results possible	- high evaluation effort
	- highly depending on feed water quality and ambient conditions

FEM models

(e.g. Hemmatifar et al., 2015; Jeon et al., 2011)

+ spacial discretized solution	- calculation intensive (time)
+ time dependent and cyclic solutions possible	

Combined models

(e.g. Ramachandran et al., 2018; Hassanvand et al., 2017; Dykstra et al., 2016)

+ accurate for holisitc approaches	- calculation intensive (time)
+ adjustable for different input parameters	- approximation errors can sum up
+ includes all relevant physics	

The state-of-the-art-models of (M)CDI cells, calculate the salt concentration in the single parts of the module (spacer, IEM, porous electrode) and energy consumption using different operational parameters. These models can reproduce the experimental data gained from tests of laboratory scaled MCDI plants. If the desalination behaviour is modelled, it mostly reveals cumulative salt adsorption after a CV operation in an equilibrium state of the cell. Some (Dykstra et al., 2016; Hassanvand et al., 2017) show time-dependant effluent concentrations with an out-of-lab-application preferred CC operation and can calculate the SEC of the system (Ramachandran et al., 2018). However thereby, they pursue the goal of highlighting material behaviour or improving single parts inside an MCDI module. What is still missing is a model, which can predict the performance and energy consumption holistically of entire MCDI modules (for small scale or industrial applications) to help optimizing operational parameters, for designing water treatment plants (Suss et al., 2015; Dykstra et al., 2016) and which can be used in an easy to handle calculation tool. Furthermore, no model studied the water flow through different geometrically shaped modules, which is the carrier medium of the salt and as Hassanvand et al. (2017) found, its retention time between the electrodes does influence the desalination performance.

MCDI in water treatment applications is usually not operated in single pass modes, but in periodically changing charge and discharge cycles, as the quality of the diluate is the most important parameter when it is needed for a certain purpose (drinking, washing, process cooling, etc.). For this reason, the most common operation is in constant current charge and discharge mode, while the desalination step is ended when the target of the water quality is exceeded and the regeneration step when most of the ions are flushed out of the system. In between, a transfer step is needed to not contaminate the diluate with the concentrate.

For these realistic applications, the strived models in this thesis have to be valid. The main objective is to develop and test a combined easy-to-use model for the design of technical MCDI modules. In this connection particularly calculation of salt removal efficiency and specific energy consumption (SEC), by varying operational and constructive parameters is addressed.
The application of these models on commercial available MCDI modules is studied and approaches to implement them into a design and calculation tool are stated. This calculation program shall be a decision-helping tool for designing water treatment plants with included MCDI modules.

5 Materials and methods for implementation of theoretical models

In this chapter, the materials and methods used for modelling the water treatment processes in this thesis are introduced. This comprises the implementation of the theoretical approaches expressed in equations into the simulation software.

The literature review in chapter 4 narrows down existing models in sec. 4.10. The models, which are further used in the thesis are based on the

- Nernst-Planck-Poisson equations
- (improved) modified Donnan model and
- Navier-Stokes equations for computational fluid dynamics (CFD),

to translate the physics highlighted in fig. 3.4. Their implementation in this MCDI environment is concluded in fig. 5.1.

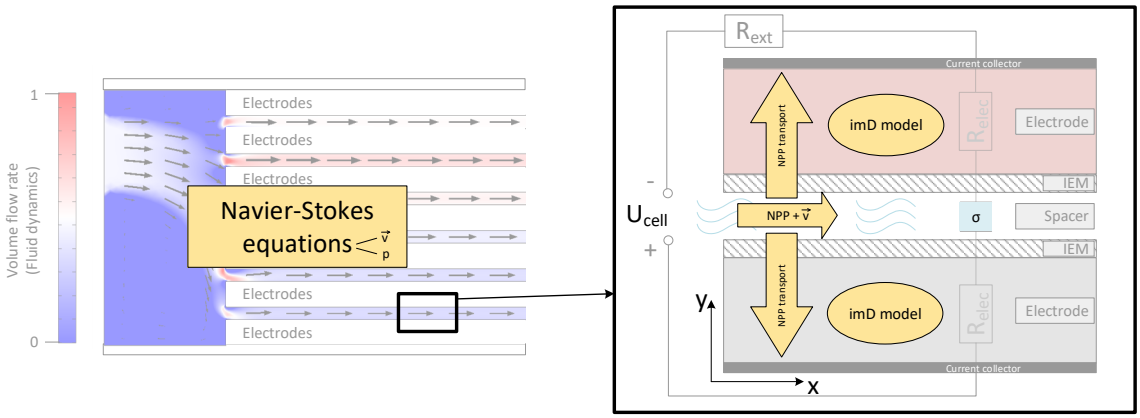

Figure 5.1. Used models and their implementation in the MCDI environment

Nernst-Planck-Poisson equations, describing convection, diffusion and migration (sec. 3.3.1), are the basic mathematical expression of ion transport in an MCDI module and essential for description of its time-dependent ion transport. They are successfully used in many studies, especially in the combined modules (tab. 4.3). To solve these PDEs, high computation times are needed. However, if suitable simplification steps are made, they can be reduced (see sec. 8.3.2).

(Improved) modified Donnan model is used, due to its broad application and proven validity, as a simplified and semi-analytically computable model (sec. 4.3) for the adsorption process. The calculation times are much lower than if the POISSON-BOLTZMANN equations are used to model the EDL spacially in the carbon electrodes and the accuracy is high enough for the range of salt concentration, the MCDI is used to desalinate brackish water (see tab. 4.2).

Navier-Stokes equations are used for the water flow through the MCDI module, as being well established (sec. 3.3.2) and the standard equations for most CFD problems.

As an overview, tab. 5.1 is listing all carried out simulations.

Table 5.1. Overview of simulation work carried out

No.	Method	Geom.	Physics	Variables
I	Analytical	0D	Electrosorption	Voltage, concentration
II	FEM	1D	Ion tranport	Spacer width, voltage, concentration
III	FEM	2D	Ion tranport	gPDE -interface
IV	FEM	2D	Fluid flow	Geometry, volume flow
V	FEM+Analytical (modelling tool)	2D	Fluid flow, ion transport, electrosorption	Voltage, amperage, concentration, volume flow
VI	Analytical (modelling tool)	0D	Electrosorption	Voltage, amperage, concentration

In this simulation work, following goals were pursued:

1) To evaluate the models in the simulation tool's environment, meaning if the tools are suitable for implementing and solving appropriate equations (sim. II and III)

2) to assess, how the already existing models for home built, very small scaled MCDI cells (as presented in sec. 4), are applicable on bigger scaled MCDI modules (≥ 75 pairs of electrodes) and for water treatment typical applications (sim. I - IV)
3) to present differences in retention time of single pairs of electrodes in a holistic CDI module and point out constructive optimization potentials (sim. IV)
4) to create the base for a calculation tool (sim. V and VI).

5.1 Simulation tools

To process the iterative and numeric calculations of the theoretical models, computation devices and appropriate software are needed. The PC used, specifically the enclosed central processing unit (CPU) and the installed random-accessed memory (RAM) are the critical elements, which mainly determine the calculation times and feasibility. All calculations are done with an Intel(R) Core(TM) i7-8650U CPU at 1.90 GHz, using 4 cores on 1 socket and an available RAM of 16 GB.

5.1.1 Spreadsheet program

For the semi-analytical computation (see. 3.1) of the mD-model, the spreadsheet program *Microsoft Office Excel*[1] was used. With this program, linear equation systems and also transcendental functions can be solved. The tabular principle in the spreadsheet program was used for solving equations iteratively either manually, by solving equations in several rows, using the results of a row as an initial value for the calculation of the equation in the next row again. This can be repeated until no change in the result can be determined anymore and hence the error to the result is below an acceptable value. Furthermore, the so called *goal seek function* available in most of the spreadsheet programs was used as an alternative, which does the latter explained automatically. Hereby also the maximum interation number and -error can be set.

5.1.2 FEM and multiphysics simulation software

To compute non-linear systems of differential equations, in a multidimensional spacial extent, an FEM simulation software is needed. Therefore, the program *COMSOL Mul-*

[1] www.microsoft.com/en-us/microsoft-365/excel

tiphysics™ v5.6 [2] was used. In this program, ordinary-, partial differential- and also implemented equations can be used and combined (COMSOL AB, 2017c). Furthermore, *COMSOL Multiphysics™ v5.6* (subsequently also called COMSOL) allows the coupling of different equations of physical problems in one study, with different study steps. Additionally, it possesses an *Application Builder*, which enables the possibility to create executable subprograms of the simulation. Hence, it is an optimal solution to combine different models and developing designing tools. The software provides preprocessing, geometry and domain building implements as well as detailed mesh building and analysing tools. For the post-processing, the results of domains and boundaries can be analysed and appropriate diagrams, surface maps and tables can be created and exported.

5.2 Methods for model implementation

In this section, the methods of how basic equations and existing models (ch. 2 and ch. 4) were implemented and translated in the simulation programs are explained. Hereby, different approaches have been used for the FEM simulating- and the spreadsheet program.

5.2.1 Equation implementation in *COMSOL*

The software allows to built equations fully manually or to use implemented versions of most used types of equations. To compare the outcome of the different usages, the NERNST-PLANCK equation was set up with the *General Form PDE*-interface (gPDE). The POISSON equation was set up with a gPDE or the inbuilt *Poisson's Equation*-interface (POeq) and the already implemented *Electrostatics*-interface (ESI). The inbuilt forms of the equations suitable for modelling of the NPP are listed as follows in tab. 5.2.

Hereby, the implementation of the NERNST-PLANCK-POISSON equations (eq. 3.10 and eq. 3.11) was done as follows:

1. **gPDE**: The coefficients e_a and d_a are damping factors of the time derivative part of the PDE, u the dependent variable of the equation and Γ the space derivative

[2] www.comsol.com

Table 5.2. Forms of inbuilt equations of *COMSOL Multiphysics™ v5.6*

Pos.	Interface	Equation
1	gPDE	$e_\mathrm{a}\,\frac{\partial^2 u}{\partial t^2} + d_\mathrm{a}\,\frac{\partial u}{\partial t} + \nabla \cdot \Gamma = f$
2	POeq	$\nabla \cdot (-c\nabla u) = f$
3	ECI	$E = -\nabla V$, with $\nabla \cdot (\epsilon\, E) = \rho$

part. At the right hand side of the equation, a source f can be added. For the simple NPP implementation the damping factors and f need to be set to zero. Γ is the flux J and hence

$$\Gamma = -D \cdot (\nabla u + u \cdot \frac{z\,F}{R\,T} \cdot \nabla V) + u \cdot v_f \tag{5.1}$$

with $u = c_\mathrm{i}$, $V = U$ and v_f being the velocity field, which was set to constant in x- and 0 in y-direction or the solution for velocity of the CFD simulation was taken (see fig. 5.1). For time-dependant studies, the damping factor d_a was set to 1 for implementing a time derivation. This includes Fick's second law (eq. 3.2), which shows the variation of concentration over time. To damp this derivation, a value below 1 can be inserted. To simulate a transport through porous media, d_a was set equal to the porosity of the material (as stated in Dykstra et al. (2016)). The electrical potential V is overtaken by *POeq* or *ECI*, which were solved coupled. The *gPDE* was also used for setting up the Poisson equation, by defining $e_a = d_a = 0$ as well as

$$\Gamma = \nabla V \quad \text{and} \tag{5.2}$$

$$f = -\frac{\sigma}{\epsilon_0\,\epsilon_r}, \tag{5.3}$$

whereas $\sigma = z\,u\,F$. In COMSOL, 2D calculations were carried out and thus ∇ equals to derivatives in two directions (x and y). For every direction eq. 5.1 was translated to the COMSOL syntax into

```
Gamma(x) = -D*(ux + u*z*F/R/T * Vx) + u * vf
Gamma(y) = -D*(uy + u*z*F/R/T * Vy) + u * vf ,
```

eq. 5.2 into

```
Gamma(x) = Vx
Gamma(y) = Vy
```

and all the other coefficients accordingly.

2. **POeq**: The inbuilt POISSON equation was used to compare differences in the outcome towards the gPDE, while c was set to 1 and f according eq. 5.3.
3. **ECI**: The *Electrostatic*-interface offers the POISSON equation, by combining both equations from tab. 5.2, with ρ in COMSOL being σ in this thesis:

$$\nabla(-\epsilon_0\,\epsilon_r\nabla V) = \rho \mathrel{\widehat{=}} \nabla^2\phi = -\frac{\sigma}{\epsilon_0\,\epsilon_r} \tag{5.4}$$

For the CFD simulation, the standard laminar flow node of the *Single Phase Flow*-interface (SPF) was used, since the critical Reynolds number for gap flows is only exceeded with a volume flow of (see eq. 2.18 - eq. 2.21)

$$\dot{V}_{\text{crit}} = v_{\text{crit}}\,A > \frac{Re_{\text{crit}}\,\nu}{L_{\text{gap}}}\,A = \frac{2200\cdot 10^{-6}\,\frac{\text{m}^2}{\text{s}}}{4\cdot 10^{-4}\,\text{m}}\cdot 3.2\cdot 10^{-5}\,\text{m}^2 = 0.176\,\frac{\text{L}}{s} \tag{5.5}$$

in between a single pair of standard electrodes (*Voltea* C3, see sec. 6.1), with $\nu = 10^{-6}\,\text{m}^2\,\text{s}^{-1}$ (VDI-Gesellschaft, 2013) and thus for the whole module $\dot{V}_{\text{crit}} > 75\cdot 0.176\,\text{L}\,\text{s}^{-1}$ $\approx 792\,\text{L}\,\text{min}^{-1}$, which is assumed to be never reached in application (see sec. 2.2).
In the models in this thesis, the space in between the electrodes is assumed to be empty and not filled with a woven spacer mesh (see sec. 2.3.2), hence a laminar flow is considered.
Nevertheless, comparison calculations were carried out with including the k-ϵ-turbulence model (see sec. 3.3.2), since the flow profile is further dependant on the inflow conditions of the gap (Bohl and Elmendorf, 2014; VDI-Gesellschaft, 2013). The SPF is using the NAVIER-STOKES equations (see sec. 3.3.2).

5.2.2 Pre-processing and solver settings in *COMSOL*

In this section, pre-settings next to the equation implementation (sec. 5.2.1) as well as domain- and boundary definitions for the FEM simulation are presented.

Global parameter definitions

Firstly, all parameter and constant variables definitions can be found in tab. 5.3, which were set in COMSOL as global definitions and used in further calculations. The values are either known from *Voltea* (sec. 6.1) or taken out from literature (e.g. VDI-

Gesellschaft (2013); Dykstra et al. (2016); Biesheuvel et al. (2011a)). In this table,

Table 5.3. Defined constants for the FEM simulation

Pos.	Variable	Value	Unit	Description
1	`Dna`	2.00e-09	m^2/s	Diffusion coefficient of Na
2	`Dcl`	2.00e-09	m^2/s	Diffusion coefficient of Cl
3	`F`	96485	C/mol	Faraday constant
4	`R`	8.314	J/(mol K)	Gas constant
5	`T`	293	K	Temperature
6	`Cna_init`	20	mol/m^3	Initial Concentration of Na
7	`Ccl_init`	20	mol/m^3	Initial Concentration of Cl
8	`V_elec`	-1	V	Electric potential
9	`epsilon`	78.854e-12	F/m	Permittivity
10	`Mnacl`	58.5	g/mol	Molar mass NaCl
11	`Mna`	23	g/mol	Molar mass Na
12	`V_ramp`	1	-	Declared variable for ramping V
13	`U_T`	(R T)/F	V	Thermal voltage
14	`C_St`	1.49e+08	F/m^3	Stern capacitance
15	`zna`	1	-	Valency of Na
16	`zcl`	-1	-	Valency of Cl
17	`muatt`	0	-	μ_{att} initial value
18	`l`	0.08	m	Length of electrode
19	`A`	$0.08 \cdot 0.16$	m^2	Area of electrode
20	`I_cell`	20	A	Amperage initial
21	`R_ext`	0.027	Ω	External resistance

natural constants as R and F, the ambient condition T, material properties as D_{Na} and M_{NaCl}, geometrical variables as l and A of the electrodes, the solver controlling variable V_{ramp}, but also empirical determined constants as C_{St} and R_{ext} as well as model fitting parameters as μ_{att} are listed.

Domain area definition

Next to the global-, the domain definitions were set, which is first of all the calculation domain area Ω. As a first simplification, Ω was defined in a 2D space (for appropriate simulation of tab. 5.1), which is assumed to be sufficiently resolved, since no significant transport effects were expected to occur in the out-of-plane direction (z). Furthermore, 1D simulations were carried out to test the transport equations in a simplified domain to save computational effort, but also to evaluate the results, if they can be sufficiently picture the experimental data.

For the 1D environment in the FEM simulation, firstly a line of $l = 350$ µm was chosen, which is within the dimensions of the spacer thickness in MCDI applications (Biesheuvel et al., 2011a). The ends of it represent the electrodes, where *electrical potential* boundary conditions were set (see description below), hence only ion transport towards and away from those is observed. Furthermore, this simulation serves for examining the solver stability.

On a 2D view, all cross sections of the module's spacer along the axes of the Cartesian coordinate system are rectangles. The xy-plane indicated in fig. 5.1 was modelled. The smaller the domain, the smaller the calculation effort. Hence, a further simplification was made by modelling only half of one pair of electrodes for the ion transport problem for 1:1-salts (see pictured domain in fig. 5.2). It is assumed that symmetry is given for the

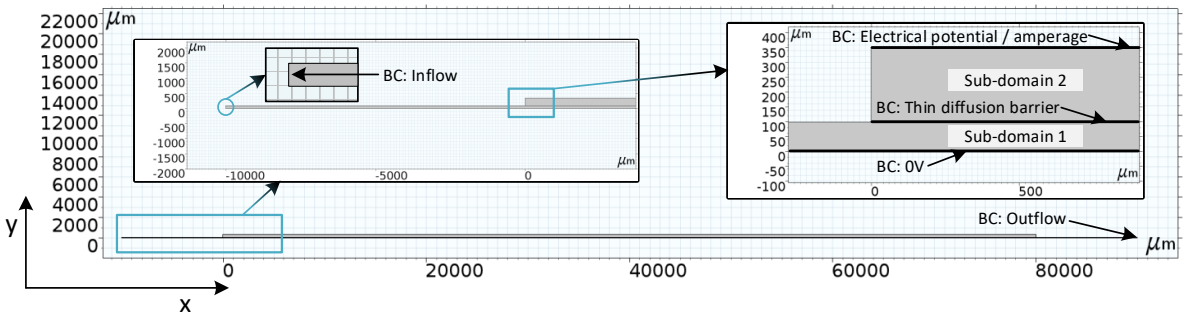

Figure 5.2. 2D calculation domain of half a pair of MCDI electrodes, for sim. III and V

ion transport and the electric field spanning from the spacer's midplane (at $y = 0$ µm) to the electrodes current collector (at $y = 350$ µm), if $c_1 = c_2 \wedge z_1 = -z_2$. Here, the half spacer possesses a thickness of $\delta_{sp} = 100$ µm and the electrode $\delta_{elec} = 250$ µm. The electrode has a length of $l = 8$ cm and before and after the electrode, a run in and out of the water of 1 cm was modelled. All geometric data was taken from above mentioned literature or from data given by the manufacturer.
In sub-domain 2 (Ω_2, see fig. 5.2) convection was not allowed and the appropriate term was neglected. In all other domains in sim. III and V, the diffusion, migration and convection node was activated.
Following boundary conditions were set:

Inflow: At the left end ($x = -10^4$µm) an *inflow* boundary condition (BC) was set, which is implemented by a DIRICHLET BC and sets a constant concentration at an inlet boundary. It does not define a velocity of the ions entering the domain. This is

modelled by a constant velocity variable or the solution of the CFD solution for v_f in Ω (see eq. 5.1 for the gPDE).

Outflow: The *outflow* BC was set by a NEUMANN BC, which basically sets the ion movement out of the domain due to diffusion to zero ($\vec{n}\,(\text{-}D\,\nabla c) = 0$) and only the convection is responsible for ions leaving Ω. Hereby is $\vec{n}$ the normal vector pointing out of the domain.

Electrostatic BC's: At the upper end of the electrode ($y = 350$ µm), a constant value for electrical potential was set (`V_elec` of tab. 5.3) with the *Electric Potential* node of COMSOL for the ECI and if CV operation was simulated. In this case for the POeq-interface, a *Flux/Source* node was set, which represents a ROBIN BC, where the NEUMANN part, in COMSOL also called *Absorption/Impedance Term* g_{Ne}, was set to zero and the DIRICHLET part g_{Di} was equalized to the fixed electrical potential:

$$\text{-}\vec{n} \cdot (\text{-}c\nabla u) = g_{\text{Di}} - g_{\text{Ne}}\, u \text{ , with } \; g_{\text{Di}} = \texttt{V\_elec} \; ; \quad g_{\text{Ne}} = 0 \tag{5.6}$$

For the simulations of CC operations, V_{cell} was set dependent on a constant I_{cell} and variable resistance values (see tab. 5.4), for the *Electric Potential* boundary node.

Due to only half a cell was modelled, V_{cell} needs to be halved as well. Furthermore, depending on which side of the pair is modelled, the sign was set to negative if adsorption of cations was simulated.

In the symmetry plane of the capacitor ($y = 0$ µm) the electrical potential was set to zero (respectively the *Flux/Source* node in the POeq interface).

IEM: The interface between electrode and spacer is a so called inner boundary, where in the MCDI module the IEMs are attached. In these membranes, the diffusion coefficient of the ions is changed due to the media they are dissolved in is different to water (sec. 4.6). Compared to the other parts of the cell, the spacial extension is very small. Thus, a *Thin Diffusion Barrier* node was set for this inner boundary, for which a barrier thickness $\delta_{\text{IEM}} = 15$ nm and a different diffusion coefficient $D_{\text{NaIEM}} = D_{\text{Na}} \cdot 0.05$ was defined. These values were taken from Dykstra et al. (2016), from which it is assumed that similar equipment was used to in this thesis. With this node, following equations are added to the system of for the calculation

points at this boundary:

$$-\vec{n}\, D\, \nabla c_1 = \frac{D_{\mathrm{IEM}}}{\delta_{\mathrm{IEM}}} (c_1 - c_2) \tag{5.7}$$

$$-\vec{n}\, D\, \nabla c_2 = \frac{D_{\mathrm{IEM}}}{\delta_{\mathrm{IEM}}} (c_2 - c_1), \tag{5.8}$$

where the indices 1 and 2 indicate the two sides of the membrane

The CFD modelling was carried out furthermore in a bigger scaled domain for analysing the water flow through the module and thus 75 pairs of electrodes were spacially resolved, according to the assumption for a C-3 module (see fig. 5.3). Hereby, the thicknesses of the spacers were varied.

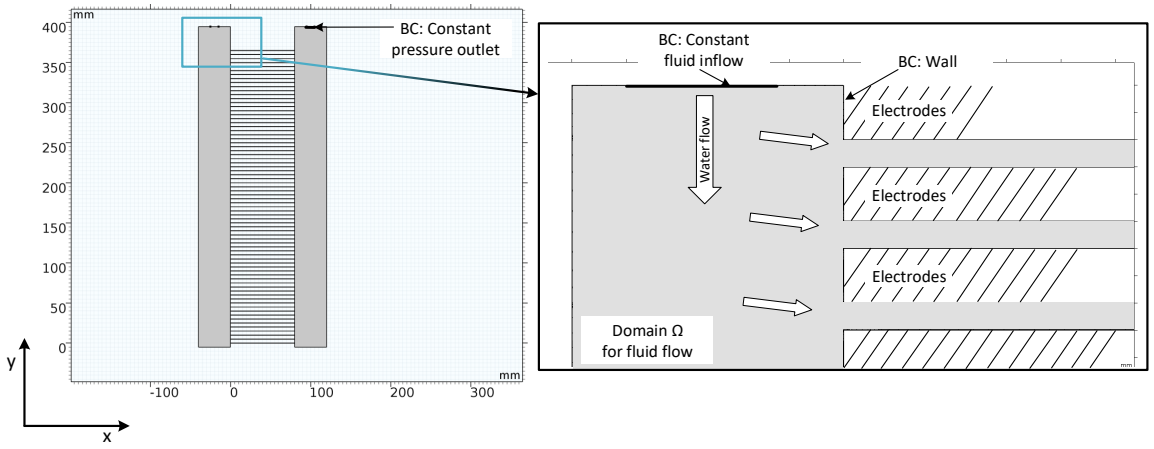

Figure 5.3. Cropped section of 2D calculation domain of flow by 75 electrodes for CFD sim. IV

Following boundary conditions were set:

Inlet: The *inlet* boundary condition, was chosen to be on the top (in geometry of fig. 5.3). It is a standard DIRICHLET BC, setting the velocity of the fluid constant and its vector of entrance to perpendicular to the boundary. In the geometry of fig. 5.2 the *inlet* BC was set at the same boundary as the *inflow* BC (for sim. V).

Outlet: The *outlet* BC was set to be a DIRICHLET BC as well, with a constant pressure of 1 bar absolute. Hereby, the backflow is additionally suppressed, meaning the outflow is not allowed to be negative. In the geometry of fig. 5.2 the *outlet* BC was set at the same boundary as the *outflow* BC (for sim. V).

Wall: The *wall* BC was automatically set to all other boundaries. Here, the *no slip* conditions was set, which simply defines $v_f = 0$ at this boundary.

Symmetry: In the geometry of fig. 5.2 (for sim. V) the *symmetry* BC was set at the same boundary as the *0V* BC. As a ROBIN BC it sets all shear stresses to zero and does not allow any flow in y-direction. Thus it behaves like an open boundary without any fluid leaving or entering the domain. At this edge, it is necessary, since only half the spacer is modelled and no wall is present at this boundary in the physical module.

Meshing

To discretize the domain in finite spacial elements, a grid with discretizing points over Ω was set up and optimized, to balance solving efforts with sufficiently approximated results (see sec 3.2.1), with the *Meshing* tool of COMSOL.

The mesh for the 1D geometry was built with $n_{\mathrm{me}} = 1500$ mesh elements, which were closer packed towards the electrode boundary. This was realized by decreasing the element size exponentially so that the element right next to the electrode is 1500 times smaller than the element in the middle of the line (see fig. 5.4). This so called *geometric sequence* distribution method was chosen because an exponential change of concentration towards the electrodes was expected (see sec. 2.1).

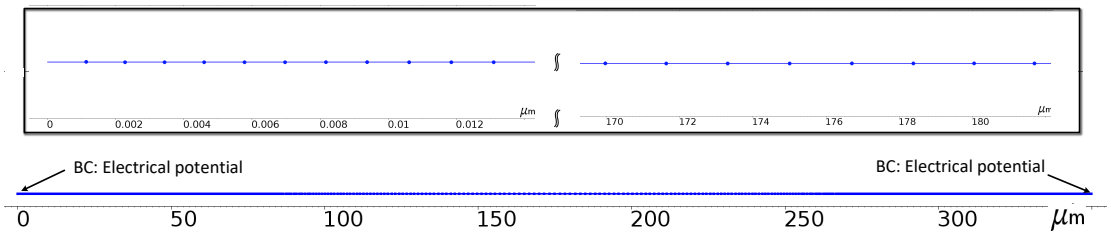

Figure 5.4. 1D calculation domain (blue) with indicated mesh points (for sim. II). Top: zoomed in areas of left boundary (electrode) and of the middle of the domain (spacer)

For the 2D geometry different meshes were used depending on the simulation carried out.

To minimize the calculation effort, n_{me} was kept as small as possible. Hereby, the grid was created very fine in y-direction and relatively coarse in x-direction, since the velocity alongside the electrodes was expected to be close to constant as calculated by the CFD simulation, on the view of one pair of electrodes or set constant in the gPDE for the convective part of the NP equation. After applying a mesh study, where the overall mesh was refined successively and the change of the results observed (see sec.8.3.2) a

mesh of geometry of fig. 5.2 with $n_{\mathrm{me}} = 10000$ elements was built as represented by the clipped section in fig 5.5. On both sides outside of this section, the mesh continues

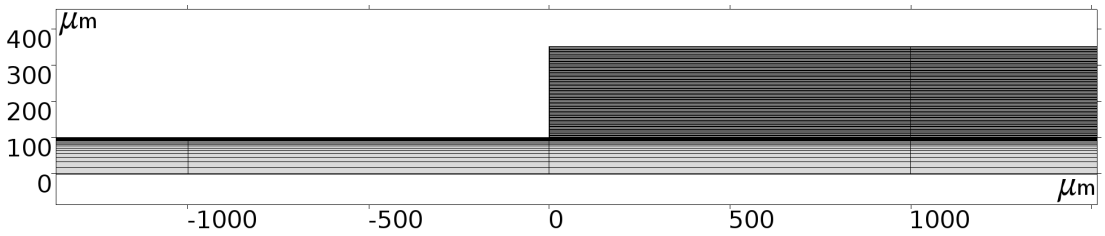

Figure 5.5. Clipped section of 2D mesh of the ion transport calculation domain for sim. III and V

unchanged. The very coarse resolution in x-direction forces a low area/length ratio of the elements, which is normally not wanted. Nevertheless does the mesh study and literature (Dykstra et al., 2016) show that the division in only few elements in water flow direction is valid and its calculations show reasonable results.

For the CFD simulation (sim. IV), the inbuilt triangle meshing tool has been used, to create a fluid simulation appropriate grid over the geometry (see fig. 5.6). Hereby,

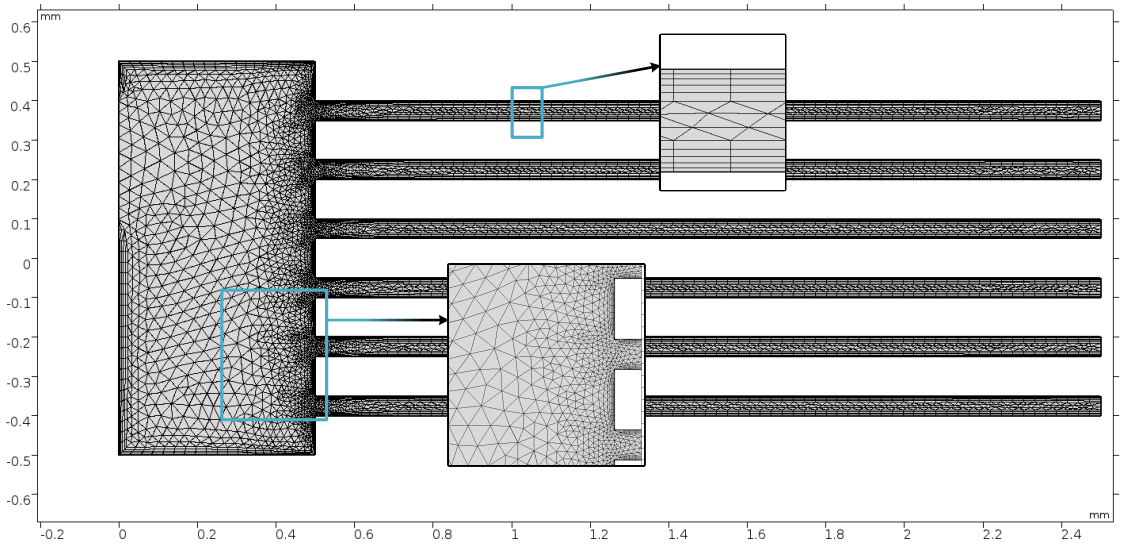

Figure 5.6. 2D mesh of the CFD domain in sim IV, created with the triangular meshing tool

mesh refinement nodes have been included to better resolve the flow at the spacer inlets, where more change and thus more iteration steps in the calculation are expected. Furthermore, boundary layers have been included close to the wall to match the boundary cell appropriately (see eq. 3.5). In the case of 75 pairs of electrodes, an amount of $n_{\mathrm{me}} = 338608$ elements was produced.

Solver settings

The software *COMSOL Multiphysics*™ *v5.6* allows several settings and adjustments for its inbuilt solvers.
Firstly, a sequence of solving steps was defined. If the CFD simulation was included, it was solved as a first step with a stationary solver, since no time-dependent changes were expected in the velocity field v_f, if the total water inlet volume flow is held constant during the desalination cycle. For the simple CFD simulation the standard inbuilt linear *parallel sparse* direct solver (PARDISO[3]) was used, which is pre-set by COMSOL. The NAVIER-STOKES equations were solved coupled with a automatic damped NEWTON's method (see sec. 3). The solution of the CFD modelling was used for the convection term of the NPP equations.
As a second step, a time-dependent solver was used, which calculates the electrical field (POISSON) and the ion transport (NERNST-PLANK) coupled. The so called *Multiphysics* node passes the electric potential of the POeq or ESI, to the migration term of the gPDE interface and the concentration vice versa. Furthermore, all global equations (tab. 5.4) have been solved together with the NPP equations, which solutions were needed as input for the electrode boundary.
As solver, the pre-set *multifrontal massive parallel sparse direct solver* (MUMPS) was used, with the use of pivoting, to find the variable best to solve for, in the equation system. This solver uses a lot of PC space memory (up to 56 GB) during solving the system (standard memory allocation factor of 1.2 was used) and can cancel calculation if the pivoting fails due to no pivot element has been found (with the set pivot threshold of 0.1). This can happen when inlet concentration or electrical potential as boundary conditions are set too high. In this case, the DIRICHLET BC's were ramped from very small values to the desired value over several steps of calculating the equation system, with the solution of the previous calculation being the initial values for the subsequent calculation.
The NPP equations were solved with a constantly damped NEWTON's method. The output time steps of the time-dependent solver were set to every half second between 0 and 1800 s. The internal time-steps of the solver using for the time derivative part of the equations (FICK's second law, see pos. 3 of tab. 5.2) were chosen automatically by the solver, with the backward differentiation formula (BDF, see eq. 3.4). Hereby, the maximum BDF order (maximum degree of the interpolating polynomial, COMSOL AB (2017b)) was set to 2.

[3] More information to the solver: `https://pardiso-project.org/`

5.2.3 Semi-analytical models

The semi-analytical models reduce the calculation time drastically. The main model used in this category was the mD or the imD model (see sec. 4.3). They were solved by the spreadsheet program *Microsoft Office Excel* and subsequently integrated in COMSOL.

Implementation in the spreadsheet program

For the spreadsheet program, the equations of the imD model are subsequently summarized.
For 1:1 salts as NaCl, $c_{\mathrm{sp,Na}} = c_{\mathrm{sp,Cl}} = c_{\mathrm{sp,NaCl}}$ is valid for the molar concentration. For this reason, eq. 4.4 can be changed to

$$\begin{aligned} c_{\mathrm{mi,NaCl}} &= c_{\mathrm{mi,Na}} + c_{\mathrm{mi,Cl}} = c_{\mathrm{sp,Na}} \cdot \exp\left(\text{-}\Delta\phi_{\mathrm{D}} + \mu_{\mathrm{att}}\right) + c_{\mathrm{sp,Cl}} \cdot \exp\left(\Delta\phi_{\mathrm{D}} + \mu_{\mathrm{att}}\right) \\ &= 2 \cdot c_{\mathrm{sp}} \cdot \cosh\left(\Delta\phi_{\mathrm{D}}\right) \cdot \exp\left(\mu_{\mathrm{att}}\right) \ . \end{aligned} \tag{5.9}$$

Furthermore is $\sigma_{\mathrm{mi,NaCl}} = z_{\mathrm{Na}} \cdot c_{\mathrm{Na}} + z_{\mathrm{Cl}} \cdot c_{\mathrm{Cl}} = c_{\mathrm{Na}} - c_{\mathrm{Cl}}$ and thus

$$\sigma_{\mathrm{mi,NaCl}} = \text{-}2 \cdot c_{\mathrm{sp}} \cdot \sinh\left(\Delta\phi_{\mathrm{D}}\right) \cdot \exp\left(\mu_{\mathrm{att}}\right) \ . \tag{5.10}$$

From eq. 4.6, the STERN potential can be derived to

$$\Delta\phi_{\mathrm{St}} = \frac{\text{-}\sigma_{\mathrm{mi}} \cdot F}{C_{\mathrm{St,vol}} \cdot U_{\mathrm{T}}} \tag{5.11}$$

If the electrical charge is positive, the ionic charge in the micropores will be always negative and so the STERN potential. The potential $\Delta\phi_{\mathrm{D}}$ always has the same sign as $\Delta\phi_{\mathrm{St}}$. Defined was that a positive voltage U_{cell} attracts ions in an MCDI system, furthermore $\sigma_{\mathrm{el}} = \text{-}\sigma_{\mathrm{mi}}$ is valid and a symmetry of electrodes as well as a 1:1 salt is present, meaning in the anode and the cathode the same absolute amount of ionic charge is adsorbed. Thus eq. 4.8 can be converted to

$$\Delta\phi_D = \frac{U_{\mathrm{cell}}}{\text{-}2 \cdot U_{\mathrm{T}}} - \Delta\phi_{\mathrm{St}} \ . \tag{5.12}$$

The four equations (eq. 5.9 - eq. 5.12) form the equations system which was solved in *Microsoft Excel* for different inputs of U_{cell}, c_{in} and material properties. Since eq. 5.9

depends on eq. 5.10, directly solving the system using eq. 5.10 - eq. 5.12 would cause a circular reference error in *Microsoft Excel*. Hence, as indicated in sec. 5.1.1, the *Goal Seek* function needs to be used to solve equation systems as the present, in the spreadsheet program. To use it, eq. 5.12 was converted to solve for U_{cell} and the value of $\Delta\phi_{\mathrm{D}}$ iteratively adapted with the *Goal Seek* function (see sec. 3.1), to match the solution of the converted equation with the input parameter U_{cell}.

The mD model with and without the additional attraction term μ_{att} as well as the imD model have been compared. For the first two, μ_{att} was adjusted to a constant value as to the solution agrees or set to zero. For the imD model eq. 4.10 was added to the spreadsheet and solved iteratively (see sec. 3.1).

The mD models for material properties definition

The mD models are firstly used to fit material property parameters and adjust the simulation results, while evaluating with experimental data. The salt adsorption capacity (SAC, Γ_{salt}) is calculated through c_{mi} as well as the micropore volume V_{mi} and mass m_{elec} with

$$\Gamma_{\mathrm{salt}} = 0.5 \cdot c_{\mathrm{mi}} \frac{V_{\mathrm{mi}}}{m_{\mathrm{elec}}} M_{\mathrm{NaCl}} \ . \tag{5.13}$$

Hereby the molar concentration $c_{\mathrm{mi}} = c_{\mathrm{mi,Na}} + c_{\mathrm{mi,Cl}}$ needs to be halved, due to it is multiplied with the molar mass of NaCl, to result in a mass concentration.
The SAR can be measured in the experiments (see sec. 7.2) and thus V_{mi} and m_{elec} or the density ρ_{AC} can be adjusted. Optimally, these parameters fit with the actual values of the datasheet or literature. A further parameter which is matched this way is $C_{\mathrm{St,vol}}$ of eq. 5.11.

Implementation of the imD model in COMSOL

To add a different adsorption behaviour to the ion transport model in COMSOL (in sim. V), the imD model was added to the simulation. This was done with the *Global ODEs and DAEs*-interface (glEQ, ODE = ordinary differential equation, DAE = differential algebraic equation). All global equations defined can be found formulated with COMSOL-syntax (COMSOL AB, 2017b, pp. 233) in tab. 5.4. The equations need to be declared in the scheme $f(u) = 0$ and a dependent variable u as well as its unit has to be defined. The latter plus the initial conditions u_0 of each equation for the iterative

calculation, are listet in tab. 5.5. To be in the scheme $f(u) = 0$, the variable u needs

Table 5.4. List of global equations in COMSOL for implementing the imD model

Pos.	u	f(u)=0
1	St	-St + (cdmi * F) / (-C_St * U_T)
2	Do	asinh(cdmi/(-2*Cna_init*exp(muatt)))-Do
3	Vma	-Vma + (Rma * I_cell) / (2 * U_T) / vma_ramp
4	Rma	-Rma + (1/cond) * (l/A)
5	V_set	-V_set + (-0.5) * (2*(Do+St+Vma)*U_T + I_cell * R_ext)
6	cond	-cond + ce * (Mna*1000) / 1000 * 2[m^3*S/(kg*m)] / 10
7	cmiDo	-cmiDo + 2 * aveop2(c1) * cosh(Do) * exp(muatt)
8	ce	-ce+aveop1(c1)
9	cdmi	cdmi - aveop1(c1) * zna

Table 5.5. Units and initial conditions of all global equations in the COMSOL simulation

Pos.	1	2	3	4	5	6	7	8	9
Unit	1	1	1	Ω	V	$\mathrm{S\,m^{-1}}$	$\mathrm{mol\,m^{-3}}$	$\mathrm{mol\,m^{-3}}$	$\mathrm{mol\,m^{-3}}$
$\mathbf{u}_0$	1	1	1	0	-0.1	0.1	0	0	0

to be included with a negative sign in most of the equations. It should be pointed out that the initial conditions u_0 of the here defined equations are not set to zero, if the variable is used in $f(u)$ as denominator in a fraction. The functions $f(u)$ were defined as follows:

Pos. 1 and 2: Defining `St` and `Do` as $\Delta\phi_{\mathrm{St}}$ and $\Delta\phi_{\mathrm{D}}$ in eq. 5.11 and eq. 5.9, while the latter is converted to solve for $\Delta\phi_{\mathrm{D}}$.

Pos. 3 - 6: `Vma` equals to the distribution of the electrical potential over Ω_2 according to Dykstra et al. (2016), which is basically a resistance over Ω_2 times the defined constant I_{cell} (OHM's law). Dividing by U_{T} makes it dimensionless. Together with `Rma` (pos. 4), which is the ionic resistance, it defines the variable `V_set` of pos. 5, which was used for the *electrical potential* boundary condition. The variability is created by the electric conductivity `cond` (pos. 6) defining the resistance `Rma`. Now a constant current simulation is possible. `V_set` is the sum of $\Delta\phi_{\mathrm{D}}$, $\Delta\phi_{\mathrm{St}}$ and `Vma` given the dimension V by multiplying with U_{T}. Added is the voltage from the external circuit, which equals to an external resistance `R_ext` and I_{cell}. Due to only one electrode of the pair is modelled, `V_set` is halved and made negative, as

to attract the cation Na^+. The `vma_ramp` is used to tune the voltage `Vma`, which is further explained in sec. 8.4.

Pos. 6 - 9 At pos. 8, `ce` is defined, which is the averaged ion concentration in Ω_2. Hereby is `aveop1` a defined global average operator of the sub-domain 2 and `c1` the concentration of sodium ions. This averaged concentration defines the electric conductivity in pos. 6. It was multiplied by the molar mass and by the factor 2 to convert the concentration with the dimension $g\,L^{-1}$ to $mS\,cm^{-1}$ (Walton, 1989) (see also sec. 6.2.1). Pos. 7 represents the c_{mi} calculated as of eq. 5.9, with `aveop2` being the average operator of the spacer. The charge density `cdmi` is defined to solve $\Delta\phi_D$ in pos. 2.

6 Materials and methods for practical experiments

For optimizing the MCDI desalination and evaluating modelling results, practical experiments have been carried out. In this chapter, the used material and proceedings of the experimental testing are explained.

6.1 Material of MCDI plant and laboratory equipment

6.1.1 Experimental setup

For the laboratory scaled experiments, the development kit (DK) of the company *Voltea B.V.* (meanwhile *Voltea Inc.*) was used as basic periphery together with different MCDI modules (see annex B on p. 160).
The DK includes a speed controlled diaphragm pump from *Lilie* (LS243155, 3.1 bar, 6.5 L min^{-1}), a cartridge pre-filter from *PENTAIR* (SWP1-10, 1 µm), one no-name paddle wheel flow sensor and one pressure sensor infront of the MCDI module as well as one electrical conductivity sensor (*JUMO*, type 202922, online) infront and one after the desalination electrodes. The signal of the conductivity sensors are transferred by measurement converters of *Thermo Scientific*, type Alpha COND 500. Behind the module, a 3/2 way solenoid valve (*Buerkert*, type 0124) is attached to lead the diluate and the concentrate flow in different directions. The total setup, together with MCDI module (*Voltea*, type C-5, see annex A on p. 158) and two tanks is illustrated in the P&I diagram and the pictures in fig. 6.1. To supply the MCDI module with a maximum of $U_{cell} = 2$ V and $I_{cell} = 60$ A, a power supply from EA, PSI 880-60 R is installed. All sensors were logged and the pump as well as the power supply are controlled via a *LabView* program.

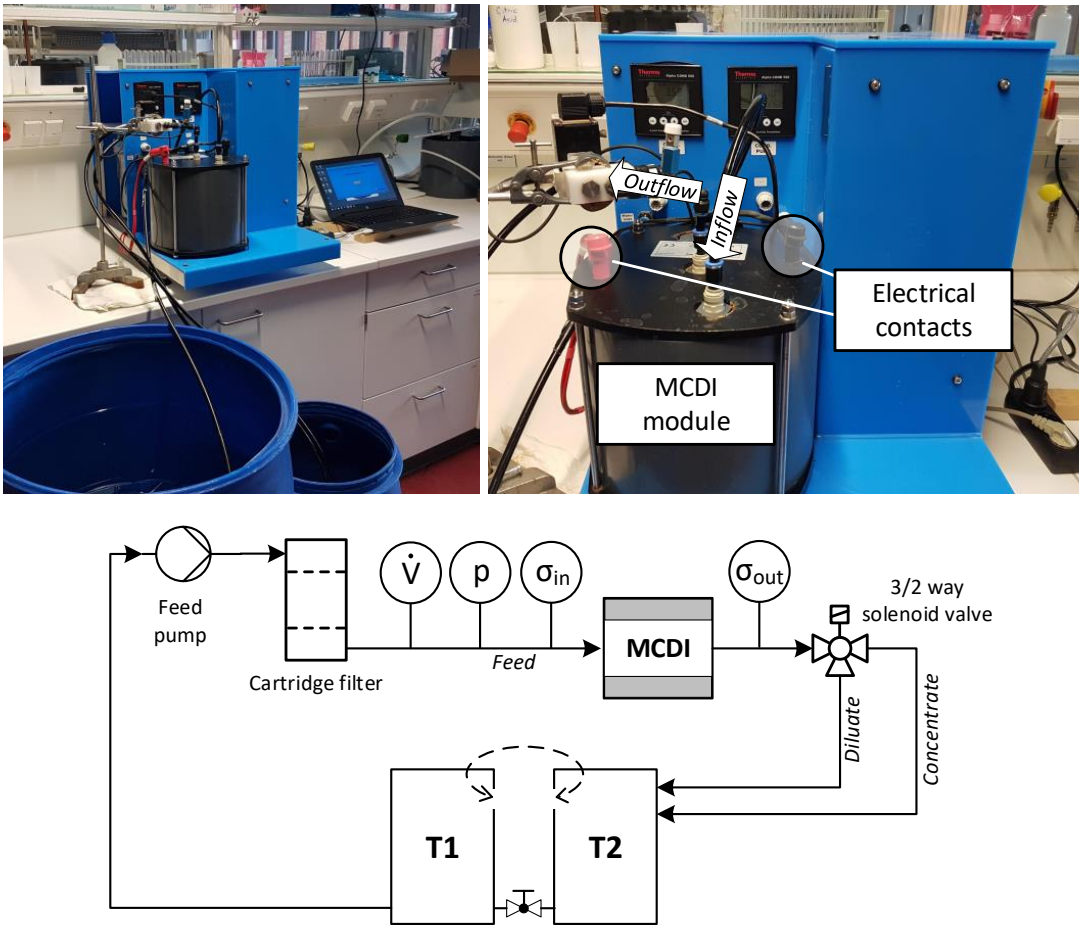

Figure 6.1. Experimental setup of the commercial MCDI module, development kit of *Voltea B.V.*, periphery and C-5 module plus the P&I diagram of the setup

The setup included two 50 to 200 L tanks, where one of which contained the model water and the other was collecting diluate and concentrate streams. After the feed tank was empty, inlet and outlet hoses were swapped. In the single pass experiments (see sec. 6.2.2) one 200 L tank was used, to which both outlet and inlet hoses where connected (inlet at the bottom, outlet at the surface), which is symbolized by the hand ball valve in fig. 6.1.

The DK includes a *LabView* program[1], which can monitor and log the measured data each second (of sensors shown in fig. 6.1) as well as control pump speed (thus $\dot{V}$), $U_{\max}$ and $I_{\max}$, for each charge, discharge and pre-charge phase (so called purify (P), concentrate (C) and pre-purify phases (PP)) and their durations.

[1] More information to the program at: `https://www.ni.com/en-gb/shop/labview.html`

The position of the solenoid valve (see fig. 6.1) as well as the sign of the voltage, which is reversed by relays (see switch in fig. 6.3) are defined for each phase as follows in tab. 6.1. This means that during the PP phase, ions are adsorbed, but the water is still lead to

Table 6.1. Definitions of voltage sign and valve position in different cycle phases

Phase	Voltage sign	Valve position
C	Negative	Concentrate
PP	Positive	Concentrate
P	Positive	Pure

the concentrate stream, since it does not meet desired quality yet. When the target concentration is reached, the valve position is changed and the P phase starts.

6.1.2 MCDI modules

Different modules were attached to the DK to observe the performance differences. The application and optimization tests were carried out with a C-3 module from *Voltea* (see fig. 6.2). The number of the module type stands for the amount of stacks of assumed

Figure 6.2. Two C-3 MCDI modules from *Voltea*. Left: old design, right: new design

25 pairs of electrodes each, with a quadratic shape and a side length of $b \approx 0.16$ m per electrode[2]. This concludes for the C-3 module a total amount of 75 pairs of electrodes

[2] Since commercial MCDI modules were used, not all constructive and material parameters were known, due to confidentiality reasons. Nevertheless, these aforementioned assumptions about the amount of electrodes and their side length fits to measurements and following official statements about electrodes total area.

and a total electrode area of $A_{\text{elec}} = 3.7\ \text{m}^2$ confirmed by *Voltea*. Further material properties as density and porosity, were approximated from Biesheuvel et al. (2011a, 2014); Dykstra et al. (2016), where as well *Voltea*-material was used and from which $\rho_{\text{AC}} = 0.55\ \text{g mL}^{-1}$, $\delta_{\text{elec}} = 220\ \mu\text{m}$ (thus $m_{1\text{elec}} = A \cdot \delta_{\text{elec}} \cdot \rho_{\text{AC}} = 3.1\ \text{g}$) and a micro porosity of $p_{\text{mi}} = 0.23$ was approximated. Subsequently these parameters were adjusted in the simulations, to fit experimental data (see also sec. 6.2.2) and compared again with literature to state the validity.
The attached IEMs contain sulfonyl groups for the cation- and quaternary ammonium groups as active functionality for the anion- exchange membranes.
The spacer material is assumed to be a woven material with a porosity of $p_{\text{sp}} = 0.7$.

The single-pass experiments (see sec. 6.2.2) were carried out with a C-5 module from *Voltea*, which have an active total electrode area of $A_{\text{elec}} = 6.2\ \text{m}^2$. The amount of electrodes is assumed to 125 pairs and all other parameters are the same as the C-3 module.

6.1.3 Electrical circuit of the MCDI development kit

To get an overview of the electrical circuiting inside the MCDI-DK, tests were carried out (see sec. 7.1), which revealed the circuitry illustrated in fig. 6.3. Hereby, only one

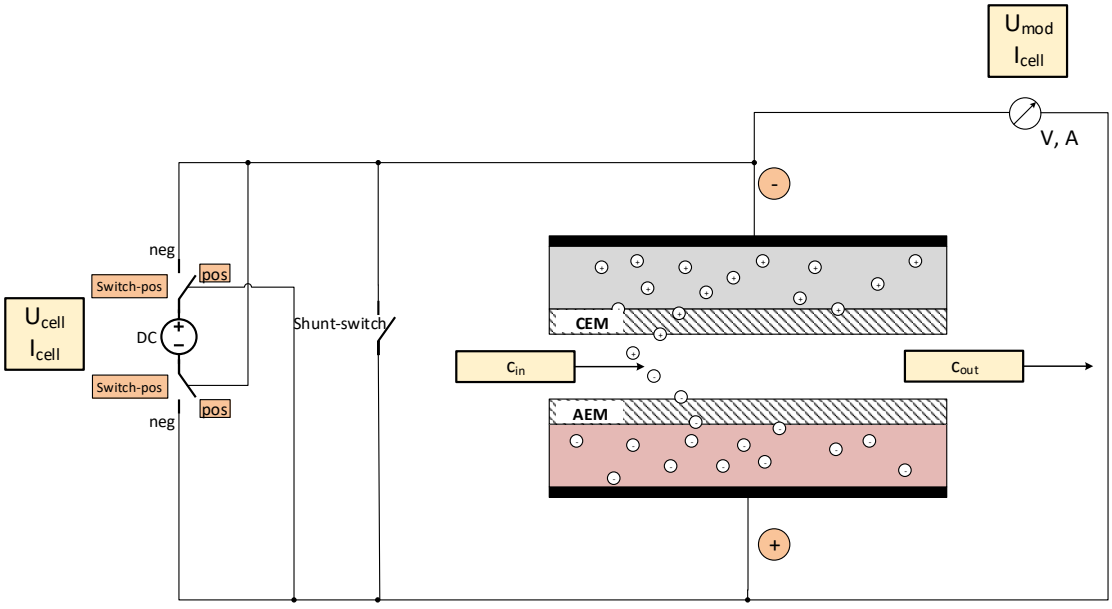

Figure 6.3. Schematic of electrical circuit of the MCDI development kit

pair of electrodes is highlighted. Positive and negative positions of the voltage- and opened or closed position of the shunt-switch are indicated. The position for charging the capacitor and thus desalinating the water is defined as positive. The negative switch position vice versa. To be able to flush the system without electrostatic effects, a shunt-switch is installed, which is furthermore used during cleaning procedures. It is possible to measure and log voltages directly at the power supply outlet and together with the electrical current at the module connectors. $U_{\max}$ and $I_{\max}$ can be set at the power supply. Next to it, the power consumption of the whole MCDI system was measured directly at the electric socket for the main power connection. Thus, subsequently three different main voltages were differed in U_{tot}, U_{cell} and U_{mod}, for main outlet, power supply outlet and at the module connectors, respectively.

6.1.4 Model water

As model water, sodium chloride (NaCl, purity $\geq 99\%$, Carl Roth GmbH + Co. KG) was diluted in deionized water (DI, produced with an ion exchanger from *TKA*, type DI 2800). The mixed solutions had molar concentrations between $c = 10$ mM $= 10$ mol m^{-3} and $c = 50$ mM. Due to the relatively high amount of water in the tanks (50-200 L) the water amount could only by approximated. After the addition of the weighed salt and mechanically stirring, the concentration was adjusted by adding more DI water or salt until the appropriate electrical conductivity was reached (see also sec. 6.2.1).
To measure the electrical conductivity in the tank a calibrated hand held sensor from the company *WTW* (type 315i) was used. When the correct salt concentration was reached, the MCDI module has been flushed with the water, while shunting the electrodes. Subsequently all inlet and outlet hoses were connected with the feed tank and the water was recirculated until salt concentration was balanced in the total system.

6.2 Methods and evaluation strategy

6.2.1 Correlation of electrical conductivity and salt concentration

To monitor the salt concentration at in- and output of the MCDI module and to adjust the model water solution, online electrical conductivity sensors have been used. To

convert the conductivity measurements to a salt concentration a conversion factor K between 0.5 and 0.9 was used (Walton, 1989) and

$$c = K \cdot \kappa \tag{6.1}$$

is valid, with c in $\mathrm{g\,L^{-1}}$ and κ in $\mathrm{mS\,cm^{-1}}$. Hereby, using $K = 0.5$ for $c < 1\ \mathrm{g\,L^{-1}}$ and $K = 0.64$ for $c > 1\ \mathrm{g\,L^{-1}}$ is recommended.
However, to define a certain conversion factor which fits for subsequent experiments, measurements were taken to determine the K-factor empirically (see fig. 6.4). Hereby,

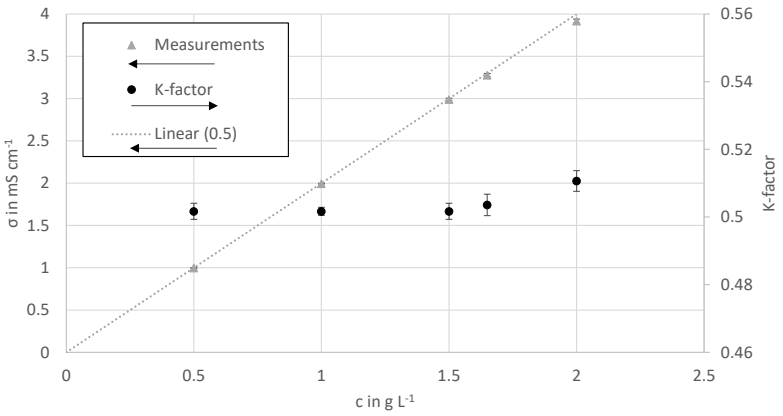

Figure 6.4. Measurements to asses the K-factor of NaCl solutions

an exact amount (*KERN* type 770 balance, with calibration value of 0.1 mg) of NaCl ($> 99.8\%$ purity) was weighed and diluted in 1 L (graduated cylinder) of DI water and stirred at room temperature. Subsequently the electrical conductivity was measured with the calibrated hand held sensor (see aforementioned).
It was observed that the K-factor remains below 0.51 up to a concentration of $c = 1.5\ \mathrm{g\,L^{-1}}$, $K \approx 0.51$ for $c = 2\ \mathrm{g\,L^{-1}}$ (for NaCl $c = 25.6$ mM and $c = 34.2$ mM respectively) and thus $K = 0.5$ was taken as general conversion factor for $c < 40$ mM ($2.34\ \mathrm{g\,L^{-1}}$) in this thesis.

6.2.2 Single pass tests

To examine the system's SAC, single pass tests were carried out. Furthermore they are helpful to evaluate the simulations done with constant input parameters and no phase changes (charge/discharge) are conducted.

Firstly, the system was fed with the model water ($c_{\mathrm{in}} = 10$ mM to $c_{\mathrm{in}} = 30$ mM) and negative voltage was applied until all ion were expelled from the electrodes. Subsequently, a CVC or CCC operation was initiated, with $U_{\mathrm{cell}} = 0$ V to $U_{\mathrm{cell}} = 2$ V and $I_{\mathrm{max}} = 60$ A or $I_{\mathrm{cell}} = 10$ A to $I_{\mathrm{cell}} = 60$ A with $U_{\mathrm{max}} = 1.2$ V and $U_{\mathrm{max}} = 1.5$ V, respectively.
Subsequently κ_{in} and κ_{out} were logged every second until $\kappa_{\mathrm{out}} \approx \kappa_{\mathrm{in}}$ and converted to a molar concentration in mM (eq. 6.1). After the measurements, the total salt adsorption (TSA, Δm_s) can be calculated as follows:

$$\begin{aligned} \Delta m_{\mathrm{s}} &= \int_t c_{\mathrm{in}} - \int_t c_{\mathrm{out}} \\ &\approx \bar{\dot{V}} \cdot \left[\bar{c}_{\mathrm{in}}\, t_{\mathrm{tot}} - \left(\sum_{t=n} (c_{out,n+1} - c_{out,n}) \right) \cdot \left(\sum_{t=n} t_{n+1} - t_n \right) \right], \end{aligned} \tag{6.2}$$

with c in $\mathrm{g\,L^{-1}}$and the SAC with

$$\Gamma_{\mathrm{salt}} = \frac{\Delta m_{\mathrm{s}}}{m_{\mathrm{elec}}} \quad . \tag{6.3}$$

The mass of electrodes m_{elec} of the latter equation was adjusted with the mD model (via ρ_{AC}, see eq. 5.13) and compared with literature values. Thus Γ_{salt} is the main parameter which was compared with the theoretical models and main indicator for the adsorption efficiency of an MCDI module.
Furthermore, the characteristics of voltage, amperage and effluent salt concentration were analysed while applying CC or CV operation for comparison with the simulation work.

6.2.3 MCDI optimization tests

Within this thesis, the MCDI technology was applied on realistic water treatment operations for drinking water production. Since almost no results for out-of-the-lab implementations exist in literature, the MCDI desalination with commercially modules was optimized empirically to generate realistic experimental data for larger scaled application (production of > 400 $\mathrm{L\,d^{-1}}$ of diluate) and the subsequent evaluation of the theoretical models. These tests were also used to compare SEC values of MCDI with reverse osmosis in literature.
For the MCDI optimization, the constant current charge and discharge (CCCD) process was chosen, since a constant diluate quality is needed for most of applied operation

categories. The focus of the experiments was to produce as much drinking water as possible from saline water (1 $\mathrm{g\,L^{-1}}$ – 2 $\mathrm{g\,L^{-1}}$ NaCl in DI water), with a low specific energy consumption (SEC) in kWh per $\mathrm{m^3}$ of product water.

A series of tests were carried out and successively operational parameters of C, PP and P cycles were changed as well as the input concentration. The influence of each parameter on the MCDI system is indicated in tab. 6.2. The goal was to remove enough salt that

Table 6.2. Influences of operational parameters on the MCDI system

Variable	Parameter	Effect
U_{max}	Max. voltage	Change size of double layer/ion capacity
I_{cell}	Electrical current	Change speed of ion migration
t_{phase}	Phase time	Adjust efficiency of respective phase and recovery rate
$\dot{V}$	Phase water flow	Adjust water volume which is desalinated per time unit/retention time

the averaged effluent conductivity $\kappa_{\mathrm{out}} < 900\ \mu\mathrm{S}\,cm^{-1}$ and thus $c_{\mathrm{out}} < 450\ \mathrm{mg\,L^{-1}}$ (see sec. 6.2.1) was reached, to comply with drinking water regulations of the WHO (WHO, 2017), recommending this concentration for NaCl, to achieve a so called "good" water quality.

After one full cycle was completed, the logging of data was started. The total test duration was between $t_{\mathrm{tot}} = 30$ min and $t_{\mathrm{tot}} = 6$ h. With the logged data, removal and recovery rate, power consumption and SEC, voltage and amperage characteristics as well as SAC and charge efficiency were observed and calculated.
The results of these experiments were used to evaluate the theoretical models with realistic data of applied MCDI operation.

7 Results and discussion of practical experiments

The developed model concepts in this thesis shall picture the desalination behaviour of real MCDI plants. Theoretical models have to be always verified by experiment studies, to confirm the accuracy of the results. Furthermore, experimental optimization of MCDI operation with realistic use cases, as drinking water production, was carried out, to generate realistic data the models can be compared with.
In this chapter, the results for the experimental testing is highlighted.

Empirical testing with lab- and pilot scale MCDI plants were carried out to study the performance of the desalination method and examine the charging and discharging behaviour of the deionization capacitor. Furthermore the theoretical model is evaluated with practical results of desalination units, which are also used in small scale applications outside of laboratory research (Voltea Inc., 2021). Hereby, different operational parameters are set, to simulate different environmental conditions and the response of the MCDI unit is recorded. Another purpose for gathering experimental data is to determine material properties, which are not given by the manufacturer, but needed for theoretical models.

7.1 Pre-tests for electrode behaviour

To get an overview of the electrical behaviour of applied MCDI modules and for analysing the electric response, pre-tests have been carried out with a C3 MCDI module from *Voltea*. Therefore, typical operating points in the electric circuit (see fig. 6.3) are set, which can be altered for optimizing an MCDI desalination. These are indicated in fig. 7.1. Only the yellow marked fields in the figure are visible measurements and thus known. The electrical circuit schematic has been created as an assumption resulting from these measurements and the following described electric behaviour. In fig. 7.1 the

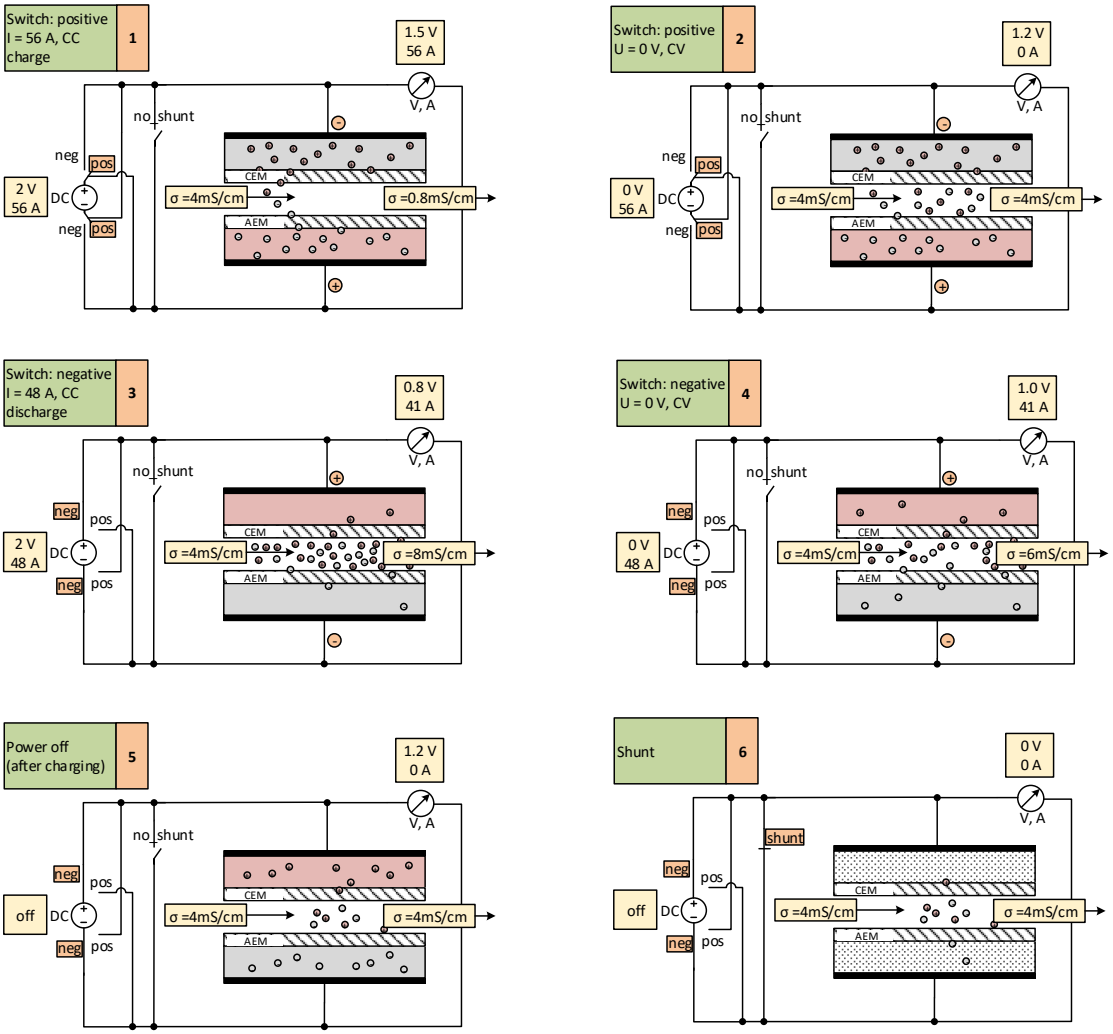

Figure 7.1. Electronic response of the MCDI development kit after applying six different configurations

electrical and ionic current is highlighted for different positions of the voltage switch and power supply settings. Hereby, the configurations 1-6 are applied successively and picture example settings for demonstration. The measured data of voltages and currents as well as the electrical conductivity are snapshots during each phase, to illustrate the typical behaviour of an MCDI cell and can be described as follows:

Setting 1: The maximum voltage $U_{\max}$ and electrical current $I_{\max}$ are set at the power supply to 2 V and 56 A respectively and are indicated next to the power supply in the schematic of the electric circuit. The voltage switch is set to positive, which means that the capacitor is charged appropriately that ions can be adsorbed in

the electrodes, which is determined by the IEM installation. It is noticed that the voltage U_{mod} measured directly at the module is constantly smaller than at the power supply outlet U_{cell}. This is due to inter alia external resistances as cables and connectors in between power supply and the pairs of electrodes. Like expected, the current at the power supply equals the current directly at the module, $I_{\mathrm{PS}} = I_{\mathrm{mod}}$. If the voltage U_{cell} at the power supply, is set high enough, so it is not reached immediately within the first seconds, I_{max} is the limiting factor and the process is called constant current charge (CCC). At the outlet, the measured conductivity is constant and lower than at the inlet.

Setting 2: Subsequently, $U_{\mathrm{max}} = 0$ V is set and the switches remain as before. Now, $U_{\mathrm{mod}} = 1.2$ V stays stable, as the capacitor is not discharged. Nevertheless, no more ions can be adsorbed, hence the electrical conductivity κ at the outlet is equal to the one at the inlet and $I_{\mathrm{mod}} = 0$.

Setting 3: Now $U_{\mathrm{max}} = 2$ V and $I_{\mathrm{max}} = 48$ A are set and the voltage switch turned to the negative position. Now the capacitor is discharged and subsequently charged with reversed voltage and defined as *negatively charged*. At the time of measurement, $U_{\mathrm{cell}} = U_{\mathrm{max}} = 2$ V was reached already and I_{mod} started decreasing to $I_{\mathrm{mod}} = 41$ A. This is assumed to occur due to no counter ions can accumulate in the electrodes in this phase. From this point on the discharge phase is not a constant current discharge (CCD), but strictly speaking a constant voltage discharge (CVD). In normal applied operation, where quick discharges are desirable, this occurs very often and is nevertheless subsequently called constant current discharge, as long the first part of the phase starts as CCD. Furthermore, $\kappa_{\mathrm{in}} < \kappa_{\mathrm{out}}$ can be observed.

Setting 4: If from this point U_{max} is set to 0 and the voltage switch remains on the negative position, an electric current can still be measured as well as a voltage due to ions are still flowing out of the electrodes and force electron movement. The conductivity κ_{out} is still higher than at the inlet, but smaller than in the previous configuration. Theoretically, this electrical power can be used each cycle for energy recovery.

Setting 5: After charging, the power supply is turned off and the voltage switch, in opposite to configuration 4, to the discharge position and no electric current is measured. This occurs due to the the power supply limits it to $I_{\mathrm{max}} = 0$ A. Furthermore, no ions are expelled from the electrodes since $\kappa_{\mathrm{in}} = \kappa_{\mathrm{out}}$ is measured.

Setting 6: In a last step, the shunt switch is closed and neither voltage nor amperage can be measued as expected. Furthermore, the electrical conductivity does not

change between in an outlet. This mode is used for flushing the system and pre charging the electrodes with a new initial concentration of salt ions or for cleaning procedures, since no concentration polarisation can occur.

For a detailed look at the voltage and amperage response of the system under different settings of $U_{\max}$ and $I_{\max}$ as well as switch positions, the voltage and electric current, U_{mod} and I_{mod}, have been recorded over time, with the logging frequency $\frac{1}{1\mathrm{s}} < f < \frac{1}{1.5\mathrm{s}}$ and highlighted in fig. 7.2. Furthermore, these tests shall reveal energy recovery

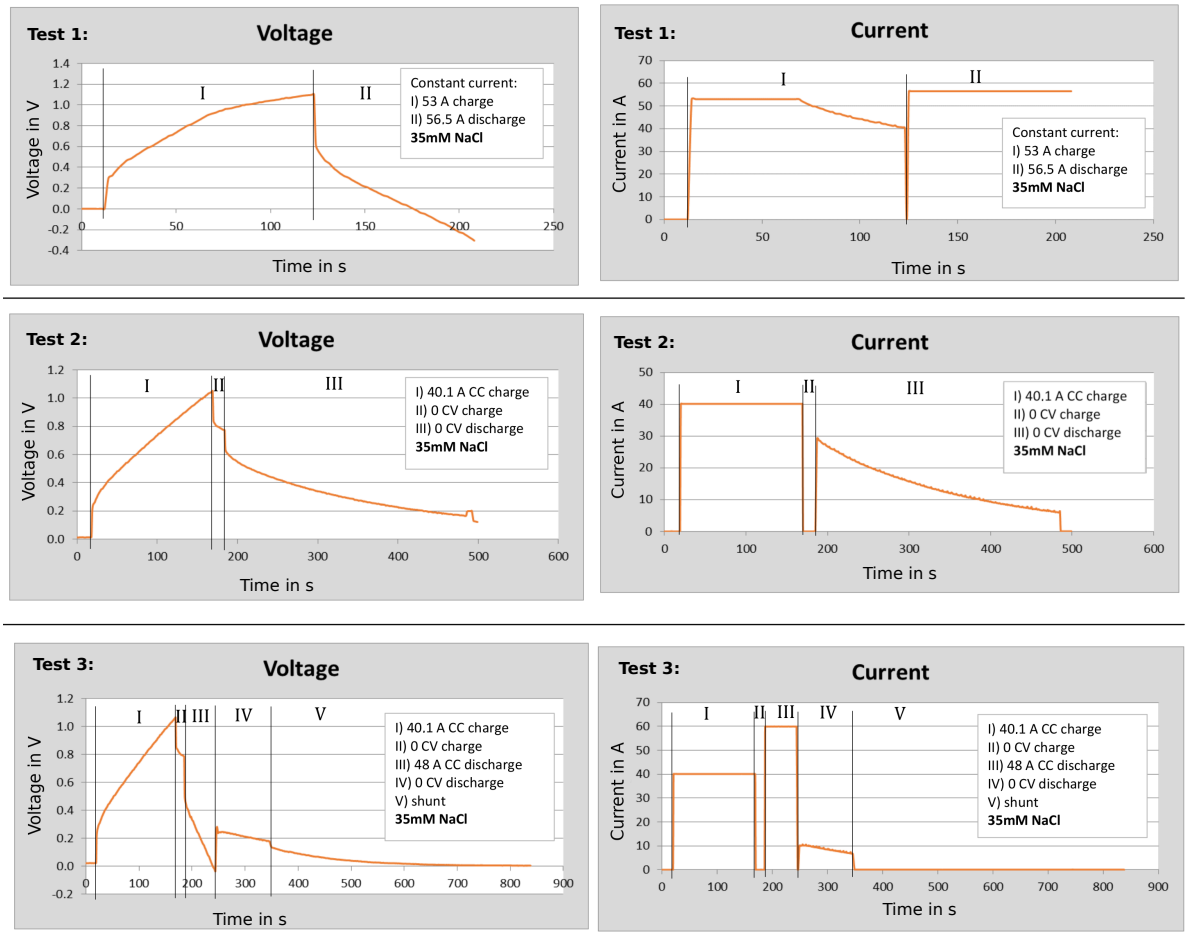

Figure 7.2. Voltage and amperage over time of the MCDI module while different scenarios are applied. Inlet concentration $c = 35$ mM NaCl.

potentials. During three different test runs, the electric response can be described as follows:

Test 1: A constant current charge discharge (CCCD) operation can be observed. Phase I shows the charging half cycle (with setting 1 of fig. 7.1) with $I_{\mathrm{CCC}} = 53$ A and phase II the discharge (setting 3) with $I_{\mathrm{CCD}} = 56.5$ A. During the charge time,

U_{mod} increases as expected until $U_{\text{cell}} = U_{\text{max}}$ after around 70 seconds. Then U_{mod} is less increasing, but still due to the ongoing adsorption of ions. At this point of time I_{mod} starts to decrease. This means, on the counter part of the electrode, that the ions are adsorbed slower. After $t = 120$ s, the discharge cycle is initiated and the voltage is dropping accordingly. The electric current is increasing to I_{CCD} and stays constant.

Test 2: The phase I is again the charging phase (setting 1) but with $I_{\text{CCC}} = 40.1$ A, which causes a more slight increase of U, thus U_{max} is not reached and I remains constant. In the next phase, U_{max} is set to 0 (setting 2) and it can be observed that U_{mod} decreases slowly and I drops to 0. This means that also no ions are adsorbed anymore. In phase III, U_{max} is kept on 0 V but the voltage switch is turned to negative (setting 4), meaning discharge position. Only now, ions are released in the 0VD cycle, although no additional voltage was applied and U_{mod} is decreasing. Furthermore, the migrating ions force an electrical current which is decreasing together with the speed of desorption. Here, a potential of energy recovery can be observed.

Test 3: The first two phase do not differ from test 2. In phase III, the capacitor is discharged completely (setting 3) until $U_{\text{mod}} = 0$ V, with a CCD operation but not further charged with reversed voltage as usual in normal operation. In this phase, the electric current remains constant over time. When the voltage at the capacitor is 0, negative charging or also called discharging voltage is set to 0 at the power supply during phase IV (setting 4) and it can be seen that still releasing ions induce electrical power. In phase V, the shunt switch is additionally closed (setting 6). Now, no electrical current can be measured and the capacitor is discharging slowly to 0.

With these experiments, the electric behaviour and the ion transport dynamic of the MCDI module was analysed. It can be seen that the MCDI responds like a capacitor, which can release energy during the discharge phase due to additional ion movement, that could be used for energy recovery purposes. Furthermore, the conventions of the DK system are determined: The negative voltage is the discharging voltage, which can reach negative values and the electric current always remains in the positive range. The assumed schematic of the electric circuit seen in fig. 6.3 could be confirmed.

To analyse the different effluent concentration over time, constant voltage (CV) and constant current (CC) experiments were carried out and compared, which results can be seen in the following sections.

With CV desalination, ions are adsorbed at a maximum rate until the EDLs are fully shaped and the electrodes saturated. Thus these experiments are suitable to determine the salt adsorption capacity of an MCDI module.
With CC desalination, ions are adsorbed at an even rate and a constant effluent concentration is achieved. Hereby, the SAC values can be compared with different applied electrical currents.

7.2 Constant voltage single pass experiments

To determine the basic performance of an MCDI module, especially the salt adsorption capacity (SAC) and material properties of the electrodes as well as for evaluation of the results of the theoretical models, single pass experiments with constant voltage charge (CVC) have been operated. This operation forces the system to adsorb salts as quickly as possible until the capacitor is charged with a given maximum voltage. Beforehand, all ions have been completely expelled from the electrodes, by applying a negative voltage until $\kappa_{\text{out}} = \kappa_{\text{in}}$. The tests have been operated with a C5 module from *Voltea* (see sec. 6.1.2).
In several experiments, different charging voltages U_{cell} (set as maximum at the power supply, see fig. 6.3) between 0.0 and 1.5 V, were applied. Due to the presence of an external resistance, the high total area of the electrode and the need of an overpotential, no water electrolysis is yet expected (see tab. 2.1 and description). The concentration at the module's outlet over time, develops throughout the different experiments as indicated in fig. 7.3 (for a better overview, the results of ten measurements). By increasing the cell voltage, more ions could be adsorbed and appropriately, the outlet concentration was decreased stronger and for a longer time. It needs to be highlighted, that ions are also adsorbed with $U_{\text{cell}} = 0$ V, due to diffusion- rather to electromigration- effects. In the first seconds concentration and electric potential differences are the highest and thus the most ions per time are adsorbed. After the porous electrodes are filled up, both driving forces weaken and less ions are adsorbed, hence the outlet concentration rises. In a CVC operation, these are typical characteristics, where κ_{out} reaches a short minimum and no flat progression is observed, which shows similar behaviour as the course of the electric current function over time, charging a capacitor with a constant voltage (no constant current). As an example, the voltage and amperage characteristics of a CVC operation with $U_{\text{cell}} = 1$ V is shown in fig. 7.4. After reversing the voltage, U_{mod} becomes positive after $t = 0$. U_{cell} remains almost constant and I_{cell} decreases to

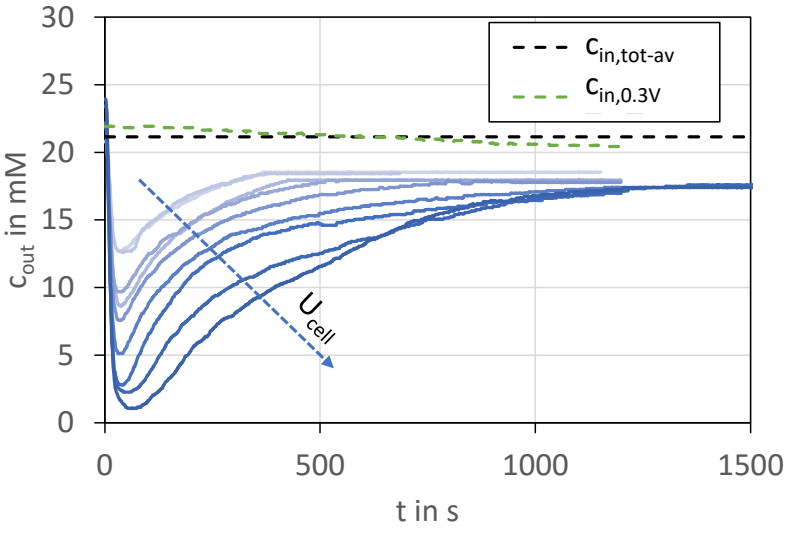

Figure 7.3. Concentration c_{out} over time for the applied voltages U_{cell} = 0.0, 0.1, 0.2, 0.3, 0.5, 0.8, 1.0, 1.2, and 1.5 V

zero as expected for charging a capacitor.

The averaged volume flow through the module was kept constantly on $\dot{V} = 1.0\ \text{L}\,\text{min}^{-1}$. The inlet concentration was in average $\bar{c}_{\text{in}} = 21.14$ mM (= $c_{\text{in,tot-av}}$ in the diagram), indicated with the dashed horizontal black line in the figure. This is in the range of subsequent operated application experiments. Hence, the electrodes are fed with 21.14 mmol NaCl per minute.

For all U_{cell}, the starting outlet concentration at $t = 0$ is higher than $\bar{c}_{\text{in}}$, approaches the line from below and remains steady on a lower level. This has following reasons:

Firstly, for the CV tests, a 50 L tank has been used for the feed water and to collect the effluent of the MCDI (see fig. 6.1, with opened hand valve (symbolic) between the tanks). This volume is not enough to buffer the difference of concentration between in- and outlet, meaning that c_{out} decreases c_{in} during the charge phase. As an example, $c_{\text{in,0.3}}$ is indicated in the figure.

Furthermore, c_{out} does not reach the inlet concentration, due to measuring errors occurring at the conductivity sensor at the outlet, when no big changes are measured in the range of $\kappa_{\text{out}} = 2.1$ to $2.2\ \text{mS}\,\text{cm}^{-1}$, which is an equivalent to $c_{\text{out}} \approx 17.9$ mM. This results in a wrong sensor data output, showing constant conductivity values. This effect was compensated by observing the change of c_{in} over time. If it was smaller than 0.5% over 20 s, the charge phase was considered to be ended. Subsequently, c_{out} was extrapolated exponentially at same progression before reaching this concentration.

With eq. 6.2 and eq. 6.3 the SAC was calculated, which is shown in fig. 7.5 together with

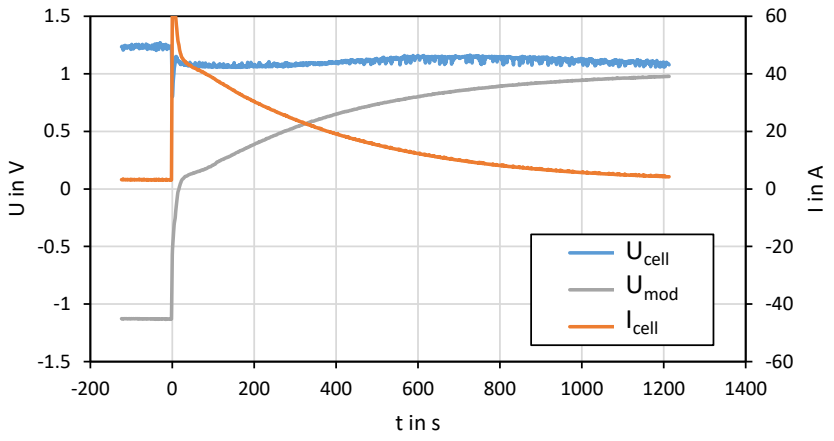

Figure 7.4. Characteristics of voltages and amperage for CVC operation (starting at t=0) with $U_{\text{cell}} = 1$ V

U_{cell}, for all measurements carried out. Hereby, the mass of the electrodes was determined with an assumed value for the density of the active carbon of $\rho_{\text{AC}} = 0.55\ \text{g}\,\text{mL}^{-1}$ (see sec. 6.1.2) to $m_{\text{elec,C5}} = 774.4$ g. To completely compensate the effect that c_{in} is changing over time, the relation

$$\bar{c}_{\text{in}}\, t_{\text{tot}} = \sum_{t=n}(c_{in,n+1} - c_{in,n}) \cdot \sum_{t=n}(t_{n+1} - t_n) \tag{7.1}$$

was used. During the experiments, the inlet concentration was $c_{\text{in}} = 21.20$ mM ± 0.46 (SD). The TSA is rising the higher the applied voltage and thus SAC, since $\Gamma_{\text{salt}} = \frac{\Delta m_s}{m_{\text{elec}}}$. This is explained with the increasing size of the electric double layer (see sec. 2.1) and with it the storage potential. With $U_{\text{cell}} = 0$, more than 2 g of NaCl are adsorbed through diffusion only and thus SAC values in between $\Gamma_{\text{salt,0V}} = 2.60$ and $\Gamma_{\text{salt,0V}} = 3.63\ \text{mg}\,\text{g}^{-1}$ were measured. The further progression of SAC is exponential. The higher the voltage, the more the effect of electromigration prevails and a maximum SAC at U_{cell}= 1.5 V of $\Gamma_{\text{salt}} = 14.71\ \text{mg}\,\text{g}^{-1}$ is resulting.

For the CV single-pass tests can be concluded that

- CV tests are suitable to determine the SAC values for different applied voltages of an MCDI module
- the higher U_{cell}, the bigger the EDLs shaped in the porous electrodes and thus the higher the SAC

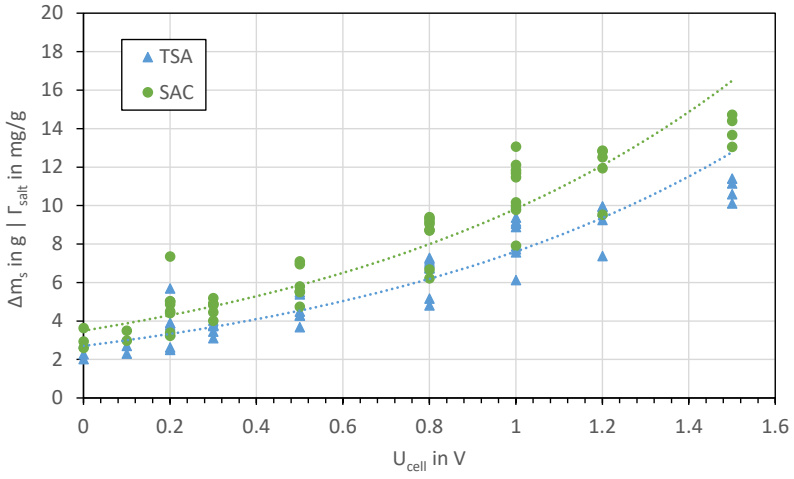

Figure 7.5. Experimentally determined SAC (Γ_{salt}) and TSA (Δm_s) values versus U_{cell} of a C-5 module (*Voltea*)

- for $U_{\text{cell}} = 0$ V, salt is adsorbed without electromigration and needs to be considered in theoretical models
- with SAC results, the mD models can be validated and material parameters set (see sec. 8.1).

7.3 Constant current single pass experiments

The usual operation of MCDI modules is in CCCD mode that a constant effluent salt concentration can be ensured. To be able to determine desalination behaviour over time and to evaluate the results of the models, single pass experiments of constant current desalination were carried out, to observe the salt adsorption performance until the electrodes are fully saturated.

As in the previous section, the electrodes are completely discharged beforehand until no ions are assumed to be inside. The tests have been operated with a C5 module from *Voltea* (see sec. 6.1.2).

Different I_{cell} were applied from 10 to 50 A and the characteristics of σ_{out} measurements observed, which is shown in fig. 7.6. It can be seen that the higher I_{cell}, the higher the initial removal of salt ions, however the earlier c_{out} is increasing. For all tests a maximum of $U_{\text{cell}} = 1.5$ V was allowed. Hence, for all tests the same amount of ion adsorption is expected. Especially for the test with low electric current as $I_{\text{cell}} = 10$ A the constant

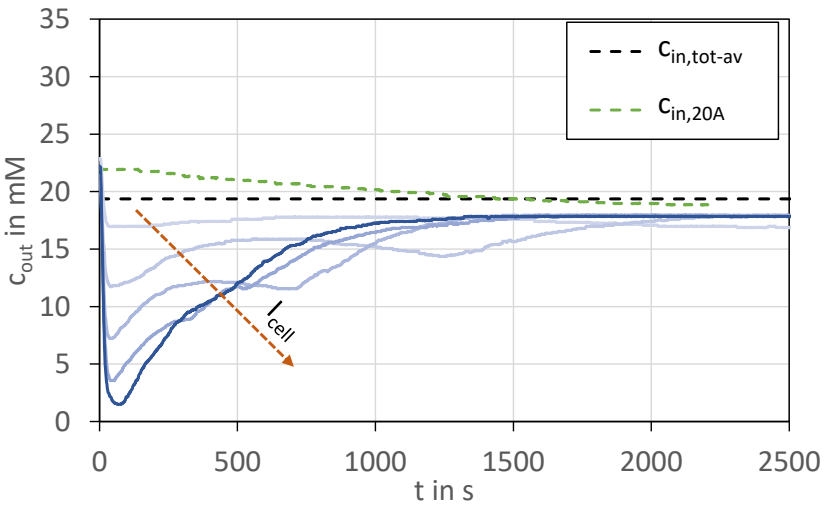

Figure 7.6. Concentration c_{out} over time for the applied electric current I_{cell} = 10, 20, 30, 40 and 50 A and $U_{\text{cell}} = 1.5$ V.

concentration at the output was observed. However, all tests show an initial minimum before that and the bigger I_{cell}, the bigger the negative peak. This is explained by the equilibrium state between adsorbing ions and feeding new ions through the water volume, which is not yet being reached. The higher I_{cell}, the lower is the subsequent stable outlet concentration.

The second blue line from above indicates the progression of c_{out} with $I_{\text{cell}} = 20$ A. It is recognized that the outlet concentration is decreasing and is not flattening after the minimum. This is due to the inlet concentration is decreasing at the same speed, since the same effluent tank is used as for the feed (see sec. 7.2). However Δc between in- and outlet is remaining constant. The same is valid for the test with applied currents of = 30 A. For $I_{\text{cell}} > 30$ A, the maximum voltage is reached before the constant outlet concentration can be established. From this point I_{cell} is decreasing as in a CVC operation (see fig. 7.7). Before that, the electric current is constant and thus forces a constant ion adsorption speed to the system. In this period, U_{cell} increases until U_{max} is reached. U_{mod} is constantly lower than the cell voltage, due to external resistances of the system (cables, current collector, etc.).

During the CCC single pass experiments, the SAC can be calculated as well as explained in sec. 7.2, which results are highlighted in fig. 7.8. The values are not expected to differ from fig. 7.5 for $U_{\text{cell}} = 1.5$ V. However a small variance between the different applied currents is visible. The best SAC value of $\Gamma_{\text{salt}} = 16.21\ \text{mg}\,\text{g}^{-1}$ is observed with the lowest $I_{\text{cell}} = 10$ A and thus a higher efficiency can be expected, with lower electrical currents in

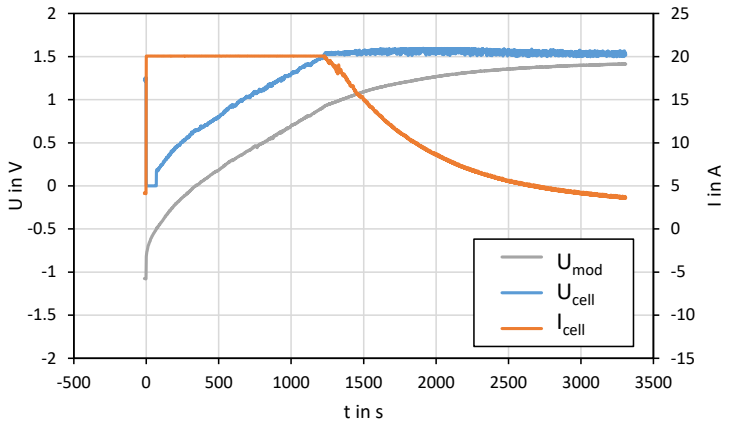

Figure 7.7. Characteristics of voltages and amperage for CCC operation (starting at t=0) with $I_{cell} = 20$ A and maximum U_{cell}= 1.5 V.

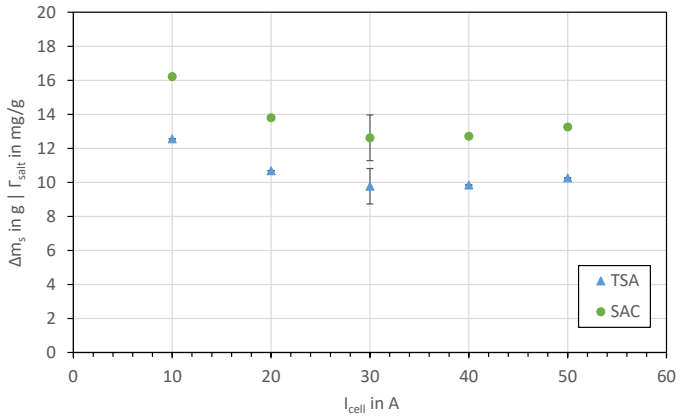

Figure 7.8. SAC and TSA values versus I_{cell} of a C-5 module, with U_{cell} =1.5 V

the later application tests. This can be explained with a possible higher charge efficiency for lower I_{cell}, due to ion swapping effects (see sec. 2.4.2) happen slowly in the beginning of the desalination phase (Suss et al., 2015) and thus more co-ions can be expelled from the electrodes and more ions can be adsorbed overall to balance the electrical charge (sec. 2.4.2). The SAC with an I_{cell} 50 A, $\Gamma_{salt} = 13.25$ mg g^{-1} is within the range of the CV tests in the previous section, where electric currents are always maxed out.

For the CC-single pass tests can be concluded that

- for CC desalination, constant effluent concentrations can be observed, which are needed for applied MCDI operation

- the lower I_{cell}, the lower the salt removal and the longer the desalination. However higher SAC values are measured, due to assumed higher charge efficiencies
- the maximum SAC of $\Gamma_{\mathrm{salt}} = 16.21\ \mathrm{mg\,g^{-1}}$ at $U_{\mathrm{cell}} = 1.5$ V was measured for $I_{\mathrm{cell}} = 10$ A.

7.4 Application tests for water treatment

As stated before, MCDI in water treatment applications is typically operated in CCCD mode, while the desalination step is ended when the target of the water quality is exceeded and the regeneration step when most of the ions are flushed out of the system (see sec. 6.1). Hence, the most experimental data collected is from application tests of the commercially available modules (see sec. 6.1.2), for which the strived models have to be valid.

Firstly, the attention was turned to adjust the operational parameters to optimize the MCDI desalination, so it can compete with the conventional RO method, especially concerning specific energy demand (SEC). Furthermore, realistic data for evaluating the simulation results was generated.

To analyse the characteristics of the CCCD operation, the results of voltage, amperage and conductivity measurements of a typical operation with the parameters listed in tab. 7.1 are shown in fig. 7.9. These MCDI settings are the results of manually opti-

Table 7.1. Operational parameters used to desalinate water with $c_{\mathrm{in}} = 1.65\ \mathrm{g\,L^{-1}}$ for drinking water purpose in CCCD mode

Phase	Time in s	U_{cell} in V	I_{cell} in A	$\dot{V}$ in L min^{-1}
C	130	1.3	54.1	0.6
PP	60	1.3	21	0.25
P	440	1.3	12.3	0.4

mizing the cycle by adjusting the parameters. The focus of setting the phase times and electric current is the charge balance between concentrate (C) and pre-purify (PP) plus purify (P) phases, which possess opposite signs. Hereby, the negative charge (in the concentrate/discharge phase) $Q_{\mathrm{D}} = 7033$ C is adjusted to be approximated 5% higher than the positive charge $Q_{\mathrm{C}} = 6672$ C, to ensure the capacitor is discharged completely and the full adsorption potential is given in every charging cycle. To guarantee high

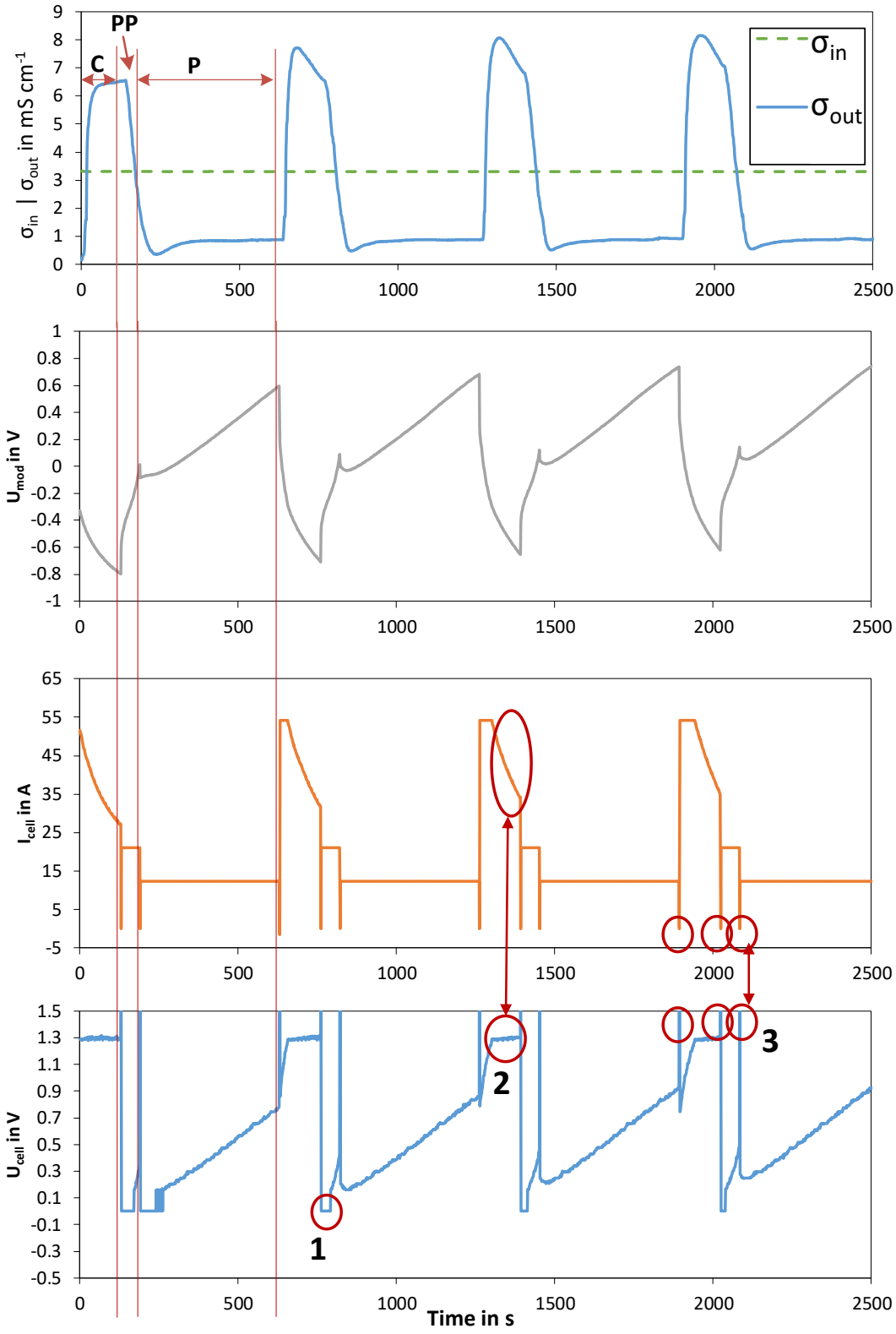

Figure 7.9. Characteristics of MCDI desalination in CCCD mode

SAC values and not to risk water electrolysis, $U_{\text{cell}} = 1.3$ V for all phases was chosen. I_{cell} was adjusted together with $\dot{V}$ to balance the feed/adsorption ratio of the ions. The phase times were fit together with the amperage to balance the charge ratio. Furthermore is the C and PP phase kept as short as possible to raise the water recovery. With $\eta_{\text{vol}} = 65.2\%$ and these parameter settings, 400 L of pure water was produced per day. Furthermore, $\dot{V} \cdot t$ needs to be higher than the volume of water between the electrodes and partly inside the MCDI module, since all concentrated water has to be flushed out in the C-cycle.

In fig. 7.9 the characteristics of the electric conductivity before and after the MCDI module, U_{cell}, U_{mod} and I_{cell} are highlighted. In the diagrams, the C, PP and P phases are indicated in one cycle, which repeat periodically.
It can be observed that after the pure phase was initiated, σ_{out} is overshooting the plateau shortly (as shown in sec. 7.3) and then progresses into the steady state. In real MCDI application, it is mostly necessary that the purify phase ends before σ_{out} starts to increase again. Due to relatively small I_{cell} and $\dot{V}$ were set, the conductivity measurement at the outlet remains constant below $\sigma_{\text{out}} = 0.9$ mS cm^{-1} for the rest of the phase and drinking water is produced (see sec. 6.2.3). Subsequently, the concentrate phase flushes out all ions which were lead to the spacer through the reversed voltage. To do so as quickly as possible, high I_{cell} is used while assuring $Q_{\text{D}} = 1.05 \cdot Q_{\text{C}}$.
The pre-purify phase guarantees that the desired concentration at the outlet is reached before the purify phase sets the position of the valve to the product channel (see fig. 6.1). At the end of PP, U_{mod} reaches approximated zero. This voltage increases for positive and decreases for negative applied U_{cell} (see fig.6.3). Furthermore, its absolute value is always smaller than U_{cell}, due to external resistances.
It can be observed that I_{cell} remains constant until U_{cell} reaches its maximum value (point 2 in the figure), which was expected of a CCCD operation. It was observed that this happens only in the concentrate phase, due to electrical currents are high, speeding up the ionic exchange and no ions are accumulated in the discharge phase. This leads to a smaller ionic counter charge in the pores of the electrodes (see sec. 2.4.2) and higher electric potentials are reached quicker. I_{cell} is set to be higher in the PP than in the P phase and $\dot{V}$ vice versa (tab. 7.1), to increase the water recovery η_{vol}.
When the applied voltage is switched from negative to positive, the diagram shows $U_{\text{cell}} = 0$ for $t = 30$ s as indicated by point 1 in the figure, which highlights the energy recovery potential of MCDI operation.
In point 3, amperage and voltage peaks are observed. They occur at the switching

times in between the phases. This is explained by electronic circuit effects in between the switching relays and the power supply output. Hereby, short shunting times in between the phases flats the peaks and protects the power supply from over voltage at the outlet.

To optimize the MCDI process, a series of experiments were carried out with a C-3 module (see sec. 6.1.2) and model water with an NaCl concentration of $c_{\mathrm{in}} = 1\,\mathrm{g\,L^{-1}} = 17\,\mathrm{mM}$, to produce drinking water. The operational parameters have been adjusted to increase the recovery rate and at the same time keep the SEC as low as possible. The experiments with the most promising results are listed in tab. 7.2 and the outcome of water recovery (eq. 2.22), salt removal and SEC further in tab. 7.3. It needs to be highlighted

Table 7.2. Operational parameters of most promising optimizing experiments for MCDI desalination

	$\dot{V}$ in L min^{-1}			Time in s			I_{cell} in A		
Pos.	**C**	**PP**	**P**	**C**	**PP**	**P**	**C**	**PP**	**P**
1	1	1	1	115	20	110	21.5	18	18
2	1.5	1.5	1.5	115	20	110	32.7	27.5	27.5
3	1	1	1	115	20	220	39.5	18	18
4	**1**	**1**	**1**	**115**	**20**	**330**	**57.6**	**18**	**18**
5	0.25	1	1	115	40	330	57.6	18	18
6	0.25	0.25	1	115	40	360	57.6	18	18
7	0.25	1	1	115	40	360	57.6	18	18
8	0.25	1	1	125	30	110	58.7	49.9	49.9
9	0.25	0.5	1	135	40	110	58.3	49.9	49.9
10	0.25	1	1	115	40	310	57.6	18	18
11	0.25	1	1	115	40	310	59.2	18.5	18.5

that to fulfil drinking water regulations, 55% of salt needs to be removed of water with the quality $c = 1\mathrm{g\,L^{-1}}$. Since the inlet concentration varied over time it was enough for experiment pos. 4 in the table, to remove 54% of the salt to achieve the desired quality ($c_{\mathrm{in},4} = 0.96\ \mathrm{g\,L^{-1}}$, $c_{\mathrm{dil},4} = 0.44\ \mathrm{g\,L^{-1}}$).

The results of the optimization tests are visualised in a diagram for the recovery versus the removal together with the SEC in fig. 7.10. Highlighted is the removal mark, below which no drinking water quality is assured. The figure shows that the higher the removal the higher the SEC. A small increase is observed with rising water recovery as well. To evaluate the optimum experiment, the test with the highest recovery value and lowest SEC, which removes enough NaCl was chosen and indicated with the red dot in the diagram (furthermore, pos. 4 in tables tab. 7.2 and tab. 7.3).

Additionally, optimizing test series have been carried out with $c_{\mathrm{in}} = 2\ \mathrm{g\,L^{-1}}$ and subse-

Table 7.3. Recovery, removal and SEC of optimizing experiments for MCDI desalination

Pos.	Removal in %	Recovery in %	SEC in kWh m^{-3}
1	58	45	0.45
2	58	44	0.63
3	55	61	0.53
4	54	71	0.61
5	52	82	0.65
6	49	90	0.64
7	53	84	0.60
8	75	64	2.90
9	79	66	3.22
10	48	82	0.59
11	46	81	0.64

quently η_{vol}, η_{rem} and the SEC have been evaluated in the same way. The results are shown in fig. 7.11. The threshold for the minimum salt removal lays at $\eta_{\text{rem,min}} = 77.5$ %. The optimum test achieved $\eta_{\text{rem}}= 78\%$, $\eta_{\text{vol}}= 44\%$ and an SEC= 1.58 kWh m^{-3}, with the operational parameters listed in tab. 7.4.

Table 7.4. Optimum operational parameters to desalinate water with $c_{\text{in}}= 2$ g L^{-1} for drinking water purpose

Phase	Time in s	I_{cell} in A	$\dot{V}$ in L min^{-1}
C	130	50.0	1.0
PP	20	13.3	0.25
P	440	13.3	0.25

It was observed that in both cases, the tests with optimum results were using relatively low $I_{\text{cell}}= 18$ A and 13.3 A, in the charging phase. This fits with studies in the CCC single pass experiments (sec. 7.3), where it was found that for low I_{cell}, more stable c_{out} and higher SAC values are resulting. To produce drinking water the water volume flow needed to be set very low with 0.25 L min^{-1} in the 2 g L^{-1}-case. This negatively affects the recovery rate and thus the SEC in kWh per produced m^3 of diluate, due to the total volume of product water is being reduced.
The SEC = 0.61 kWh m^{-3} for producing 1.02 m^3 of drinking water per day in the 1 g L^{-1}-case is very low and can compete with conventional desalination technologies as reverse osmosis (Zhao et al., 2013a).

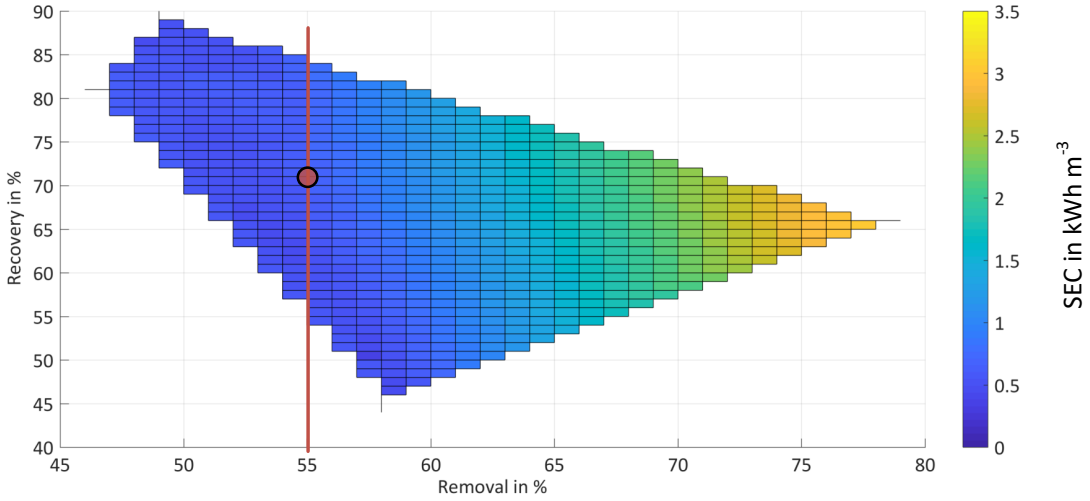

Figure 7.10. Results for water recovery, salt removal and SEC of the optimization tests, desalinating model water with 1 gL^{-1}NaCl to produce drinking water

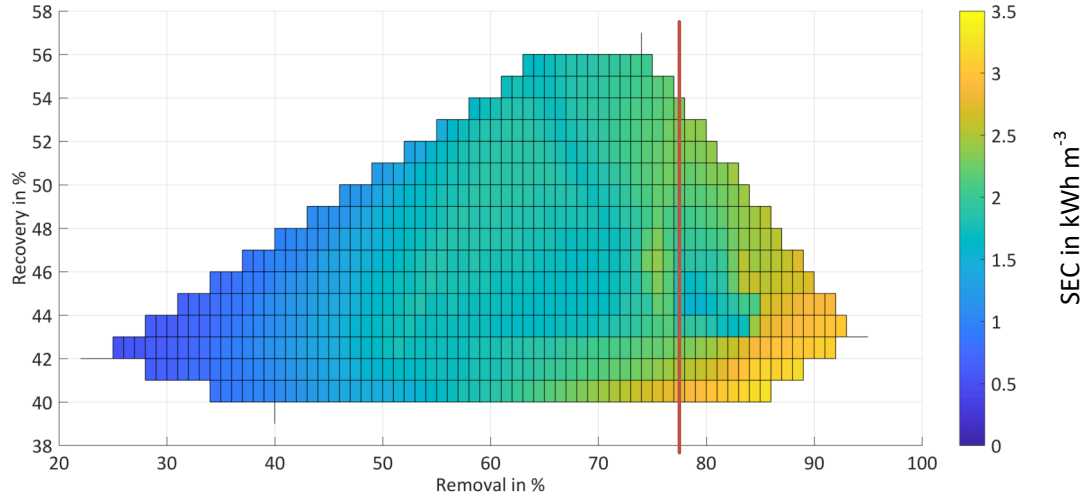

Figure 7.11. Results for water recovery, salt removal and SEC of the optimization tests, desalinating model water with 2 gL^{-1}NaCl to produce drinking water

8 Results and discussion of modelling

In this chapter, the results of the modelling work and subsequent evaluation is presented, subdivided into the different approaches explained in sec. 5:

1. The results of the adaption of the analytical models are presented and simplification possibilities, advantages and disadvantages are listed. Furthermore, with the analytical model, material properties can be determined (sim. I).
2. To evaluate the meshing and calculation times, mesh studies as pre-simulation are shown.
3. The FEM modelling approach for ion transport is presented, since it shows a holistic view of the ion movement and uses its physical basic equations (sim. II-III).
4. CFD modelling for the water flow through an MCDI module has been carried out and results are presented subsequently (sim. IV).
5. To improve accuracy of the simulation of applied MCDI operation, models have been combined and the results are highlighted (sim. V-VI).

8.1 Analytical modelling of adsorption

8.1.1 Modelling results

The analytical models in this thesis are based on the modified Donnan models (see sec. 4.3), which have different validity for different input parameters (see tab. 4.2). For this reason, various modifications of the model were tested with parameters of commercial available MCDI modules.
The analytical modelling of the adsorption was carried out as explained in sec. 5.2.3, with the implementation of eq. 5.9 - eq. 5.12 in the spreadsheet program. The different modifications of the model were taken into account by varying the additional attractive term μ_{att}.

After calculating c_{mi}, the SAC was determined with eq. 5.13 (with $\rho_{\mathrm{AC}} = 0.55\ \mathrm{g\,mL^{-1}}$ adjusted from literature Dykstra et al. (2016)) and is presented for different models in fig. 8.1. For the $\mathrm{mD_0}$ and $\mathrm{mD_{1.9}}$ data, the mD model was used with a constant

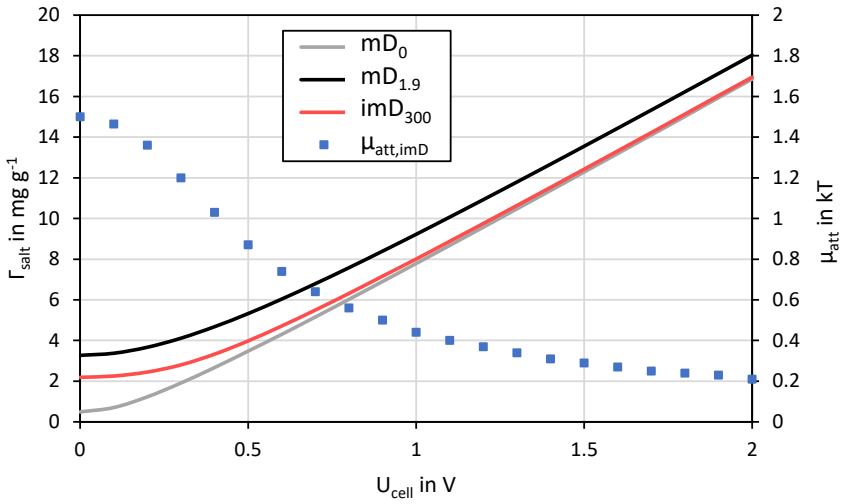

Figure 8.1. SAC versus U_{cell} according to different mD models and calculated μ_{att} for the imD model; $c_{\mathrm{Sp}} = 20$ mM.

$\mu_{\mathrm{att}} = 0$ kT and 1.9 kT respectively. For the improved modified Donnan model (imD), the additional attractive term was caclulated manually (see eq. 4.10), iteratively together with above mentioned equations, by choosing $E_{\mathrm{att}} = 300$ kT from literature (Biesheuvel et al., 2014). Hereby, the maximum amount of iteration steps was $\leq$ 5. The subscript behind imD indicates the used E_{att}.

The data series with the names of the mD model, indicate Γ_{salt} in the diagram. It is observed that the SAC is increasing over U_{cell}, firstly exponential and subsequent almost linear. The biggest difference in between the models can be seen at low $U_{\mathrm{cell}} < 0.4$ V. This is the range, where the additional attraction μ_{att} term has the most influence on ion adsorption. The higher μ_{att}, the higher Γ_{salt}. For $\mu_{\mathrm{att}} = 0$, a small adsorption is visible ($\Gamma_{\mathrm{salt}} = 0.49\ \mathrm{mg\,g^{-1}}$) when no voltage is applied, which is mathematically described by eq. 5.9. If $\Delta\phi_{\mathrm{D}} = 0$ (when $U_{\mathrm{cell}} = 0$, see eq. 5.12) and μ_{att} as well, $c_{\mathrm{mi,NaCl}} = 2 \cdot c_{\mathrm{Sp}}$ (molar concentration, thus $= c_{\mathrm{mi,Na}} + c_{\mathrm{mi,Cl}}$). Physically, it is explained that the micro pores attract such many ions that the concentration is balanced with the spacer, without a voltage applied yet.

The SAC for the $\mathrm{mD_{1.9}}$ model at zero voltage is $3.27\ \mathrm{mg\,g^{-1}}$ and for the imD model $2.19\ \mathrm{mg\,g^{-1}}$. The determined μ_{att} for the imD at $U_{\mathrm{cell}} = 0$ is 1.5 and decreases to 0.21 at $U_{\mathrm{cell}} = 2$ V. Hence the curve of the imD approaches the mD without an attraction

term at higher voltages.

To compare the difference of various inlet concentrations and thus c_{Sp}, the imD model was calculated with c_{Sp} = 10, 20 and 30 mM. The results are shown in fig. 8.2. The

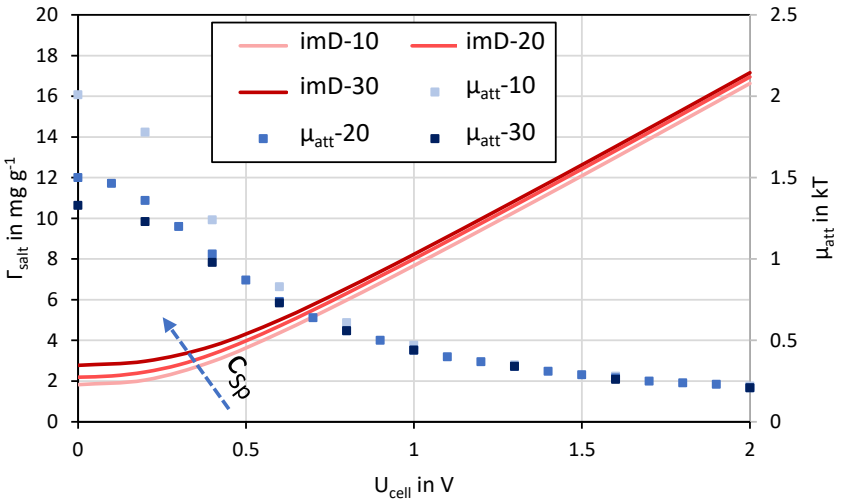

Figure 8.2. SAC versus U_{cell} according to the imD, with the concentrations c_{Sp} = 10, 20 and 30 mM

number behind the name of the data series indicates the feed concentration in mM. The main influence on the SAC outcome is again observed at $U_{cell} < 0.4$ V. At $U_{cell} = 0$ for rising spacer concentrations, μ_{att} increases and the SAC decreases, although the higher attraction term results in higher ion adsorption. However, the influence of the spacer concentration is greater on c_{mi} and thus on Γ_{salt}.

For $U_{cell} > 1$ V, all models seem to have a linear progression. After varying μ_{att} for the mD model and c_{in} for the imD model, the micropore ion correlation energy for the imD model was changed to E_{att} = 1965 kT mol m^{-3} to fit experimental data and all types were compared in the sense of linearity for $U_{cell} > 1$ V (see fig. 8.3). For this, the theoretical SAC values for U_{cell} = 10 and 100 V were calculated, whereas in practical MCDI application these voltages are never applied to avoid water electrolysis (see sec. 2.1.5). The concentration c_{in}= 20 mM was given except for imD-10 and imD-30. On the logarithmic scale, it can be seen that all models conjoin to a linear progression after $U_{cell} \approx 2$ V. This means that for the imD models, the μ_{att} is higher for higher E_{att}, but decreases close to zero at U_{cell} = 10 V, which is μ_{att} = 0.26 kT for imd$_{1965}$ and μ_{att} = 0.04 kT for the other imD models.
For the md models, this means that although the attractive chemical potential remains

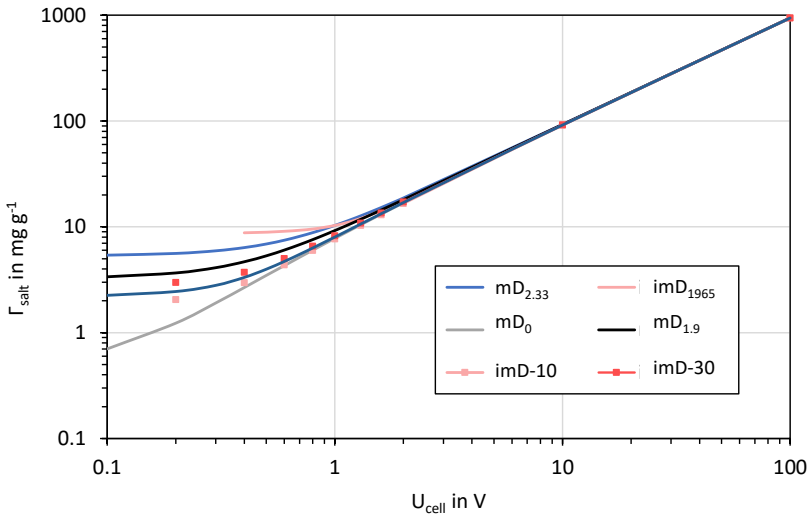

Figure 8.3. Linear progression of the mD models for high U_{cell}

high for increasing U_{cell}, the voltage and thus growing $\Delta\phi_{\text{D}}$ has a higher influence on the SAC than the constant μ_{att}, since both terms are variables of first order of the equation for c_{mi} (see eq. 5.9).

The discussed analytical mD models in this section are easy to calculate with low computational effort. They can calculate the concentration in the micro pores of electrodes in an electric field and thus the salt adsorption capacity. Hereby, different U_{cell} were applied and inlet concentrations set. It was found that for applying low voltages, the additional attractive term has a high influence on the results. However for $U_{\text{cell}} > 1$ V, the imD model does not differ significantly from the mD model without attractive term included. To minimize the calculation effort (especially with spreadsheet programs), the mD model with a constant μ_{att} can be considered. Hence, the main performance parameter SAC for MCDI operation can be calculated.
These models do not have a statement on the time dependant characteristics of the MCDI operation as effluent concentration and electrical current and a continous periodical simulation is not feasible.

8.1.2 Evaluation with experimental data

Another disadvantage of the mD model is the need of experimental data to adjust the parameters needed for calculation as the mass of the electrodes m_{elec} (or dimensions and density), the porosity or volume ratio of the micro pores, the STERN capacity C_{St} (or

$C_{St,0}$ and α, see eq. 4.7) as well as E_{att} or μ_{att} (see eq. 4.10).
These variables were taken from aforementioned literature (see tab. 4.1) and adjusted after comparing the results with own experimental data. The tuned parameters were mass of electrodes and porosity of micro pores to $m_{1elec} = 3.1$ g and $p_{mi} = 0.22$ (see sec. 6.1.2). This results in a total mass of all electrodes in a C-5 module to $m_{elec} = 774$ g. Fig. 8.4 shows the experimental data of sec. 7.2, together with several adjusted mD models, which are

- **mD$_0$**, the mD model with no additional attraction term
- **mD$_{1.9}$**, the mD model with $\mu_{att} = 1.9$ kT, which is adjusted to fit experimental data for low U_{cell}
- **mD$_{2.33}$**, the mD model with $\mu_{att} = 2.33$ kT, which is adjusted to fit the linear trendline of the experimental data, between $U_{cell} = 0.5$ and 1.5 V
- **imD$_{300}$**, the imD model with $E_{att} = 300$ kT mol m^{-3}, which is taken from aforementioned literature
- **imD$_{1965}$**, the imD model with $E_{att} = 1965$ kT mol m^{-3}, which is adjusted to fit the linear trendline of the experimental data at $U_{cell} = 1$ V and the data for $U_{cell} = 1.5$ V.

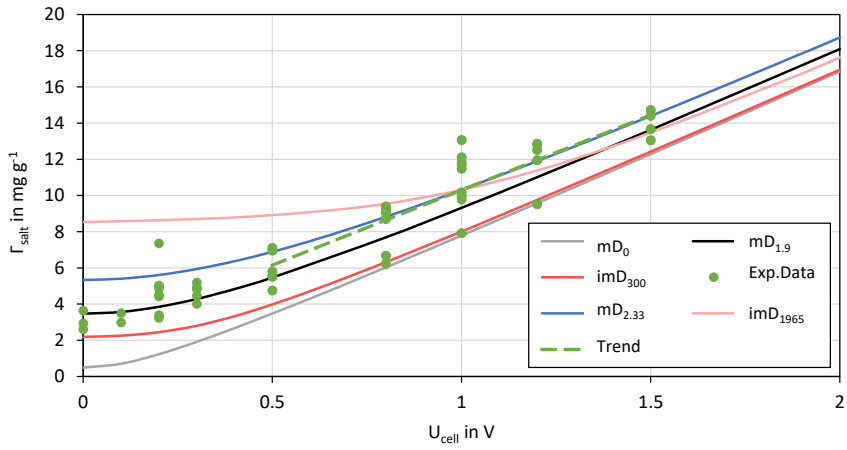

Figure 8.4. Different adjusted mD models compared with the SAC of experimental data from the CVC single pass experiments

By comparing the experimental data with the model data for different μ_{att} and E_{att}, it stands out that the tendency of the SAC value over the cell potential of both are in agreement with each other. The salt adsorption capacity below U_{cell}= 0.5 V of the

experimental data fits best to the mD model with $\mu_{att} = 1.9$. Since the various model data appears almost parallel linear to each other above U_{cell}= 0.5 V, a linear tendency line was created for $0.5 < U_{cell} < 1.5$ V and an mD and imD model was searched to fit this line in the middle at the cell voltage of 1 V. The line possess the function $f(x) = 8.2979\,x + 2.0008$ which results in a value of $\Gamma_{salt} = 10.30$ for $U_{cell} = 1$ V. The $mD_{2.33}$ and imD_{1965} fit this point of function exactly. The first of both further follows the linear trendline, whereas the latter decreases too quickly to match with the experimental data. The $mD_{2.33}$ is the closest model which fits to the averaged values of the experimental data, for $U_{cell} \geq 1$ V and for the averaged $c_{in} = 21.20$ mM, which is highlighted in tab. 8.1. Hereby indicated in blue, are the best matching values for experimental data.

Table 8.1. Values for SAC in mg g^{-1} of mD- and experimental data for different U_{cell}

U_{cell} in V	**0.0**	**0.1**	**0.2**	**0.3**	**0.5**	**0.8**	**1.0**	**1.2**	**1.5**
$mD_{1.9}$	3.47	3.57	3.85	4.28	5.47	7.69	9.32	11.01	13.63
$mD_{2.33}$	5.33	5.40	5.61	5.94	6.89	8.82	10.31	11.90	14.39
Exp.data	3.05	3.23	4.72	4.71	5.94	8.40	10.89	11.93	13.96
SD	±0.43	±0.26	±1.19	±0.38	±0.90	±1.16	±1.47	±1.25	±0.65

Evaluating the models revealed that the mD model fits better than the imD, to own experimental data of commercial MCDI modules to desalinate NaCl spiked water to produce drinking water, for higher voltages ($U_{cell} \geq 0.8$ V) where normal operation takes place. For simplification reasons, the mD model is further considered with a constant $\mu_{att} = 2.33$ kT, which is shown to be valid in this range of cell voltage. Furthermore, the parameters for the additional attraction term is in range, of which can be found in literature (e.g. Biesheuvel et al., 2014; Dykstra et al., 2016). In contrast, the micro pore ion correlation energy $E_{att} = 1965$ kT mol m^{-3} of the fit imD model, is much higher than found in aforementioned publications with $E_{att} = 300$ kT mol m^{-3}, which further speaks for using $mD_{2.33}$ instead.

A scheme as an overview of in- and outputs for the mD models is pictured in fig. 8.5. The mD models need a constant voltage single-pass experiment to validate the parameters C_{St}, V_{mi}, ρ_{AC} and Λ. For further prediction, the inputs c_{in}, U_{cell}, m_{elec}, and M_{salt} of monovalent salts can be varied to calculate the salt adsorption capacity Γ_{salt} of the MCDI module.

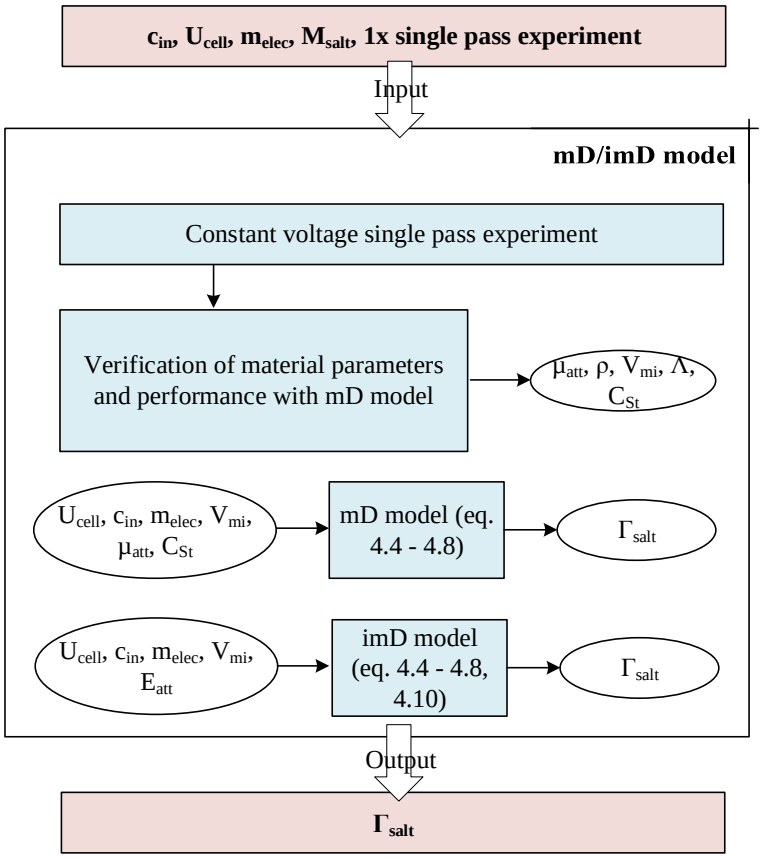

Figure 8.5. Process scheme of the mD models with in- and outputs

8.2 CFD for water flow simulation

A big difference between lab scaled MCDI cells and commercial modules for application is the dimensional scale and the linked constructive challenges of the design. The arrangement of the electrode pairs and the thicknesses of the spacer have a direct influence on the retention time of the salt water between the electrodes.

To develop a model for the latter, CFD simulations for the water flow, with a stack of 75 pairs of electrodes with different spacer thicknesses were carried out. The calculation domain is pictured in fig. 8.6. As described in sec. 5.2.2, the inlet and outlet BCs are at the top left and top right of the geometry. The inflow was set constant on $\dot{V} = 1\,\mathrm{L\,min^{-1}}$(over a squared inlet with side length of 10 mm). The spacer thickness was varied between $\delta_{\mathrm{Sp}} = 0.25$ and 4 mm. The distance between the spacer was constantly held on 5 mm, which is an assumption of the sum of IEMs, two electrodes and their current collectors plus constructive material in between.

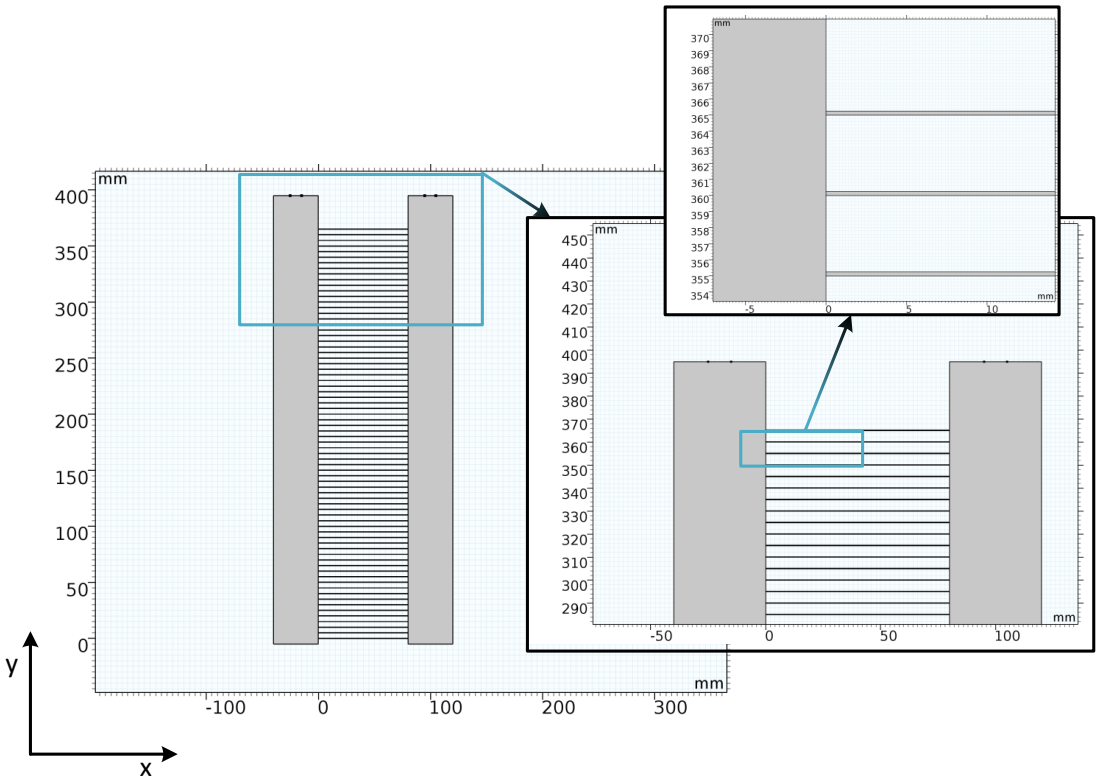

Figure 8.6. Ω of the CFD simulation. Fluid flow through an MCDI module

After stationary calculations, the distribution of the volume flow over the single spacers were analysed, to draw conclusions from it on even retention times over all spacers, to ensure stable desalination.

By observing the 2D plots of the velocity field times normalized cross section over Ω (fig. 8.7), for different δ_{Sp}, a difference in volume flow equality between the spacers can be pointed out. For both spacer thicknesses, only the first upper spacers are highlighted in the figure. Whereas the distribution of the volume flow over the spacer with $\delta_{\mathrm{Sp}} = 0.25$ mm turns out to be uniform, it seems that almost all water is flowing through the upper 20% of the module for $\delta_{\mathrm{Sp}} = 3$ mm.

Fig. 8.8 presents a closer look on the volume flow over the y-coordinate in the middle of the spacers (between in- and outlet at $x = 40$ mm). Hereby, the volume flow over a cut line between $y = 365$ mm and $y = 0$ is pictured. The reversed u-shaped lines are the flow distributions of each spacer at indicated y. Especially for higher δ_{Sp}, it can be observed that a laminar flow profile is present, however the averaged flow is distributed very non-uniform between the spacers. This indicates, that most of the water is flowing by the above electrodes and not much water reaches the bottom. For $\delta_{\mathrm{Sp}} = 4$ mm the

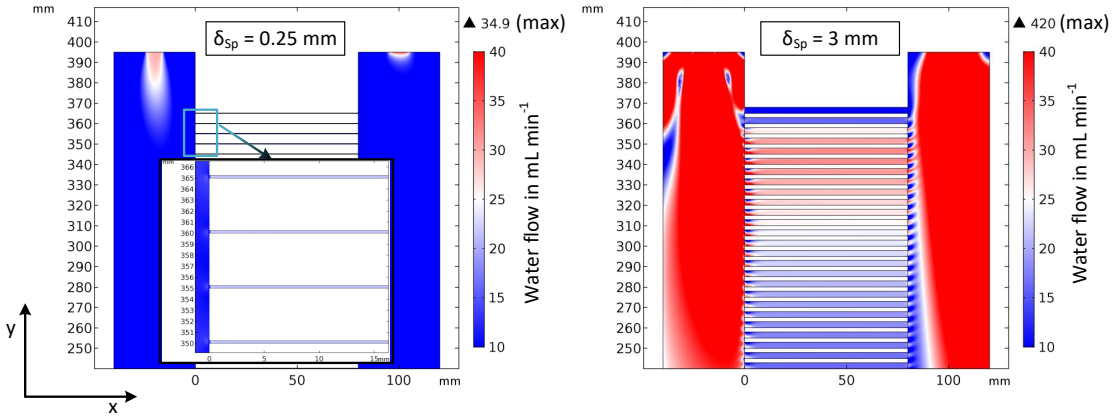

Figure 8.7. Volume flow field over Ω in mL min^{-1}, of calculations for $\delta_{\mathrm{Sp}} = 0.25$ mm and $\delta_{\mathrm{Sp}} = 3$ mm

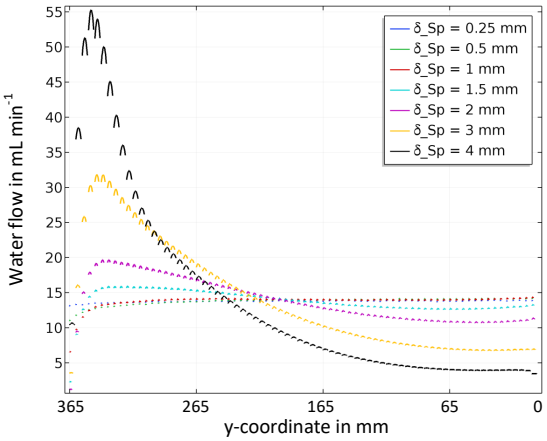

Figure 8.8. Volume flow over the y-coordinate, for different δ_{Sp}

volume flow stretches from $\dot{V} = 55$ mL min^{-1} to $\dot{V} = 4$ mL min^{-1}. Hereby it can be seen that less water is flowing through the first spacers, a maximum is reached for the third and further the volume flow is decreasing until the last one. An uneven volume flow results in uneven retention times of the water between the electrodes, whereas for each of them the same U_{cell} and I_{cell} are applied. This results in different removal rates and thus in a less overall performance.

For smaller $\delta_{\mathrm{Sp}} \leq 1$ mm, the volume flow rates are more evenly distributed, which is advantages if MCDI is used with a high amount of electrode pairs as usual in a commercial scale. Hereby, the volume flow rate is $\dot{V} = 13.77$ mL min^{-1} ± 1.05 mL min^{-1} (SD). After the first five spacers, the flow rate is $\dot{V} = 14.00$ mL min^{-1} ± 0.19 mL min^{-1} (SD).

To sum up the CFD model, a scheme for in- and outputs is pictured in fig. 8.9 In the

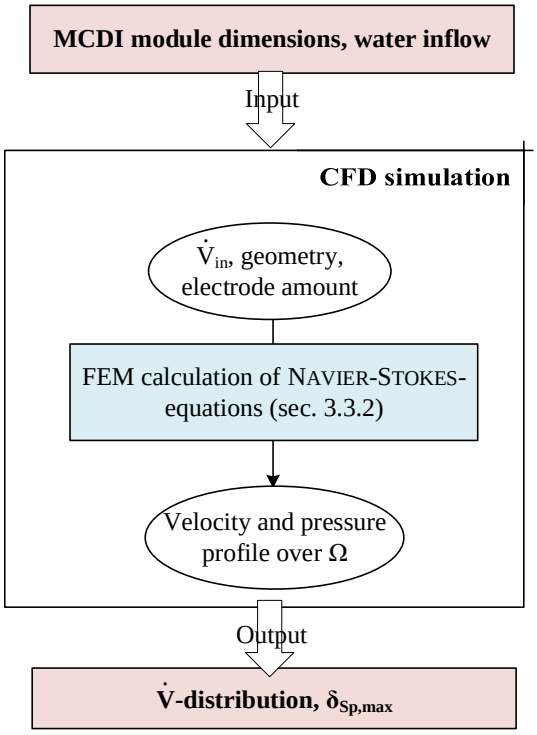

Figure 8.9. Process scheme of the CFD model with in- and outputs

CFD model, the geometry of the inside of an MCDI module can be changed without limits. The water volume flow as input variable can be varied and the distribution of $\dot{V}$ is output and $\delta_{\mathrm{Sp,max}}$ can be determined.

It can be concluded that CFD simulations showed

- when scaling up MCDI modules to a commercial size, the design needs to consider spacer widths in terms of even water distribution between all spacers so that a good desalination performance can be ensured
- the CFD model can determine maximum spacer width and minimum running-in part, before the first pair of electrodes is reached, for different applied volume flows and numbers of electrodes
- the spacer size needs to be $\delta_{\mathrm{Sp}} \leq 1$ mm with an inlet flow of $\dot{V} = 1\ \mathrm{L\,min^{-1}}$ to ensure equal retention times in all spacers
- the first pair of electrodes need to be mounted 65 mm below the water inlet of the module to further improve water flow distribution. In this case, the water flow was determined to $\dot{V} = 14.00\ \mathrm{mL\,min^{-1}} \pm 0.19\ \mathrm{mL\,min^{-1}}$ (SD) in the spacers.

8.3 FEM modelling of ion transport

In this thesis, the FEM modelling was carried out to implement ion movement to a transport model. To analyse the feasibility of solving the NPP equations in an FEM program, different simulations were carried out, whereby successively more terms of the equations (diffusion, migration and convection) and spacial dimensions were added.
In the end a combined model of ion transport and mD was tested for time dependent modelling of applied MCDI CCCD operation.

8.3.1 1D simulation

For the evaluation of the equation implementation in *COMSOL Multiphysics*™ *v5.6* a 1D simulation was carried out. The equation system was set up as explained in tab. 5.2, pos. 1 and 2. The geoemtry and mesh was set up as explained with fig. 5.4.
For different applied cell voltages, the potential and concentration profile over the spacer width have been evaluated. A cropped section close to the electrode boundary of $\phi(x)$ is pictured in fig. 8.10. U_{cell} from 0.05 to 1 V were applied, the concentration in the

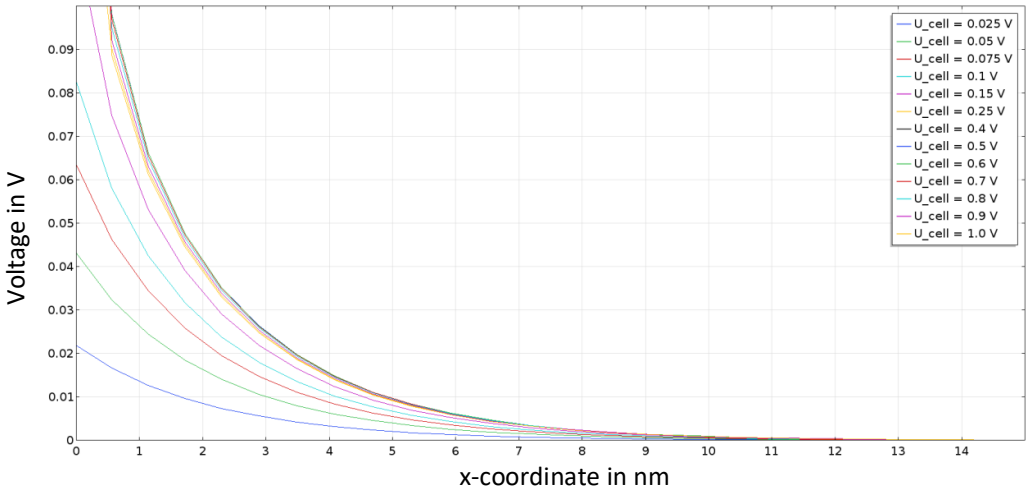

Figure 8.10. Progression of the electrical potential close to the electrode for different U_{cell}

spacer was set to $c_{\text{Sp}} = 20$ mM and the time-dependant solver was set to solve for the first 10 seconds, hence a potential profile has time to develop. It can be seen that the higher U_{cell}, the bigger the electrical double layer (see also sec. 2.1).

The potential profile is compared with the theoretical calculated value of the DEBYE length (see eq. 2.7)

$$\lambda_D = \sqrt{\frac{78 \cdot 8.854\text{E-}12\ \frac{\text{F}}{\text{m}} \cdot 8.314\ \frac{\text{J}}{\text{mol K}} \cdot 298\,\text{K}}{2 \cdot (96485\ \frac{\text{C}}{\text{mol}})^2 \cdot 1^2 \cdot 20\,\text{mM}}} = 2.13\ \text{nm}\ , \tag{8.1}$$

which is within the range of the resolved EDL in the 1D simulation. Furthermore, they fit with the profiles in literature (Butt et al., 2006, pp. 43-48).
The concentration profiles versus the spacer width for the same calculation are shown for different U_{cell} in fig. 8.11. It is pointed out that on the y-axis the concentration

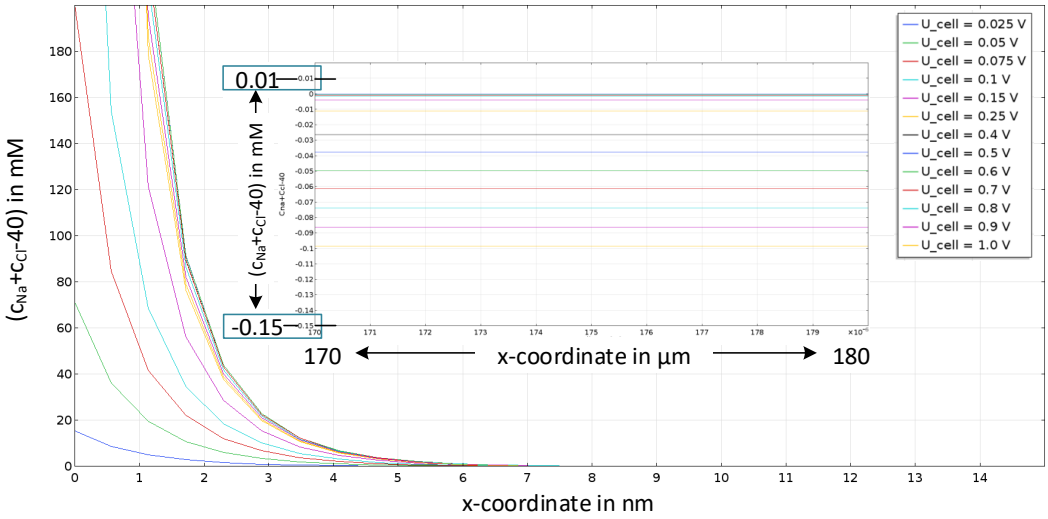

Figure 8.11. Progression of the concentration close to the electrodes and in the middle of the spacer for different U_{cell}

$c_{\text{Na}} + c_{\text{Na}} - 40$ mM is indicated, thus the difference to the inlet concentration of each ion. Here, the same is valid for the extension of the EDL as for the potential profiles as they are coupled with each other. This size is also within the range of in literature mentioned (Butt et al., 2006, pp. 43-48). Furthermore, a negative change in concentration in the middle of the spacer (see small figure inside fig. 8.11), which indicates the ion removal in the spacer. However, with $\Delta c_{\text{Sp}} = 0.069$ mM for $U_{\text{cell}} = 1.5$ V, this value is too low to match with MCDI desalination. Since only an initial concentration $c_{\text{init}} = 20$ mM is given no other flux or source was implemented. For this reason, the concentration in the middle of the spacer (bulk) is decreasing.
For this reason, a DIRICHLET BC for a constant concentration $c_{\text{Sp}} = 20$ mM at the point in the middle of the spacer was implemented in a further calculation, and U_{cell} was ap-

plied for 900 s and set to zero subsequently. The time-dependent solver was defined to process 1800 s (see fig. 8.12).
The results show that an equilibrium state is reached, where the bulk concentration remains the initial concentration and the EDL's are formed at the electrodes (see fig. 8.12), which indicates a more realistic picture of the expected concentration inside the spacer. As a post-processing step, the integral of the concentration over the spacer width was

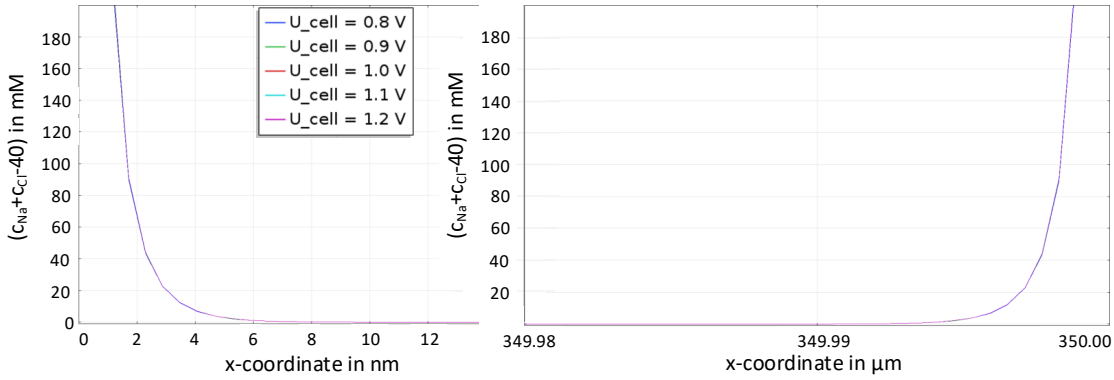

Figure 8.12. Progression of the concentration close to both electrodes for different U_{cell}, with implemented DIRICHLET BC

calculated for every time step and multiplied with assumed spacer length (0.16 m), depth (0.16 m) and amount (125) as well as with the molar mass of NaCl $M_{\text{NaCl}} = 58.5\ \text{g mol}^{-1}$, which results in a mass of salt inside the EDLs at all electrodes of a C-5 module. The data is presented for different applied U_{cell} in the following fig. 8.13. It can be observed

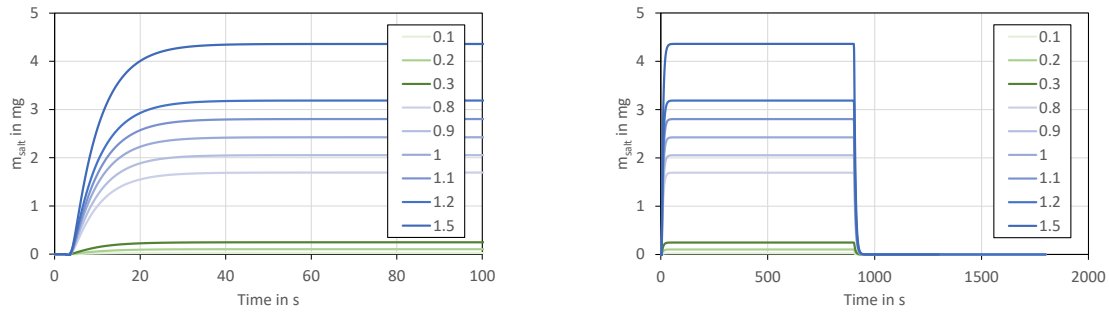

Figure 8.13. Adsorbed mass of salt versus time and for different U_{cell} in the 1D model. Left: first 100 s, right: total calculation time

that m_{salt} increases over time when a potential is applied (at $t = 0$). Furthermore, the higher the potential the higher the concentration in the EDLs. The stabilized values can

Table 8.2. Values for m_{salt} in the EDLs of a C-5 module according the 1D model for different U_{cell}

$\boldsymbol{U_{cell}}$ in V	**0.1**	**0.2**	**0.3**	**0.8**	**0.9**	**1**	**1.1**	**1.2**	**1.5**
$\boldsymbol{m_{salt}}$ in mg	0.02	0.10	0.25	1.69	2.05	2.42	2.80	3.19	4.36
$\frac{\boldsymbol{\partial m}}{\boldsymbol{\partial U_{cell}}}$ in mg V^{-1}	0.2	0.8	1.4	2.9	3.6	3.7	3.8	3.8	3.9

be taken from tab. 8.2. It can be seen that the calculated values for m_{salt}, using C-5 parameters, is very low. However, the almost linear tendency in the range $0.8 < U_{cell} < 1.5$ agrees with experimental data, which is shown by the very slowly increasing slope of mass between the U_{cell} steps ($\frac{\partial m}{\partial U_{cell}}$). Furthermore, the non-linearity for lower $U_{cell} = 0.1$ to 0.3 V, as it was calculated with the mD models in previous section and shown with experimental data, is also true for this FEM model (indicated by increasing $\frac{\partial m}{\partial U_{cell}}$ for low U_{cell}). The slope is calculated by the discretization

$$\frac{\partial m}{\partial U_{cell}} = \frac{m_n - m_{n\text{-}1}}{U_{cell,n} - U_{cell,n\text{-}1}} \; . \tag{8.2}$$

Hereby, $\frac{\partial m}{\partial U_{cell}} = 2.9$ mg V^{-1} for $U_{cell} = 0.8$ V shows an example for an approximation error, caused by a too high $\Delta U = 0.5$ V, which happens also, if the mesh size is too coarse. This effect is further explained below in the sec. 8.3.2.

As an overview, a scheme of in- and outputs to the 1D-FEM-simulation is pictured in fig. 8.14. With different U_{cell} and c_{in}, the concentration over x can be ressolved time-dependently and thus the EDL. The concentration in the EDL can give information about retained salt. In combination with an area factor Γ_{salt} can be calculated.

It can be concluded that

- the 1D model showed the feasibility of implementing the NPP equations in COMSOL
- the results for λ_D and EDL size as well as potential and concentration distribution over the spacer width and their change with different U_{cell} agree with literature values and tendencies with own experimental data
- the adsorbed mass values in the EDLs are not fitting to realistic data of MCDI modules, which is explained by the very simplified geometry in the simulation, which is an important factor in a spacial ion transport model
- no different ion movement behaviour in the electrodes, as it occurs in actual MCDI modules in macro-, meso- and micro pores was simulated

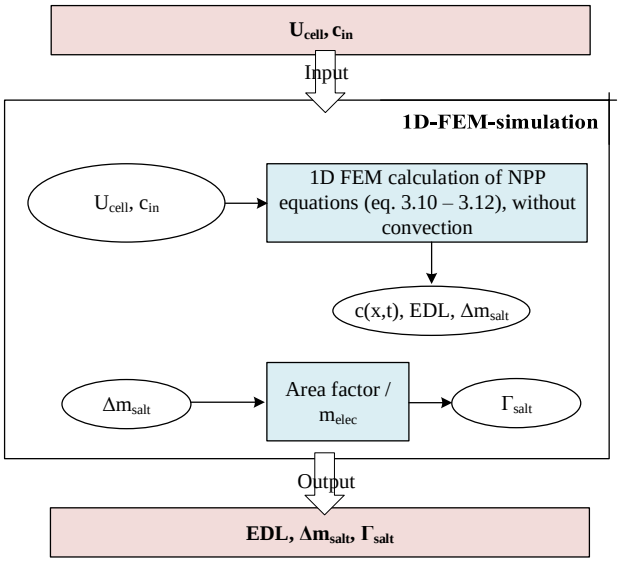

Figure 8.14. Process scheme of the 1D-FEM-model with in- and outputs

- the total surface of a porous electrode structure, where EDLs are formed is much higher than the plain electrode surfaces in the 1D model, which needs to be considered in further simulations
- introducing area factors can be considered to calculate actual SAC values
- the calculation time was $\approx$ 2.27 h.

8.3.2 Calculation time and mesh studies

Before the 2D simulation work is discussed, the results of a mesh study and the correlation with the calculation times and results is presented in this section.
Mesh studies were used to define the degree of refinement sufficiently enough to achieve adequate approximated results in acceptable calculation times. If a mesh is set up too fine, the results are very well approximated but the calculation times are sky rocketing. If the mesh is set up too coarse, the vice versa situation is given.
For every geometry, mesh studies were carried out. In this section, the results for the mesh study for a simplified geometry (only spacer of fig. 5.2, with electrode boundary conditions) is presented. Hereby, the mesh is changed in size for the overall geometry and at specified locations, where further mesh refinements are needed. Subsequently the results were analysed and compared with coarser mesh types and the calculation times were recorded (see fig. 8.15). In this study, a stationary solver was used to calculate the

gPDE and ECI interfaces (see sec. 5.2.1) coupled, with $c_{\text{in}} = 20$ mM and $U_{\text{cell}} = 1$ V. Visualized are the refinement steps on the x-axis, with 0 meaning no refinement was

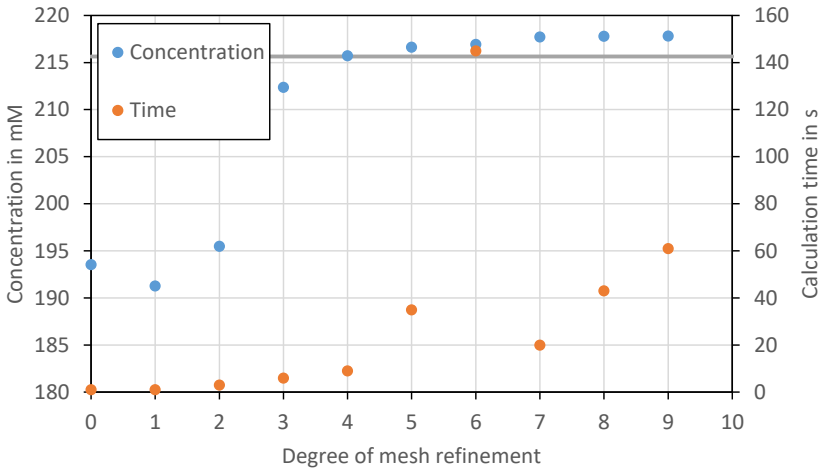

Figure 8.15. Results of electrode concentration versus calculation times for a mesh study in a 2D geometry

carried out. It can be seen that the concentration is rising and approaches a value below 220 mM, with changed refinement. The grey line in fig. 8.15 indicates 1% change to the concentration value with the greatest refinement at step 9 ($c_{\text{elec}} = 217.82$ mM). Everything above the line is considered as sufficient approximated result. This change is explained as approximation errors when Δx of the discretized equations (see sec. 3.2.1) is too big. This error is added up from cell to cell and results in a total difference of concentration in this case at the electrode boundary. The higher the changes expected in the spacial direction, the smaller the mesh has to be defined in this section.
The refinement was increased between step zero and six in y-direction towards the electrodes. Between step seven and nine, the refinement level of step four was improved in x-direction. It can be seen that the narrowing of the mesh in y-direction highly increases the accuracy, while calculation times are not significantly increasing. The further increase of refinement in x-direction does not raise the accuracy of the results but increases calculation times relevantly. For these reasons, refinement degree four was decided to be accurate in enough and requires the lowest calculation time, with $c_{\text{elec},4} = 215.74$ mM and $t_{\text{calc}} = 9$ s.

With this mesh study, the refinement of the grid towards electrodes, to calculate the NPP equations in a 2D domain was defined and used for further simulations in this

thesis. It is pointed out that the calculation time is a significant factor for a frequently used calculation tool, for the design of MCDI applications and hence further analysed in subsequent modelling studies.

8.3.3 2D ion transport simulation

The one dimensional simulation in sec. 8.3.1 revealed that the geometry was too much simplified for a spacial ion transport model. Furthermore, the implementation of a convection term perpendicular to the electromigration can not be added. For this reason, 2D FEM simulation studies were carried out, so that the implementation of a water flow is possible and periodic charge and discharge phases can be simulated.

Model transfer from 1D simulation

Firstly, the 1D model was transferred to two dimensions and the spacer was extended to a rectangle with width and length of $b = 200$ µm and $l = 1000$ µm, whereas the upper and lower sides are the electrode boundary conditions. In the middle of the spacer, a DIRICHLET BC was set for remaining constant concentration in the spacer, as in the 1D simulation.
To further stabilize the solving system and achieve convergence of the solver, U_{cell} as a so called load to the system needs to be ramped (COMSOL AB, 2017b), meaning the input parameter is slowly increased over time by adding a ramping function $f_{\text{rm}}(t) = \frac{1}{150}\,t$ for $0 < t \leq 150$ and $f_{\text{rm}}(t) = 1$ for $t > 150$, as a factor to the electrode boundary condition. $U_{\text{cell}} = 0.8$ V was developed after $t = 150$ s, the solver was set to solve until $t = 200$ s. As inlet concentrations $c_{\text{in,Na}} = 20$ mM and $c_{\text{in,Cl}} = 20$ mM was set. The concentration profiles ($c_{\text{Na}} + c_{\text{Cl}} - c_{\text{in}}$) of the last time step over the spacer width close to the electrode, at the positions $x = 0, 250, 500, 750$ and 1000 µm are presented in fig. 8.16. Since the concentration profiles at all positions for x are exactly equal, only one line is visible in the diagram. The cropped section shows the EDL of the negative charged electrode boundary. The y-axis shows summed Na^+ and Cl^{-1} concentrations in mM, with subtracted bulk concentrations. The profile is equal to the 1D simulation and is thus considered to be transferred correctly and no numerical errors with implementing the x-direction were created. To achieve the results, a calculation time of $t_{\text{calc}} = 715$ s was needed.

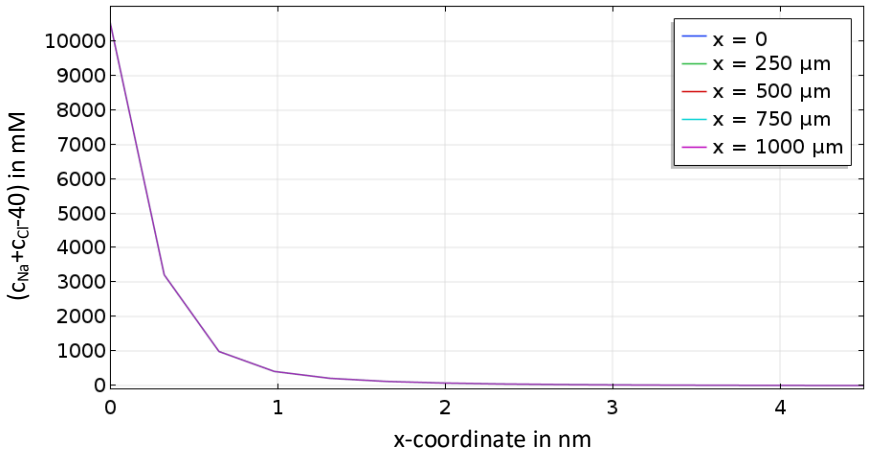

Figure 8.16. Concentration profile close to the EDL for different x-positions in the 2D model

Space charge density and convection term

As a next step, a constant velocity for the convection term was added. A subsequent mesh study (as in the previous sec. 8.3.2) revealed, that calculation times are exponentially higher so that the mesh size in y-direction needed to be made more coarse. Hence, the amount of cells in y-direction was lowered to $n_{\mathrm{me,y}} = 150$. Hereby, a growth rate of 50 was chosen from electrode to the middle of the spacer. This results in a size of the first cell next to the electrode boundary of $\Delta y = 100$ nm, which is bigger than λ_{D}. Due to highly increasing calculation times, the amount of cells cannot be increased in y-direction and in view of resolving the potential over y correctly and achieving convergence, the growth rate can not be increased either, which could lower Δy.
In x-direction, $n_{\mathrm{me,x}} = 50$ and no growth rate was set, with regard to the implementation of a convection term. Fig. 8.17 shows the 2D mesh of this study. The electrode boundary conditions remain the same, however the constant concentration condition in the middle of the spacer was moved to the left boundary of the rectangle as an *inflow* boundary for the salt ions.
The calculation was stopped at $t = 5$ s, due to calculation times were skyrocketing. At this point, U_{cell} was ramped to 32 mV and c_{in} to 8E-4 mM. As expected, the concentration profile next to the electrode is resolved very roughly and shows a too high λ_{D}, which is caused by approximation errors due to too big cell size Δy (see fig. 8.18). Furthermore, shortly before the electrode the concentration switches sign to negative, which is considered a numeric calculation error. It can be seen that the implementation

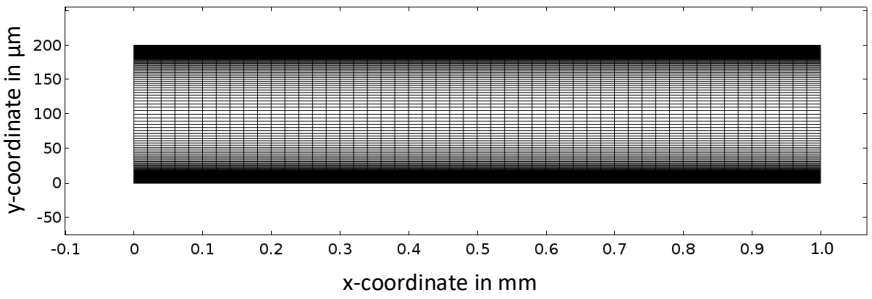

Figure 8.17. Mesh of the simplified 2D geometry of the spacer

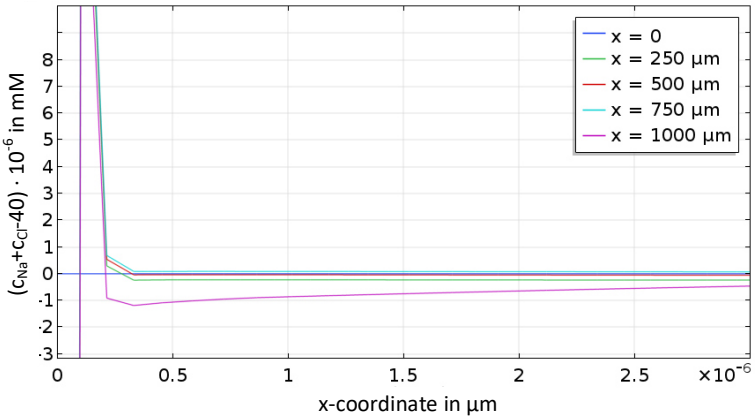

Figure 8.18. Concentration profile close to the EDL. Snapshot while $U_{\text{cell}} = 32$ mV and $c_{\text{in}} = 8\text{E-}4$ mM

of the convection term causes lower bulk concentrations towards the end of the spacer, which indicates higher desalination for longer retention time of the salt water in between the electrodes.

Hence, this additional term further causes a much higher concentration change over the extend of the spacer. This higher changes force the solver to use smaller time steps Δt for discretization, to solve Fick's second law (see sec. 5.2.1). The higher Δx and Δy, the smaller Δt needs to be. This results in reciprocal values of ≈ 15000 s^{-1} for the time steps ($\Delta t = 6.67\text{E-}5$ s) and thus in very high calculation times. Vice versa, the time steps are smaller but the calculation needs longer, due to the equations need to be solved for more cells. To achieve the results of the first five seconds, a calculation time of $t_{\text{calc}} = 65242$ s ($\widehat{=}$ 18.12 h) was needed.

When modelling the NPP equations with the FEM, they have to be solved coupled since

the equation for the concentration distribution (NERNST-PLANCK) is highly depending on the result of the equation for the potential distribution (POISSON) and vice versa. Thus they are connected through a space charge density, defined by the ions concentration (see sec. 3.3.1). However, in the spacer channel (not in the EDLs), charge neutrality is given for monovalent salts, since $c_1 = c_2$ and $z_1 = -z_2$ (see eq. 3.12).

Charge neutrality

To simplify the model equations for drastically lowering the calculation times, charge neutrality was assumed ($\sigma = 0$) in the whole spacer, to be able to calculate the ion transport model in a reasonable time, with small cells in nm scale close to the electrodes. Firstly, the previous model without conductivity term was re-calculated to ensure the possibility of resolving the EDLs. Additionally, the domain was increased by adding running-in and -out parts (see fig. 8.19, $x = -10$ to 0 mm and $x = 80$ to 90 mm), before and after the electrodes ($x = 0$ to 80 mm) and expand the electrode to its half original size $l = 8$ cm. Since the increase of the domain implicates a higher cell number,

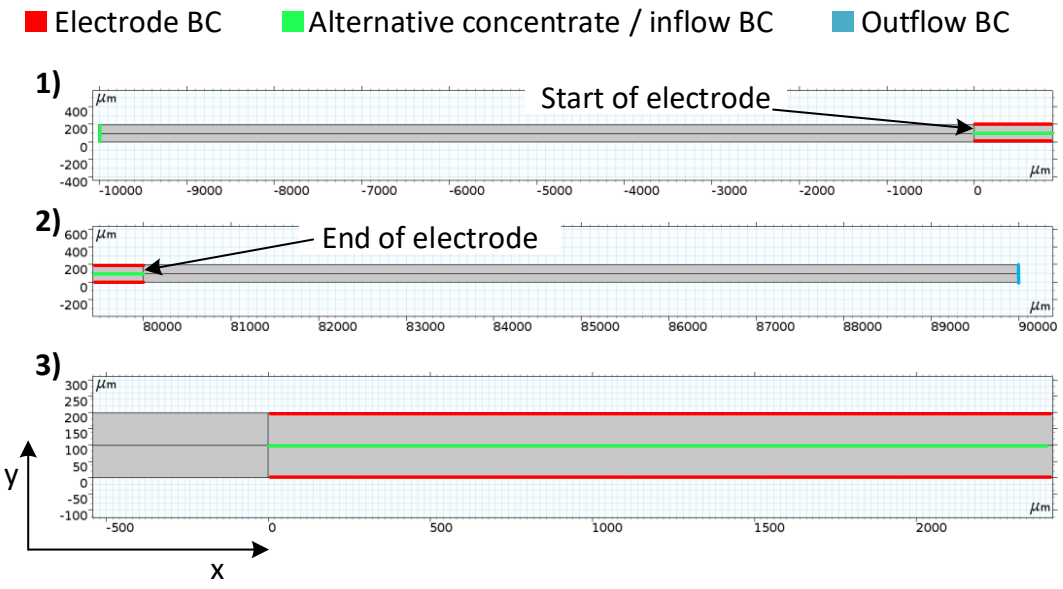

Figure 8.19. 2D geometry of spacer with inflow, outflow, concentrate and electrode boundary conditions. 1) Running-in part before electrodes, 2) running-out part after electrodes, 3) start of electrodes at $x = 0$

the resolution of the mesh in y-direction was further decreased to obtain reasonable

calculation times below $\leq$ 2 h. The amount of cells was set to $n_{\mathrm{me,y}} = 400$, with an exponential growth rate of 400 between electrode and middle of the spacer and $n_{\mathrm{me,x}} = 100$ without growth rate.
After the calculation time of $t_{\mathrm{calc}} = 1.57$ h, which was significantly smaller than of the simulation with $\sigma \neq 0$, the concentration progression over the spacer width at different positions of x at the time step $t = 60$ s, can be analysed and is highlighted in fig. 8.20. The different colours represent various positions at $x =$ -10, -5, 0, 40, 80, 85 and 90 mm.

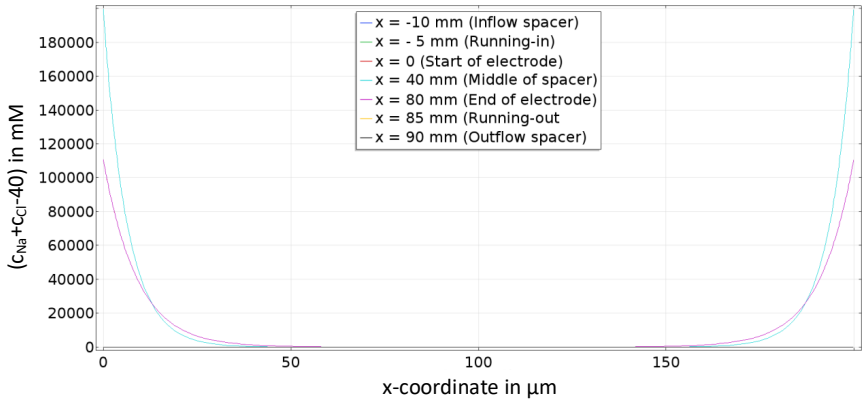

Figure 8.20. Concentration profile over spacer width at $t = 60$ s and U_{cell} 0.8 V

The curves of the first and the latter, at position $x =$ -5 and $x = 85$ and $x = 0$ and $x = 80$ mm are laying on top of each other. It can be seen that there is a difference in the concentration profiles between the beginning of the electrode and the middle. The progressions at the running-in and out parts is constantly zero.

By analysing the concentration of Na^+ ions at the cathode's boundary over time, it stands out that it is linearly increasing (see fig. 8.21). As charge neutrality is given, ϕ over the spacer width becomes linear as well as $\Delta\phi$ constant (see eq. 3.11) and thus it does not change with the concentration. Hence, the electro migration force remains constant and salt ions can accumulate at the electrode's interface (see eq. 3.10). This effect at position $x = 40$ mm is pictured in fig. 8.22. It can be seen that also the concentration at the electrode and the accumulation of salt in the spacer increases linearly, because of constant $\Delta\phi$. The concentration $c_{\mathrm{elec,Na}} \approx 200$ M and $m_{\mathrm{salt}} > 450$ g show unrealistic high values after $t = 200$ s of applying $U_{\mathrm{cell}} = 0.8$ V. This is due to the missing space charge density calculation, where a constant concentration of $c = 20$ mM at the middle of the spacer creates an infinite source of ions, which migrate towards the electrode.

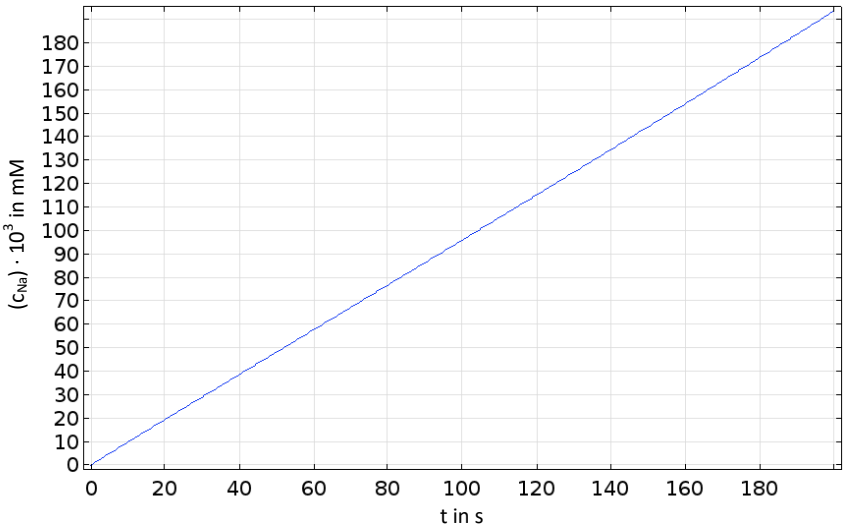

Figure 8.21. Concentration of Na^+ at the anode in 10^3 mM

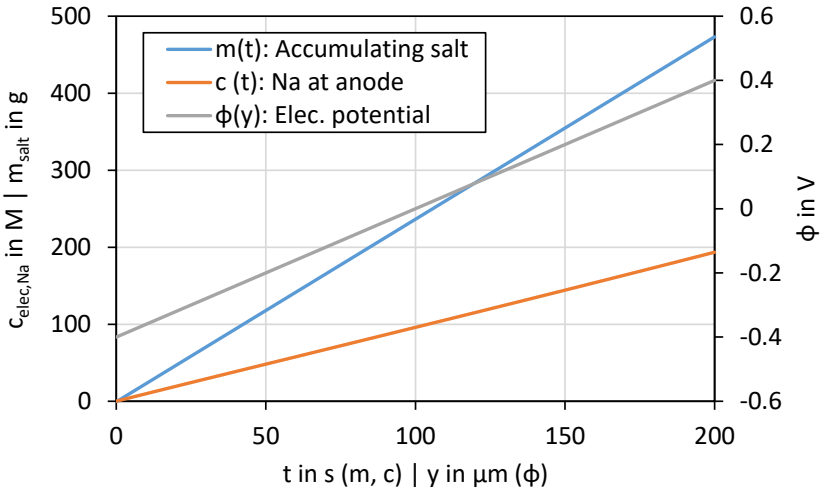

Figure 8.22. Concentration of Na^+ at the electrode boundary and accumulating salt in spacers of assumed C-5 geometry over time and potential over the spacer width (all at position $x = 40$ mm)

Since

- the spacer has the function to transport the ions to the porous electrodes and not to store them
- the EDLs formed at the electrodes do not contribute to the absolute amount of stored ions, relatively to the amount in the porous electrodes
- in real MCDI modules, the spacer-electrode interface is not a wall where salt can accumulate and
- the constant concentrate boundary condition needs to be set to the inlet of the spacer for realistic modules

the charge neutrality in the spacer is considered for further 2D FEM simulation of the ion transport inside the spacer. Furthermore, the exact reproduction of the EDL shape at the spacer electrode interface is not needed.

Charge neutrality and convection term

As a next step, a convection term was added to the system and the in- and outflow boundaries were defined. Hereby, the velocity vector of eq. 3.10 was set to $\vec{v} = \binom{0.007}{0}\,\mathrm{m\,s^{-1}}$, which relates to the converted volume flow of $\dot{V} = 1\,\mathrm{L\,min^{-1}}$ for a C-5 module. The convective flow in y-direction was suppressed. The concentration boundary in the middle of the spacer was erased. Due to a significant transport term in x-direction was added, a change in the concentration profile is expected in respective orientation. Thus, to calculate the mass adsorption, an area integral over the spacer part in between the electrodes was used, instead of the line integral in previous section and multiplied by the out-of-plane depth of the electrodes (16 cm) and molar mass of NaCl.
In fig. 8.23, the concentration $c_{\mathrm{Na}} + c_{\mathrm{Cl}} - c_{\mathrm{in}}$ is presented for cropped sections of the spacer. A non-uniform distribution in x-direction can be observed. The further to the end of the electrode, meaning the longer the retention time of the salt water in the spacer, the more salt migrated towards the electrodes boundary. Furthermore, it stands out that the EDLs are thicker than in previous models, but therefore have a lower maximum concentration $c_{\mathrm{Na}} + c_{\mathrm{Cl}} = 376 + 40$ mM (indicated at the top of the colour bar) at the interface spacer-electrode.

The mass of salt accumulation recalculated for a C-5 module, over time for different U_{cell} is presented in fig. 8.24. It is observed that the ions are not accumulating without

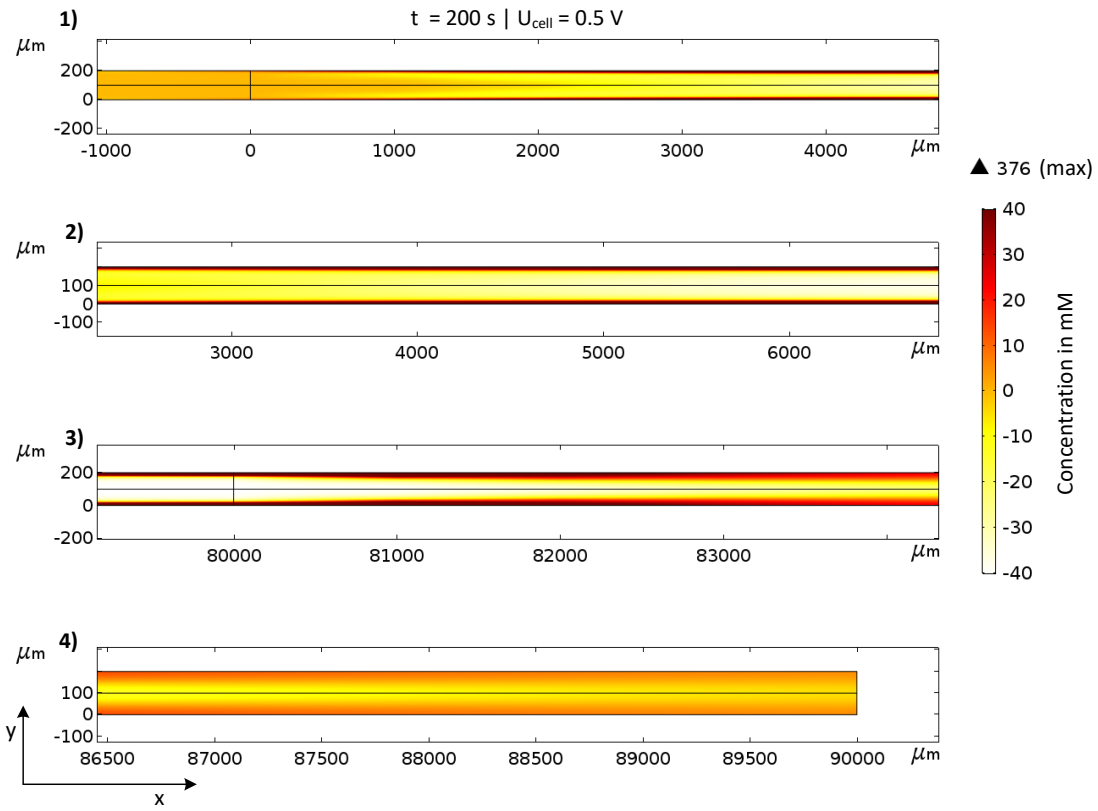

Figure 8.23. Concentration profiles over cropped section of the spacer. 1) Start of electrode, 2) middle of electrode, 3) end of electrode 4) running-out and outflow

limit, but reach a threshold after a maximum of $t = 50$ s. This was achieved by moving the concentration boundary condition to the inflow and further adding an outflow boundary at the end of the spacer.

For $U_{\text{cell}} = 0$ V, the model does predict zero and for $U_{\text{cell}} = 1.5$ V, $m_{\text{salt}} = 22.19$ mg of salt adsorption in C-5 equivalent electrodes. The results for the tests with the other cell potentials lay in between. It is noticeable that the change of m_{salt} and thus Γ_{salt} is parabolic and not linear, which was expected for $U_{\text{cell}} \geq 0.8$ V. (see tab. 8.3). In tab. 8.3, the values for the SAC of the $\text{mD}_{2.33}$ model are listed, to be able to compare the most promising with the recent model. Therefore, the scaling factor $s_{\text{mD2.33}} = \frac{\Gamma_{\text{salt,mD2.33}}}{\Gamma_{\text{salt}}}$ was introduced, which is constant when the tendency of models are the same. The decreasing factor s indicates the parabolic and not linear tendency of SAC over U_{cell}, which is pronounced in fig. 8.25. Hereby, the SAC results of the mD_0 model is inserted in the diagram for comparison. Especially for $U_{\text{cell}} > 0.5$ V, where the mD model becomes linear, the FEM model stands out with its parabolic progression. It needs to be pointed

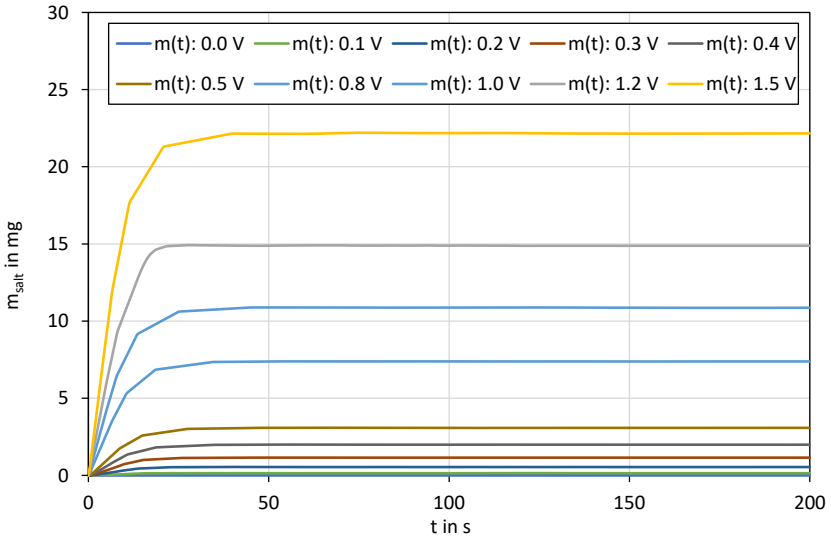

Figure 8.24. Salt accumulation in the spacer over time for different U_{cell}

Table 8.3. Values for salt accumulation and SAC in the 2D model with convection term and charge neutrality. U_{cell} in V, m_{salt} in mg, $\Gamma_{\text{salt}}(\cdot 1000)$ in µg g^{-1}, $\Gamma_{\text{salt,mD}}$ in mg g^{-1} and the scaling factor s.

$\boldsymbol{U_{\text{cell}}}$	0.0	0.1	0.2	0.3	0.4	0.5	0.8	1.0	1.2	1.5
$\boldsymbol{m_{\text{salt}}}$	0.00	0.14	0.54	1.15	1.99	3.08	7.38	10.86	14.88	22.16
$\boldsymbol{\Gamma_{\text{salt}}(\cdot 1000)}$	0.00	0.18	0.70	1.49	2.57	3.98	9.54	14.03	19.21	28.62
$\boldsymbol{\Gamma_{\text{salt,mD2.33}}}$	5.03	5.10	5.32	5.66	6.11	6.65	8.62	10.14	11.74	14.26
$\boldsymbol{s_{\text{mD2.33}}}$	$\to \infty$	27768	7618	3811	2378	1670	904	723	611	498

out that the y-axis shows the SAC in two different scales, in µg and mg salt per g electrode respectively, thus a scaling factor $s = 1000$ needed to be applied on the axis. This factor is influenced by differences in adsorption area, whereas in this case the much smaller surface of the electrode's interface to a porous active carbon structure is given. Stoeckli and Centeno (2005) found that the external area of porous active carbon material can be between $S_{\text{E}} = 20$ and 250 m^2 g^{-1}. This would lead to an external surface (macro- and meso pores) of present C-5 electrode of $A_{\text{E}} = 62$ to 774 m^2, whereas the electrode spacer interface has an active area of $A = 256$ cm^2. The difference is in the dimension of the scaling factor s.

It can be concluded that

- the 1D model was successfully transferred to a 2D model
- adding physics in x-direction (perpendicular to the electrodes surface), do sky-

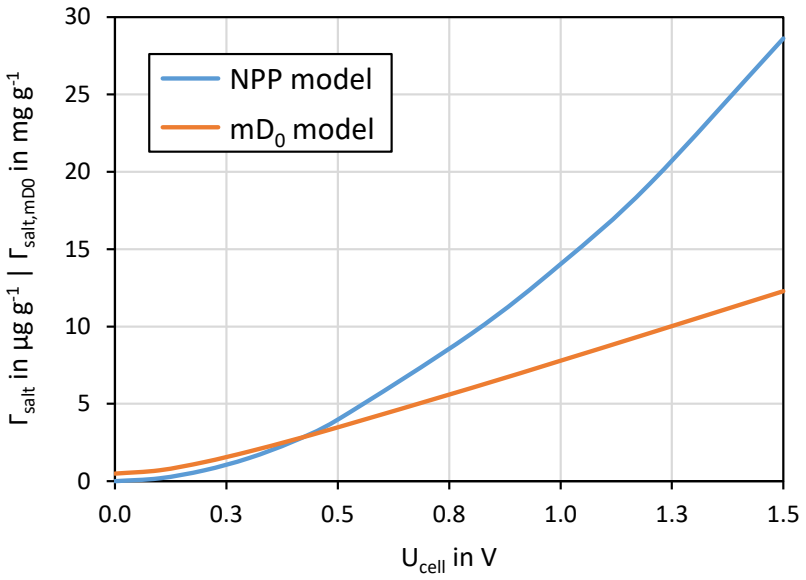

Figure 8.25. SAC over $U_{cell}$of the 2D FEM model with convection and the mD_0 model

rocket the calculation times

- by introducing charge neutrality in the spacer, reasonable calculation times can be achieved
- SAC values do fit experimental data after introducing a scaling factor to compensate the area increase due to the porous structure of activated carbon, for low $U_{cell} \leq 0.5$ V.

Especially for cell voltages > 0.5 V, the range in which applied MCDI takes place, the model does not agree with experimental data. Also the tendency of the SAC development over U_{cell} does not match the almost linear progression at real MCDI applications. What is missing for the pure ion transport model with the NPP equations, is a factor for adsorbing and for absolute pore capacity, which restricts ion adsorption and counter acts as a resistance at higher cell voltages. For this reason, a combination of the transport model with the modified Donnan model is considered in the next section.

8.4 Combination of FEM and mD models

A study for the combination of the time-dependent transport model with the mD model for ion adsorption, was carried out to simulate real MCDI desalination in CCCD mode. Hereby, the electrode spacer boundary was set as the interface of both models and the

geometry was extended by the sub-domain shown in fig. 5.2. In between Ω_1 and Ω_2, a thin diffusion barrier was implemented for modelling the IEM (see the domain area definition in sec. 5.2.2). It is noted that to simplify the model for 1:1 salts, the spacer was halved and symmetry was assumed in the middle (at $y = 0$), meaning a ROBIN BC was set, which does not allow a flow in y-direction and sets all shear stress for the fluid flow to zero. Since only the anode was modelled, only the ion concentration of Na^+ was set as input parameter for the model, assuming the same adsorption behaviour as NaCl for both electrodes.
A laminar flow was calculated stationary, before the ion transport to model the velocity field, which was used as input for $\vec{v}$ for the NPP equations in Ω_1. In Ω_2, the convection term was neglected.
To implement the mD model, the global equations of tab. 5.4 were solved coupled with the NPP equations and `V_set` was set as input parameter for the electrode BC. Hereby, a constant I_{cell} was set.
To compare this model with the previous NPP models, the concentration profile and the remaining salt in the spacer is evaluated and shown in fig. 8.26. The concentration profile is pictured at $x = 40$ mm thus in the middle of the electrode, over the y-coordinate, meaning for $0 < y < 250$ µm the electrode is present and for $250 < y < 350$ µm the spacer. It can be seen that a constant concentration is built up inside the electrode and an EDL at the spacer interface. The higher the adsorption time, the higher the concentration. The concentration c_{Na} in the spacer away from the electrode, approaches $c_{\text{Na}} - c_{\text{in}} = -20$ thus zero (with $c_{\text{in}} = 20$ mM), indicating all salt is adsorbed in this time in between the electrodes.

Furthermore, it is observed that the salt accumulation in the spacer is negative in this model (fig. 8.26, bottom). Since the adsorption of ions was shifted to domain Ω_2, the spacer functions solely as carrier for ions towards the electrodes and for the water towards the outflow boundary as in real applications.
The mass is calculated by the area integral, times length of all C-5 electrodes and molar mass of NaCl, assuming the counter electrode adsorbing the same amount of Cl^- ions. It is observed that the higher I_{cell} (blue curves), the stronger the adsorption in between the electrodes. Furthermore, an overshooting after the bulk concentration was reached ($m_{\text{salt}} = 0$) and no more ions can be adsorbed. This must be caused by a backflow from the electrodes in the spacer and not from approximation errors of the solver, since after decreasing the cell sizes to reduce calculation errors, the same overshooting was still observed.

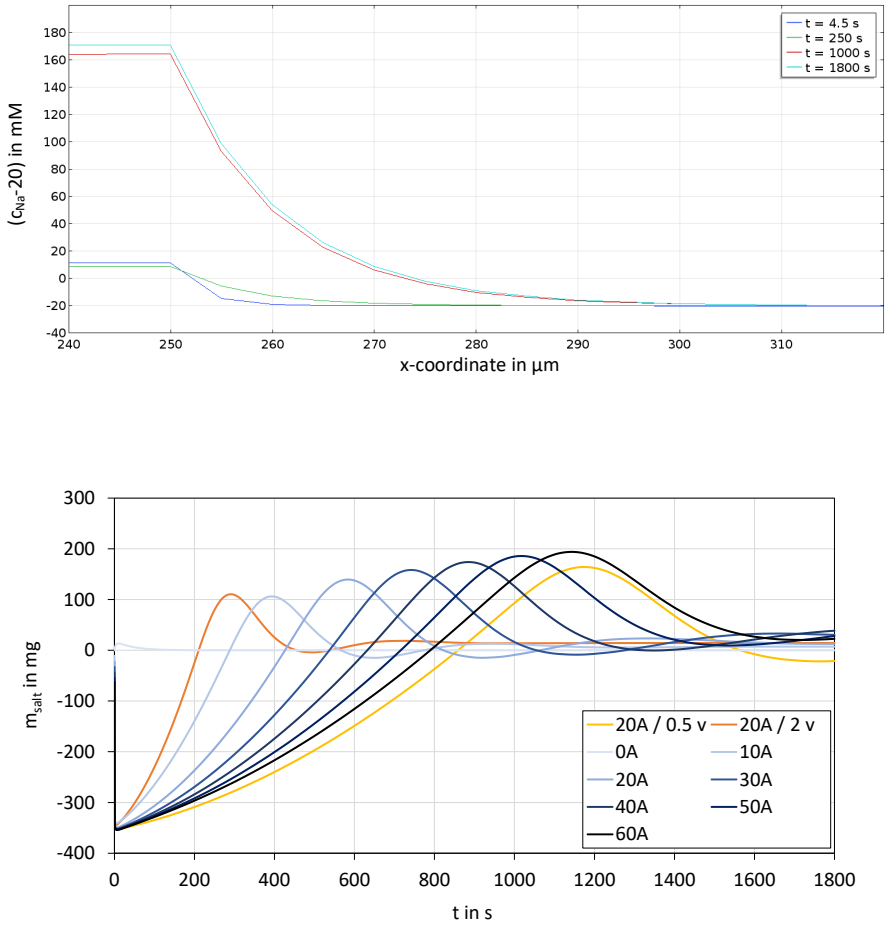

Figure 8.26. Concentration profile of Na^+ over the electrode and spacer width (top) and salt accumulation over time (bottom) calculated by the 2D combined model

The orange and the yellow curve picture the mass adsorption for $I_{\text{cell}} = 20$ A and halved or doubled inlet velocity, respectively. This shows that the higher the velocity, the higher the potential of salt adsorption, since more salt is fed to the spacer.

In fig. 8.27 the distribution of ions across the spacer and electrode domain is pictured at different time steps, at the start (left) end the end (right) of the electrode for different time steps. In this case, $I_{\text{cell}} = 30$ A was set. At $t = 0$ the domains show throughout the initial concentration $c_{\text{init}} = 20$ mM of Na^+. From the first second, ions are adsorbed into the electrode, also from the spacer of the running-in part. After 10 s, the first 3 mm of electrode possess a concentration > 20 mM above inlet concentration (thus > 40 mM absolute). Elevated concentrations are detected at the end of the electrode at $t \approx 1200$ s, after that the concentration in the running-out part starts increasing and thus also at the outlet of the spacer.

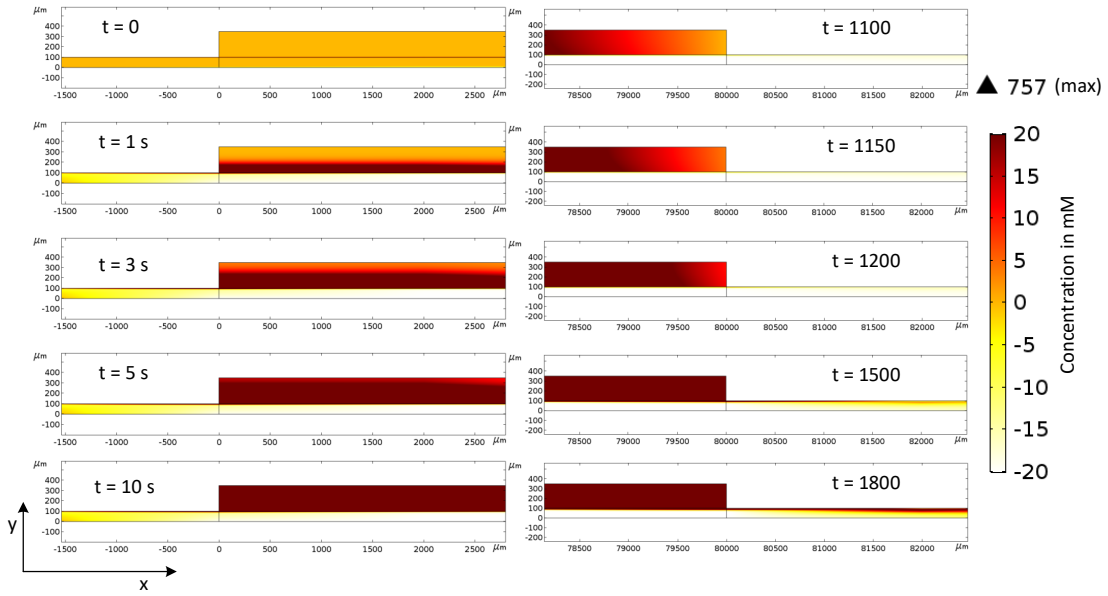

Figure 8.27. Na^+ distribution over spacer and electrode calculated by the 2D combination model. Left: start of electrode, right: end of electrode. I_{cell} 30 A.

Since a transport model in x-direction was implemented, it is possible to analyse the averaged concentration of the outflow boundary over time and compare the result with experimental data. Fig. 8.28 shows the outlet concentration over time of different I_{cell}, calculated by the combined 2D model. As in fig. 8.26 also here can be seen, the higher I_{cell}, the stronger and the longer the adsorption process. Comparing this model with the experimental data from fig. 7.6, it points out that the quicker adsorption for higher I_{cell} fits to data, but not the longer adsorption time. Since the SAC does not change for different applied currents, longer adsorption duration is not expected and thus is a incorrect calculation by the model. Furthermore, the adsorption speed is constant in theory. The slight increase of c_{out} in the first part of adsorption is hence not correct in the model.

Nevertheless, it was found that the potential over the electrode's macro pores $\texttt{Vma} = U_{ma}$, and the external resistance R_{ext} of the mD equations (see tab. 5.4) have a high influence on the adsorption behaviour.
For this reason, both parameters have been adjusted and c_{out} was analysed (see fig. 8.29) Hereby R_{ext} is stated in mΩ and for U_{ma} the size of its divisor; the higher the less weight is given for U_{ma} to calculate U_{set}.
It is observed that by increasing R_{ext} and the divisor of U_{ma}, the adsorption periods are increasing, since then U_{set} is rising as well, which is the applied voltage to the electrodes

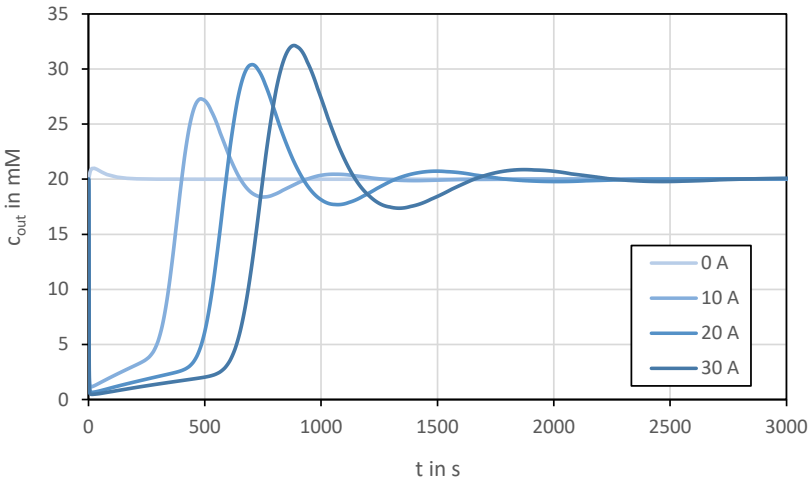

Figure 8.28. Concentration of Na^+ averaged over the outlet of the spacer, calculated by the 2D combined model

and responsible for the size of the EDLs. Hereby, the adsorption speed is closer to constant (flat c_{out}) for higher I_{cell}.
It is pointing out that for $R_{ext} = 27$ mΩ and the original U_{ma} value (divisor 1), the adsorption duration is longer for lower I_{cell}, which agrees with experimental data. However, the adsorption amount is much higher for lower I_{cell}, which contradicts to real MCDI desalination.
Considering the SAC values, the model with $R_{ext} = 27$ mΩ and U_{ma}-divisor (see `vma_ramp` in tab. 5.4) of 500 (fig. 8.28) fits best for desaslination with $I_{cell} = 20$ A. By using eq. 6.2 and eq. 6.3, $\Gamma_{salt,20A} = 12.14\ mg\,g^{-1}$ and $\Gamma_{salt,30A} = 15.95\ mg\,g^{-1}$ was calculated for the combined 2D model. The experimental data revealed, $\Gamma_{salt,20A} = 13.80\ mg\,g^{-1}$ and $\Gamma_{salt,30A} = 12.62\ mg\,g^{-1}$, respectively.

In fig. 8.30, an overview of the process of the combined model with in- and outputs is given. Here, I_{cell}, c_{in}, $\dot{V}$ and R_{ext} can be varied to achieve the effluent concentration dependent on time and thus also the SAC value.

The studies for the combined model of 2D ion transport equations with the analytical mD model can be concluded to:

- The inclusion of an electrode domain, separated with a thin diffusion barrier to simulate the ion exchange membrane, enables the time-dependant calculation of the effluent concentration

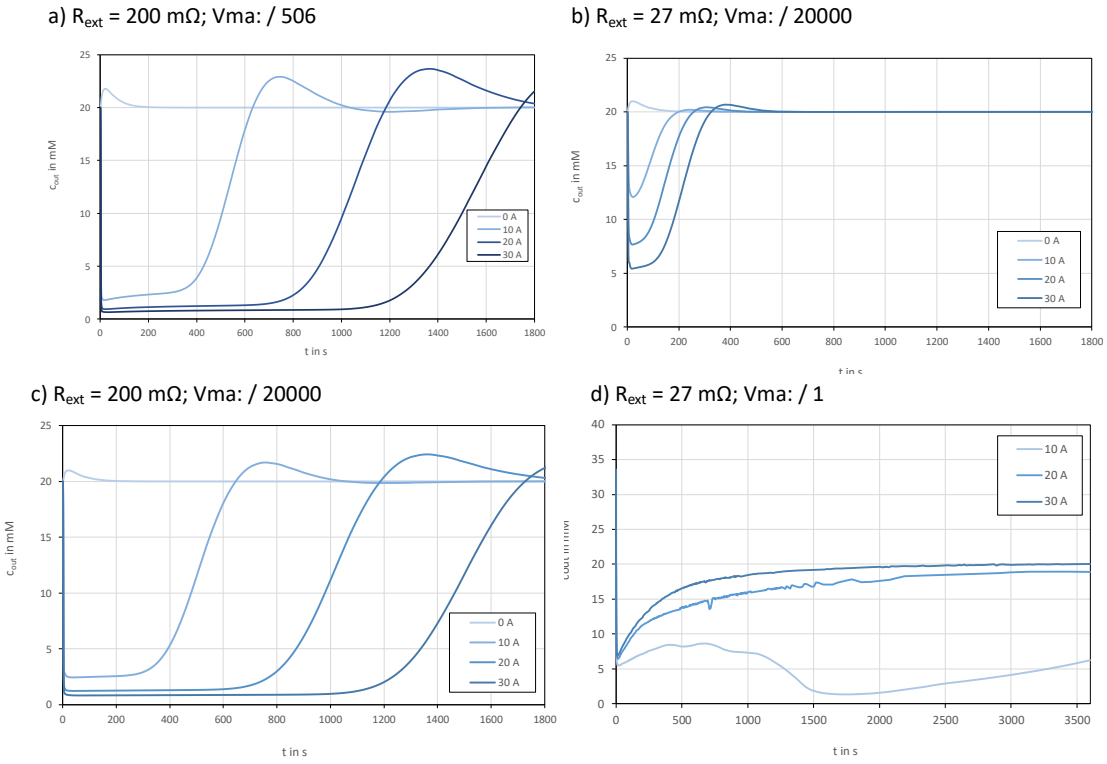

Figure 8.29. $c_{\mathrm{Na,out}}$, averaged over the outlet of the spacer, with adjusted values for R_{ext} and U_{ma}

- the values for c_{out} show same tendency as for experimental data, but not for changing I_{cell}
- the external resistance and implementation of the potential over the electrode, to calculate U_{cell} and I_{cell} for the electrode's boundary need further development and adjustments to fit the model to experimental data
- a maximum cell voltage U_{max} can not be implemented in the model
- calculated SAC values are within the range of experimental data for specific I_{cell}= 20 to 30 A, $R_{\mathrm{ext}} = 27$ mΩ and U_{ma} weighting of 500^{-1}.

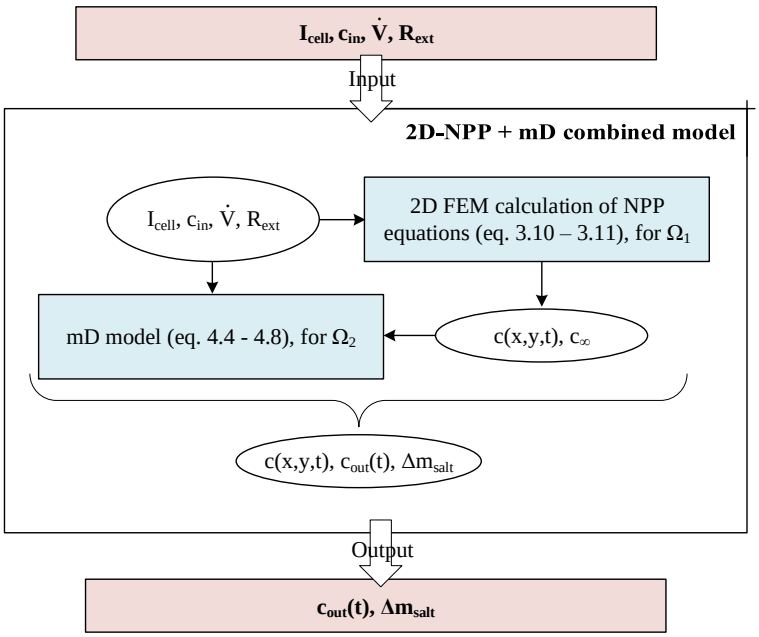

Figure 8.30. Process scheme of the 2D-FEM-simulation combined with the mD model and their in- and outputs

9 Development of a simplified calculation tool

The previous sections showed that for the fully two dimensional model of the ion transport through an MCDI module, very high calculation times and still further developments are needed to create a handy calculation tool. Especially for higher U_{cell}, the analytical mD models show promising results and are used together with electronic RC equations to predict the performance of MCDI CCCD operation applications.

9.1 Theory

The typical MCDI desalination behaviour is pictured in fig. 7.6 and fig. 7.9. It is pointed out that during a constant current charge phase, c_{out} is increasing before the actual salt adsorption capacity is achieved, which happens when enough ions are adsorbed that U_{max} is reached and I_{cell} is forced to decrease.
It was found that this turning point occurs at a certain percentage of the SAC value, which can be determined by experiment. Subsequently, the SAC calculated with the $\mathrm{mD}_{2.33}$ model for a set U_{cell} can be reevaluated for applied MCDI operation to an useable $\Gamma_{\mathrm{salt},\eta}$

$$\Gamma_{\mathrm{salt},\eta} = \eta_{\mathrm{SAC}} \cdot \Gamma_{\mathrm{salt,mD}} \ . \tag{9.1}$$

Longer than this point, charge phases must not be operated, since a constant effluent quality is desired.

With eq. 2.24, the charge efficiency Λ can be calculated, by comparing adsorbed salt with the applied charge in a practical experiment. With given Λ, the salt removal η_{rem} can be predicted as

$$\eta_{\mathrm{rem}} = \frac{\dot{n}_{\mathrm{ads}}}{\dot{n}_{\mathrm{in}}} = \frac{\Lambda \cdot I_{\mathrm{cell}}}{\dot{V} \cdot c_{\mathrm{in}} \cdot F} \ , \tag{9.2}$$

with $\dot{n}_{\mathrm{ads}}$ being the adsorbed ion flow in $\mathrm{mol\,s^{-1}}$ and c_{in} the molar concentration of the influent. Vice versa, the needed I_{cell} can be calculated for a desired η_{rem}.
Subsequently, the maximum time of desalination $t_{\mathrm{max,ch}}$ can be determined by

$$t_{\mathrm{max,ch}} = \frac{m_{\mathrm{elec}} \cdot \Gamma_{\mathrm{salt},\eta} \cdot F}{\Lambda \cdot I_{\mathrm{cell}} \cdot M_{\mathrm{salt}}} \ , \tag{9.3}$$

which is the time, where the effluent concentration starts increasing. After this point, it rises proportional to the decrease of the electrical current times the current efficiency, which is the same as Λ during constant effluent concentration. The decrease of I is given by the discharge behaviour of a capacitor (Tietze et al., 2015), modified with $t_{\mathrm{max,Ch}}$:

$$I(t) = I_{\mathrm{cell}} \cdot \exp\left(-\frac{t - t_{\mathrm{max,Ch}}}{RC}\right), \ \text{for} \ \ t \geq t_{\mathrm{max,Ch}}, \tag{9.4}$$

whereas RC is the resistor capacitor time constant, which can be determined in a single pass experiment. Thus the further progression of the effluent concentration could be predicted if necessary. It needs to be pointed out that $I(t)$ as in eq. 9.4 is only valid for $t > t_{\mathrm{max,Ch}}$. Thus the original function for capacitor charging needs to be shifted on the t-axis about $t_{\mathrm{max,Ch}}$, by inserting this value with a negative sign behind t in the equation. For $t < t_{\mathrm{max,Ch}}$, $I(t) = I_{\mathrm{cell}}$ is valid.

When I_{cell} and $t_{\mathrm{max,ch}}$ are determined for the desired η_{rem}, the main parameters for the charge phase of an MCDI operation are defined. As it was found that the performance is higher for lower I_{cell} (see fig. 7.8), $\dot{V}$ and thus $\dot{n}_{\mathrm{in}}$ needs to be adjusted to fit for low I_{cell}, in such a way η_{rem} can be reached (eq. 9.2).

For the discharge step, $(t_{\mathrm{DC}} \cdot \dot{V})$ needs to be sufficient to remove the concentrate volume from the module. To discharge the capacitor, Q_{DC} needs to be 5% higher than Q_{C} (see sec. 7.4), thus I_{cell} for the discharge step can be defined with

$$I_{\mathrm{cell,DC}} = 1.05 \cdot \frac{Q_{\mathrm{C}}}{t_{\mathrm{DC}}} \ . \tag{9.5}$$

For energy calculations, $U(t)$ is needed, which is given by charging a capacitor (Tietze et al., 2015), modified with U_{R}.

$$U(t) = U_{\mathrm{cell,max}} \cdot \left(1 - \exp\left(-\frac{t}{RC}\right)\right) + U_{\mathrm{R}}, \ \text{for} \ \ t < t_{\mathrm{max,Ch}}. \tag{9.6}$$

For $t \geq t_{\mathrm{max,Ch}}$, $U(t) = U_{\mathrm{cell,max}}$ is valid. With this constraint, the potential drop due to

external resistances U_{R} can be defined, since $t_{\mathrm{max,Ch}}$ and $U_{\mathrm{cell,max}}$ is known. Subsequently also R_{ext} can be determined with $\frac{\Delta U}{I_{\mathrm{cell}}}$.
The energy used for each phase is

$$E = \Delta t \cdot \bar{U} \cdot I_{\mathrm{cell}} \ , \tag{9.7}$$

whereas $\bar{U}$ is the averaged voltage from eq. 9.6 during Δt for the charge or discharge phase. E is the energy needed for desalination (charge and discharge phases respectively). For real MCDI application, the efficiency of the power supply and energy demand of a water pump need to be included.

Via the equation for water recovery (eq. 2.22), the diluate volume can be calculated and subsequently the SEC for the MCDI operation in used kWh per acquired m^3 of product water.

9.2 Evaluation

This calculation tool was evaluated with CC- and application experiments. As an example a single pass experiment is plotted together with the c_{out}-progression calculated by the model over time and presented in fig. 9.1. The decreasing inlet concentration (grey

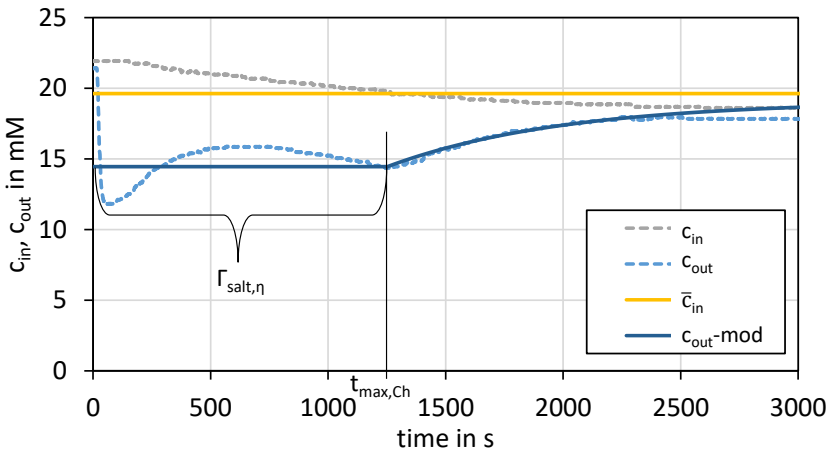

Figure 9.1. c_{in} and c_{out} over time of a CC single pass experiment. Dotted line for the experimental data and solid for the model.

dashed line) was caused by mixing of the effluent with the influent water (see sec. 7.3).

The parallel decreasing outlet concentration (blue dashed line, after $t = 690$ s) indicates a constant desalination with a constant I_{cell}. The modelled outlet concentration (solid blue line) fits for the experimental data except of the overshooting in the beginning of the charge phase, which is compensated by the subsequent lower desalination than estimated. The differences of the useable SAC values and the maximum charge time are $\Delta\Gamma_{\text{salt},\eta} = (7855 - 7253)\ \text{mg g}^{-1} = 602\ \text{mg g}^{-1}$ and $\Delta t_{\text{max,ch}} = (1252 - 1245)\ \text{s} = 7\ \text{s}$, between experiment and model.

The crucial parameters for the calculation tool are Γ_{salt}, η_{SAC} and thus $t_{\text{max,Ch}}$, which need to agree with experimental data.
Γ_{salt} is calculated by the validated $\text{mD}_{2.33}$ model. By comparing experimental data of CC operation with I_{cell} between 10 and 30 A and an inflow concentration of $c_{\text{in}} = 20$ mM, it is analysed if the percentaged usable SAC is remaining constant. Therefore, the values for $\eta_{\text{SAC,C-5}}$ at U_{cell} 1.2 and 1.5 V are listed in tab. 9.1. It is observed that $\eta_{\text{SAC,C-5}}$ is

Table 9.1. Deviation of values for $\eta_{\text{SAC,C-5}}$ to evaluate the calculation tool

U_{cell} in V	1.2	1.5
$\eta_{\text{SAC,C-5}}$	65.0%	61.5%
SD	± 4.3%	± 4.4%

slightly higher for $U_{\text{cell}} = 1.5$ V and both series show almost the same standard deviation of 4.3 and 4.4%, respectively, which is considered small enough to assume $\eta_{\text{SAC,C-5}} = 63\%$ being constant for the calculation model.

With this assumption, the model was compared with other CC single pass experiments. An extraction is shown in fig. 9.2. It can be seen that $t_{\text{max,ch}}$ is varying in between the experiments and does not fit exactly with experimental data. With $\Delta t_{\text{max,ch}} = 111\ \text{s} \pm 76\ s$ (SD) and an averaged $t_{\text{max,ch}} = 811$ s, it is a deviating by 14%. The reason is seen in the first overshooting of c_{out} below the constant desalination mark. The amount which is adsorbed by the electrodes in this time, equals approximately the amount which is missing to reach the calculated $t_{\text{max,ch}}$ and thus removal values are compensated. The differences of removal values are in between ±13%.

Furthermore, the SEC values of the aforementioned single pass experiment and the model data were compared and listed in tab. 9.2. Although the C-5 module possessed a low current efficiency of $\lambda_{\text{current}} = 43\%$, the SEC values were moderate low with $\text{SEC} < 0.5\ \text{kWh m}^{-3}$. It needs to be pointed out that the discharge cycle is not yet

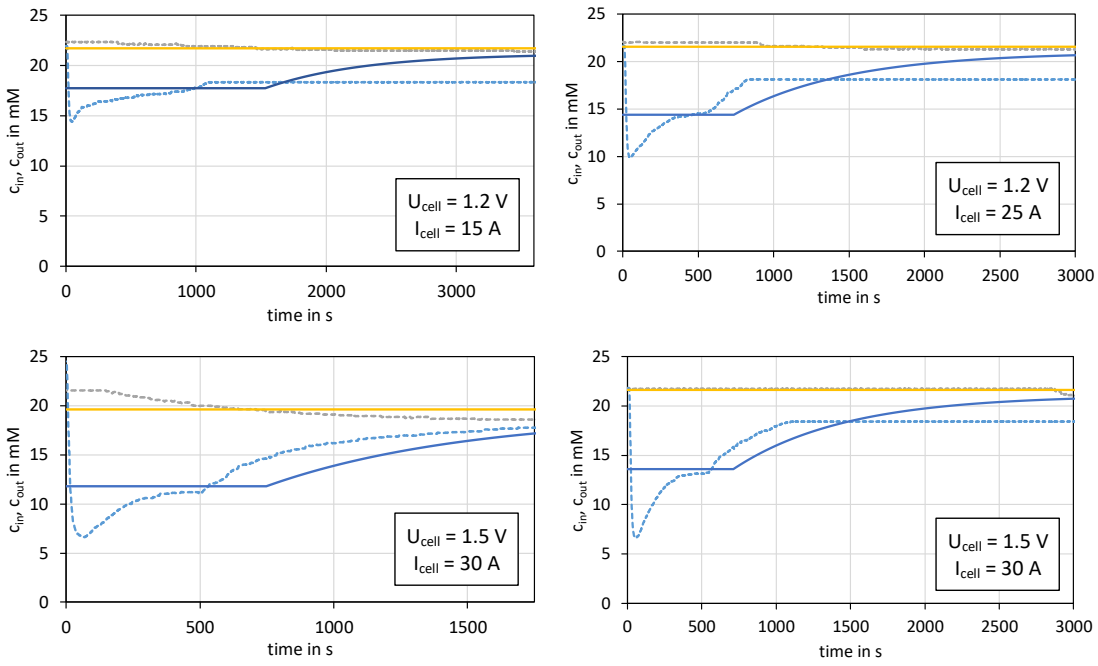

Figure 9.2. Comparison of calculation tool results (solid lines) with experimental data of CC single pass experiments (dotted lines)

considered and thus its energy demand and the resulting water recovery rate. The values of experiments and model are within the same range. The difference follows mainly from the first seconds of desalination, when the U_{cell} in real application is zero, due to potential ion adsorption is given also with $U_{\text{cell}} = 0$ (see point 1 in fig. 7.9). This is not considered in the model.

Furthermore it can be seen that SEC and removal values are more favourable for $t < t_{\max}$, which highlights the importance of knowing $t_{\max}$. Thus also that Γ_{salt}, which derives from the mD model, needs to be modified for real MCDI application. For this reason, the useable SAC $\Gamma_{\text{salt},\eta}$ was defined.

Table 9.2. SEC and removal values of experimental data and model

		$t < t_{\max}$	Whole charge phase
Exp. Data	SEC in kWh m^{-3}	0.294	0.429
	Removal	24%	17%
Model	SEC in kWh m^{-3}	0.348	0.440
	Removal	26%	17%

For all constant current single pass experiments, for $I_{\text{cell}} = 10$ to 30 A, the accuracy of the calculation tool can be determined as listed in tab. 9.3.

Table 9.3. Accuracy of the calculation tool for most important parameters

	Accuracy	**SD**
SEC	75%	7%
Salt removal	87%	6%
$\boldsymbol{t_{\max}}$	86%	9%

An overview of the steps of the calculation tool with in- and output, can be found in fig. 9.3. The inputs are the applied water flow, maximum cell voltage, constant current, mass of electrodes, molar mass of the salt in the feed water and inlet concentration. With the tool, the SEC, salt removal and maximum charge times can be calculated. Future work needs to evaluate the model with bigger MCDI modules (input for m_{elec}) and water quality of monovalent salts (different M_{salt}). Furthermore only the charge cycle was considered. However, with the assumption in eq. 9.5, the energy needed in the discharge cycles can be calculated, which needs to be evaluated in future work.

It can be concluded that

- the developed simplified calculation tool for MCDI applications can be used for quick characterization of operational parameters for MCDI CCCD operation
- for different I_{cell}, maximum U_{cell}, $\dot{V}$ and c_{in}, the SEC, salt removal and maximum charge times can be predicted with an accuracy of 75%, 87% and 86%, respectively
- the resulting SAC of calculation with the mD model is modified to $\Gamma_{\text{salt},\eta}$
- uses RC charging equations in combination with the $\text{mD}_{2.33}$ model, to predict salt removal, optimum phase duration and SEC values for different U_{cell} and inlet concentrations
- material parameters, current efficiency, η_{SAC} and the RC time constant need to be determined empirically beforehand
- effect of overshooting c_{out} needs to be analysed further
- the assumption of a constant RC factor needs to be reconsidered, since different cell concentration affect the resistance (see pos. 4 in tab. 5.4)
- different sizes of modules as well as various water qualities for the feed need to be evaluated in future work.

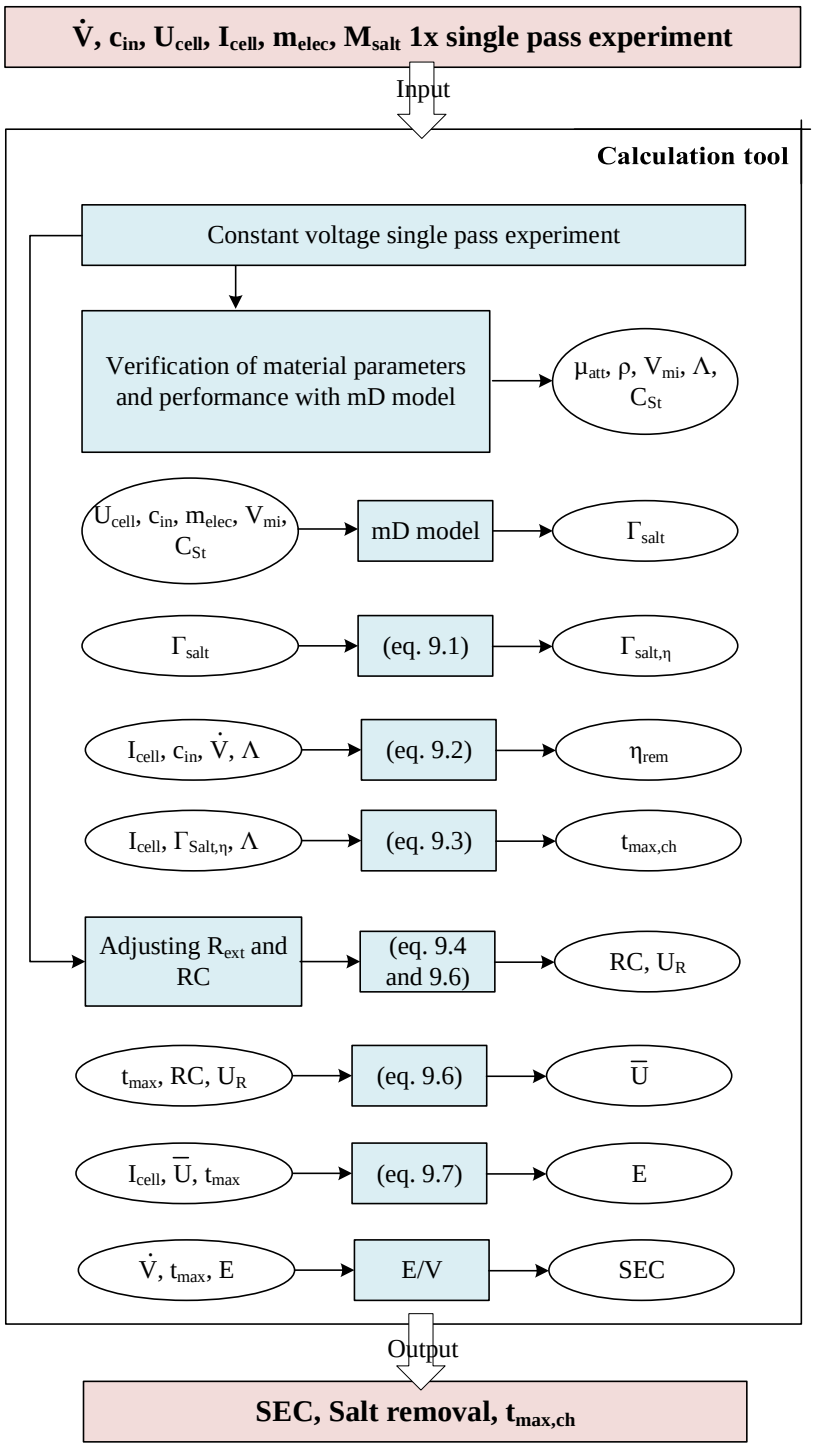

Figure 9.3. Process scheme of the calculation tool with in- and outputs

10 Conclusion and outlook

Research work in literature shows the competitive position of desalination with membrane capacitive deionization. The state-of-the-art of MCDI desalination is experimentally well developed in a laboratory scale using single to only few pairs of electrode cells and there are existing theoretical models, which agree with the salt adsorption capacity or simplified time-dependant ion transport data. To design modular desalination processes including MCDI modules for an out-of-the-lab scale, holistic models are still missing.
In this PhD thesis, the transfer of MCDI operation from laboratory to applied desalination in a commercial scale was considered, regarding the modelling aspect. To develop a calculation tool for system dimensioning and optimizing operational parameters, different state of the art modelling approaches for small scale laboratory set ups have been reviewed, adapted and further developed, to fit larger lab and pilot scale application, producing drinking and irrigation water (production rate above 500 L per day). Hereby, following approaches were used:

- Computational fluid dynamics (CFD) modelling (Navier-Stokes-equations) for determining retention time of salt water between the electrodes
- Nernst-Planck and Poisson equations (NPP) for ion transport
- adapted modified Donnan (mD) model for ion adsorption
- adapted RC model for energy consumption.

To evaluate the models, constant current and constant voltage single-pass experiments with commercial available MCDI modules were carried out, to characterise material input parameters of the model and to evaluate the salt adsorption capacity. Furthermore, application experiments, producing drinking water from saline model water were operated, while optimizing the desalination process concerning removal performance and specific energy consumption, were used to evaluate the calculation tool.
Hereby, the characteristics of cell voltage, electrical current and effluent salt concentration of applied MCDI operation was analysed and optimized. In application tests, drinking water was produced from brackish water with a concentration of $c = 1\ \mathrm{g\,L^{-1}}$,

with an SEC between 0.45 and 0.61 kWh m^{-3}, which is less than published data for RO desalination (Zhao et al., 2013a). Hereby, the typical applied operational limits and modes were pointed out compared to lab scale MCDI desalination. An early cancelling of the charging step needs to be considered if a constant effluent concentration and higher flow efficiency are targeted. This results in an increased water recovery, by adjusting the water flow during the regeneration phase to flush all ions but few water.
The practical experiments further showed that low I_{cell} lead to a higher SAC. This is explained by the longer and more stable ion adsorption, when ion electrosorption is slower. This further requires lower water flows, to achieve the target salt removal.
Additional important observed aspects are the differences to lab scaled CDI cells, which are e.g. the relatively high ion adsorption when no U_{cell} is applied and overshooting effluent concentrations at the beginning of the desalination phase depending on various water flows, which is different compared to the data gathered for small lab scaled cells in literature and needs to be considered for theoretical models for commercial scaled MCDI modules.

The CFD simulation work showed the relation between electrodes distribution, spacer thickness and retention time of the salt water in between the electrodes. It was found that the spacer needs to be thin enough ($\delta_{\text{Sp}} < 1.5$ mm) to ensure an equal distribution of water through the cells.

1D ion transport simulation with the NPP equations could resolve the EDL correctly for different U_{cell}, and the DEBYE-length was in agreement with literature. For calculating an SAC value, area factors are needed.
The 2D simulation with implemented convection term can calculate SAC values with an scaling factor, which fit to Γ_{salt} values of the mD model with $\mu_{\text{att}} = 0$, for $U_{\text{cell}} \leq 0.5$ V.

With CFD and the ion transport equations, one and two dimensional FEM models were developed, which can resolve the electrical double layers at the electrodes correctly and effluent concentrations at the outlet of the MCDI module. The latter was possible after implementing the water flow and its convective influence on the NPP equations as well as the mD model for ion adsorption.
With this model, all operational parameters can be set as input for the model and the salt adsorption capacity as well as time-dependant effluent concentration can be calculated. However, the calculation times are very high (1 to 20 hours for one desalination cycle) and the agreement with experimental data was only valid for $I_{\text{cell}} = 20$ A.

The semi-analytical mD models were used and adapted to fit the SAC values for applied MCDI desalination. Hereby, it was found that for higher cell voltages $U_{\mathrm{cell}} > 1$ V, where applied MCDI is typically operated, the additional excess chemical potential μ_{att} can be assumed constant and does not need to be calculated dependently on the micro pores concentration as in the imD model.
The mD model with $\mu_{\mathrm{att}} = 2.33$ kT was used to fit unknown material parameters and modelled SAC values did agree with experimental data.

Furthermore, a calculation tool including the mD model was developed. Hereby an effective SAC value $\Gamma_{\mathrm{salt},\eta}$ was introduced to adapt the model to applied MCDI desalination operation. With this model, the maximum desalination time can be calculated and salt removal as well as the specific energy demand for desalination cycles can be predicted, for different inlet salt concentrations, cell voltages and module sizes. The accuracy of this calculation tool was 87% (±6% SD) for the salt removal, 86.0% (±9% SD) for maximum desalination times and 75% (±7% SD) for the SEC values.

For future work, it can be pointed out that for the 2D FEM simulation, improvements are needed to fit the model to experimental data, also for different applied electrical currents I_{cell}. Hereby, the equations for the distribution of the electrical potential over the electrodes need to be re-assessed. Furthermore, future computational performance needs to solve the complex equation system in a reasonable calculation time, that the model can be used as a flexible calculation tool.

By finding suitable area / electrode surface factors, the 1D ion transport simulation can predict SAC values. In future work, a study of these factors is needed, so that simple 1D ion transport simulations can be used for MCDI salt removal calculations.

The developed calculation tool agrees with experimental data of commercial scaled MCDI desalination for drinking water production. For the first time its possible to calculate maximum desalination times for different I_{cell}, which is highly important for applied MCDI operation to ensure stable effluent concentrations. The tool was evaluated for a module with electrode sizes of $A_{\mathrm{elec}} = 6.2$ m^2 and a productivity rate to produce drinking water of $V > 400$ L. The model is expected to fit for any upscaled dimension of MCDI plant, since the defining parameter m_{elec} is an input for the tool and when spacer thicknesses δ_{Sp} are set small enough, equal retention times between the electrodes are expected for any water volume flow, as CFD simulations revealed in this thesis. Furthermore, including the mD model, the tool is expected to be valid for $c_{\mathrm{in}} = 5$ to 250 mM as for the imD model, as far $U_{\mathrm{cell}} > 0.8$ V are applied and Λ is measured in

a single pass experiment beforehand (see tab. 4.2). However in future, more tests with pilot- and industrial scale desalination plants have to be carried out, so that the tool with different possible inputs for m_{elec} can be validated with large scale desalination plants as well as with different multivalent salts.

The latter touches on the subject *MCDI for agricultural use*, where the ratio of bivalent ions as Mg^{2+} and Ca^{2+} to Na^{+} (sodium adsorption ratio) is significant for a successful irrigation, as described e.g. in Guyes et al. (2021). In this study, the different adsorption speeds of the different ions is pronounced and how various water flows and constant currents in the charge phase can change the adsorption ratio.
The FEM approaches in this thesis consider the mobility of each ion through the STOKES-EINSTEIN-equation (see eq. 2.14), however the adsorption term of the calculation tool, based on the mD model, does not differ between different valencies. Hence, an evaluation with feed water with a more complex salt matrix and if applicable an adjustment of the tool is needed in future work.

Since MCDI applications typically use pre-treatment steps to minimize total suspended solids (TSS) and total organic carbon (TOC) concentrations, no fouling activity was modelled in this thesis. Nevertheless, long-term applications can lead to blockage of the modules. Thus, a fouling model can be modularly added in future, which can optimize operational parameters to avoid frequent cleaning.

Bibliography

Andres, G.L., Mizugami, T., Yoshihara, Y., 2017. Simulation of an electric behavior of the CDI system. Desalination 419, 211–218. doi:10.1016/j.desal.2017.06.011.

Basser, P.J., Grodzinsky, A.J., 1993. The donnan model derived from microstructure. Biophysical Chemistry 46, 57–68. doi:10.1016/0301-4622(93)87007-j.

Bezerra, M.A., Santelli, R.E., Oliveira, E.P., Villar, L.S., Escaleira, L.A., 2008. Response surface methodology (RSM) as a tool for optimization in analytical chemistry. Talanta 76, 965–977. doi:10.1016/j.talanta.2008.05.019.

Biesheuvel, P., 2015. Activated carbon is an electron-conducting amphoteric ion adsorbent. arXiv:1509.06354 [physics.chem-ph] .

Biesheuvel, P., Zhao, R., Porada, S., van der Wal, A., 2011a. Theory of membrane capacitive deionization including the effect of the electrode pore space. Journal of Colloid and Interface Science 360, 239–248. URL: https://doi.org/10.1016/j.jcis.2011.04.049, doi:10.1016/j.jcis.2011.04.049.

Biesheuvel, P.M., Fu, Y., Bazant, M.Z., 2011b. Diffuse charge and faradaic reactions in porous electrodes. Physical Review E 83, 061507. doi:10.1103/physreve.83.061507.

Biesheuvel, P.M., Porada, S., Levi, M., Bazant, M.Z., 2014. Attractive forces in microporous carbon electrodes for capacitive deionization. Journal of Solid State Electrochemistry 18, 1365–1376. URL: https://doi.org/10.1007/s10008-014-2383-5, doi:10.1007/s10008-014-2383-5.

Boehm, H., 1994. Some aspects of the surface chemistry of carbon blacks and other carbons. Carbon 32, 759–769. doi:10.1016/0008-6223(94)90031-0.

Boeswirth, L., Bschorer, S., 2012. Technische Stroemungslehre (Lehr- und Uebungsbuch). Vieweg+Teubner Verlag, Wiesbaden.

Bohl, W., Elmendorf, W., 2014. Technische Stroemungslehre. Vogel Business Media. URL: https://www.ebook.de/de/product/22097042/willi_bohl_wolfgang_elmendorf_technische_stroemungslehre.html.

Box, G.E.P., Behnken, D.W., 1960. Some new three level designs for the study of quantitative variables. Technometrics 2, 455–475. URL: https://www.tandfonline.com/doi/abs/10.1080/00401706.1960.10489912, doi:10.1080/00401706.1960.10489912.

Butt, H.J., Graf, K., Kappl, M., 2006. Physics and chemistry of interfaces. Physics textbook. 2., rev. and enl. ed. ed., Wiley-VCH, Weinheim. URL: http://www.gbv.de/dms/ilmenau/toc/501422285.PDF. literaturverz. S. [357] - 378IMD-Felder maschinell generiert (GBV).

COMSOL AB, 2017a. CFD Module Users Guide. version: 5.3 ed. COMSOL AB. URL: https://doc.comsol.com/5.3/doc/com.comsol.help.cfd/CFDModuleUsersGuide.pdf.

COMSOL AB, 2017b. COMSOL Multiphysics Reference Manual. version: 5.3 ed. COMSOL AB. URL: https://doc.comsol.com/5.3/doc/com.comsol.help.comsol/COMSOL_ReferenceManual.pdf.

COMSOL AB, 2017c. Introduction to COMSOL Multiphysics. version: 5.3 ed. COMSOL AB. URL: https://cdn.comsol.com/doc/5.3/IntroductionToCOMSOLMultiphysics.pdf.

Corless, R.M., Gonnet, G.H., Hare, D.E.G., Jeffrey, D.J., Knuth, D.E., 1996. On the LambertW function. Advances in Computational Mathematics 5, 329–359. doi:10.1007/bf02124750.

Deschamps, M., Gilbert, E., Azais, P., Raymundo-Piñero, E., Ammar, M.R., Simon, P., Massiot, D., Béguin, F., 2013. Exploring electrolyte organization in supercapacitor electrodes with solid-state NMR. Nature Materials 12, 351–358. doi:10.1038/nmat3567.

Długołęcki, P., van der Wal, A., 2013. Energy recovery in membrane capacitive deionization. Environmental Science & Technology 47, 4904–4910. doi:10.1021/es3053202.

Duval, J., Lyklema, J., Kleijn, J.M., van Leeuwen, H.P., 2001. Amphifunctionally electrified interfaces: coupling of electronic and ionic surface-charging processes. Langmuir 17, 7573–7581. doi:10.1021/la010833i.

Dykstra, J., Keesman, K., Biesheuvel, P., van der Wal, A., 2017. Theory of pH changes in water desalination by capacitive deionization. Water Research 119, 178–186. doi:10.1016/j.watres.2017.04.039.

Dykstra, J., Porada, S., van der Wal, A., Biesheuvel, P., 2018. Energy consumption in capacitive deionization – constant current versus constant voltage operation. Water Research 143, 367–375. doi:10.1016/j.watres.2018.06.034.

Dykstra, J., Zhao, R., Biesheuvel, P., van der Wal, A., 2016. Resistance identification and rational process design in capacitive deionization. Water Research 88, 358–370. URL: https://doi.org/10.1016/j.watres.2015.10.006, doi:10.1016/j.watres.2015.10.006.

Ferzinger, J., Perić, M., 2008. Numerische Stroemungsmechanik. Springer-Verlag Berlin Heidelberg New York, Berlin Heidelberg.

Fritz, P.A., Boom, R., Schroen, K., 2019. Polyelectrolyte-activated carbon composite electrodes for inverted membrane capacitive deionization (iMCDI). Separation and Purification Technology 220, 145–151. doi:10.1016/j.seppur.2019.03.053.

Guyes, E.N., Shocron, A.N., Chen, Y., Diesendruck, C.E., Suss, M.E., 2021. Long-lasting, monovalent-selective capacitive deionization electrodes. npj Clean Water 4. doi:10.1038/s41545-021-00109-2.

Hamann, C.H., Vielstich, W., 2005. Elektrochemie. Wiley-VCH GmbH. URL: https://www.ebook.de/de/product/4008104/carl_h_hamann_wolf_vielstich_elektrochemie.html.

Han, L., Karthikeyan, K., Anderson, M.A., Gregory, K.B., 2014. Exploring the impact of pore size distribution on the performance of carbon electrodes for capacitive deionization. Journal of Colloid and Interface Science 430, 93–99. doi:10.1016/j.jcis.2014.05.015.

Hassanvand, A., Chen, G.Q., Webley, P.A., Kentish, S.E., 2017. Improvement of MCDI operation and design through experiment and modelling: Regeneration with brine and optimum residence time. Desalination 417, 36–51. doi:10.1016/j.desal.2017.05.004.

Hemmatifar, A., Stadermann, M., Santiago, J.G., 2015. Two-dimensional porous electrode model for capacitive deionization. The Journal of Physical Chemistry C 119, 24681–24694. URL: https://doi.org/10.1021/acs.jpcc.5b05847, doi:10.1021/acs.jpcc.5b05847.

Hoinkis, J., 2015. Chemie fuer Ingenieure. Wiley-VCH GmbH. URL: https://www.ebook.de/de/product/23738732/jan_hoinkis_chemie_fuer_ingenieure.html.

Israelachvili, J.N., 2011. Interactions involving polar molecules, in: Intermolecular and Surface Forces. Elsevier, pp. 71–90. doi:10.1016/b978-0-12-375182-9.10004-1.

Jeon, B.G., No, H.C., Lee, J.I., 2011. Development of a two-dimensional coupled-implicit numerical tool for the optimal design of CDI electrodes. Desalination 274, 226–236. URL: https://doi.org/10.1016/j.desal.2011.02.021, doi:10.1016/j.desal.2011.02.021.

Jeon, S.I., Park, H.R., Yeo, J.G., Yang, S.C., Cho, C.H., Han, M.H., Kim, D.K., 2013. Desalination via a new membrane capacitive deionization process utilizing flow-electrodes. Energy & Environmental Science 6, 1471. doi:10.1039/c3ee24443a.

Jeong, K., Yoon, N., Park, S., Son, M., Lee, J., Park, J., Cho, K.H., 2020. Optimization of a nanofiltration and membrane capacitive deionization (NF-MCDI) hybrid system: Experimental and modeling studies. Desalination 493, 114658. doi:10.1016/j.desal.2020.114658.

Kastening, B., 1988. Properties of slurry electrodes from activated carbon powder. Berichte der Bunsengesellschaft fuer physikalische Chemie 92, 1399–1402. doi:10.1002/bbpc.198800334.

Kastening, B., Heins, M., 2005. Properties of electrolytes in the micropores of activated carbon. Electrochimica Acta 50, 2487–2498. doi:10.1016/j.electacta.2004.10.077.

Lado, J.J., Cartolano, V., García-Quismondo, E., García, G., Almonacid, I., Senatore, V., Naddeo, V., Palma, J., Anderson, M.A., 2021. Performance analysis of a capacitive deionization stack for brackish water desalination. Desalination 501, 114912. doi:10.1016/j.desal.2020.114912.

Laurien, E., Oertel, H., 2018. Numerische Stroemungsmechanik. Springer Fachmedien Wiesbaden. doi:10.1007/978-3-658-21060-1.

Lecheler, S., 2009. Numerische Stroemungsberechnung; Schneller Einstieg durch ausfuehrliche praxisrelevante Beispiele. Vieweg + Teubner, Wiesbaden.

Lee, J., Kim, S., Yoon, J., 2017. Rocking chair desalination battery based on prussian blue electrodes. ACS Omega 2, 1653–1659. doi:10.1021/acsomega.6b00526.

Li, M., Park, H.G., 2018. Pseudocapacitive coating for effective capacitive deionization. ACS Applied Materials & Interfaces 10, 2442–2450. doi:10.1021/acsami.7b14643.

Maex, R., 2014. Nernst-planck equation, in: Encyclopedia of Computational Neuroscience. Springer New York, pp. 1–7. doi:10.1007/978-1-4614-7320-6_233-1.

Montes-Morán, M., Suárez, D., Menéndez, J., Fuente, E., 2004. On the nature of basic sites on carbon surfaces: an overview. Carbon 42, 1219–1225. doi:10.1016/j.carbon.2004.01.023.

Munz, C.D., Westermann, T., 2012. Numerische Behandlung gewoehnlicher und partieller Differenzialgleichungen. Springer Berlin Heidelberg. doi:10.1007/978-3-642-24335-6.

Naguib, M., Mochalin, V.N., Barsoum, M.W., Gogotsi, Y., 2013. 25th anniversary article: MXenes: A new family of two-dimensional materials. Advanced Materials 26, 992–1005. doi:10.1002/adma.201304138.

Pasta, M., Wessells, C.D., Cui, Y., Mantia, F.L., 2012. A desalination battery. Nano Letters 12, 839–843. doi:10.1021/nl203889e.

Pawlowski, S., Sistat, P., Crespo, J.G., Velizarov, S., 2014. Mass transfer in reverse electrodialysis: Flow entrance effects and diffusion boundary layer thickness. Journal of Membrane Science 471, 72–83. doi:10.1016/j.memsci.2014.07.075.

Porada, S., Borchardt, L., Oschatz, M., Bryjak, M., Atchison, J.S., Keesman, K.J., Kaskel, S., Biesheuvel, P.M., Presser, V., 2013. Direct prediction of the desalination performance of porous carbon electrodes for capacitive deionization. Energy & Environmental Science 6, 3700. doi:10.1039/c3ee42209g.

Porada, S., Weinstein, L., Dash, R., van der Wal, A., Bryjak, M., Gogotsi, Y., Biesheuvel, P., 2012. Water desalination using capacitive deionization with microporous carbon electrodes. ACS Applied Materials & Interfaces 4, 1194–1199. URL: https://doi.org/10.1021/am201683j, doi:10.1021/am201683j.

Porada, S., Zhang, L., Dykstra, J., 2020. Energy consumption in membrane capacitive deionization and comparison with reverse osmosis. Desalination 488, 114383. doi:10.1016/j.desal.2020.114383.

Probstein, R.F., 1994. Physicochemical Hydrodynamics. John Wiley & Sons, Inc. doi:10.1002/0471725137.

Qu, Y., Campbell, P.G., Gu, L., Knipe, J.M., Dzenitis, E., Santiago, J.G., Stadermann, M., 2016. Energy consumption analysis of constant voltage and constant current operations in capacitive deionization. Desalination 400, 18–24. doi:10.1016/j.desal.2016.09.014.

Ramachandran, A., Hemmatifar, A., Hawks, S.A., Stadermann, M., Santiago, J.G., 2018. Self similarities in desalination dynamics and performance using capacitive deionization. Water Research 140, 323–334. doi:10.1016/j.watres.2018.04.042.

Ramachandran, A., Oyarzun, D.I., Hawks, S.A., Stadermann, M., Santiago, J.G., 2019. High water recovery and improved thermodynamic efficiency for capacitive deionization using variable flowrate operation. Water Research 155, 76–85. doi:10.1016/j.watres.2019.02.007.

Rautenbach, R., 1997. Membranverfahren Grundlagen der Modul- und Anlagenauslegung. Springer, BerlinHeidelbergNew YorkBarcelonaBudapestHongkongLondonMailandParisSanta ClaraSingapurTokio.

Schlichting, H., Gersten, K., 2006. Grenzschicht-Theorie. Springer-Verlag GmbH. URL: https://www.ebook.de/de/product/3128211/herrmann_schlichting_klaus_gersten_grenzschicht_theorie.html.

Srimuk, P., Kaasik, F., Kruener, B., Tolosa, A., Fleischmann, S., Jaeckel, N., Tekeli, M.C., Aslan, M., Suss, M.E., Presser, V., 2016. MXene as a novel intercalation-type pseudocapacitive cathode and anode for capacitive deionization. Journal of Materials Chemistry A 4, 18265–18271. doi:10.1039/c6ta07833h.

Stoeckli, F., Centeno, T., 2005. On the determination of surface areas in activated carbons. Carbon 43, 1184–1190. doi:10.1016/j.carbon.2004.12.010.

Suss, M.E., Baumann, T.F., Worsley, M.A., Rose, K.A., Jaramillo, T.F., Stadermann, M., Santiago, J.G., 2013. Impedance-based study of capacitive porous carbon electrodes with hierarchical and bimodal porosity. Journal of Power Sources 241, 266–273. doi:10.1016/j.jpowsour.2013.03.178.

Suss, M.E., Porada, S., Sun, X., Biesheuvel, P.M., Yoon, J., Presser, V., 2015. Water desalination via capacitive deionization: what is it and what can we expect from it? Energy Environ. Sci. 8, 2296–2319. URL: https://doi.org/10.1039/c5ee00519a, doi:10.1039/c5ee00519a.

Tanaka, Y., 2015a. Electrodialysis, in: Progress in Filtration and Separation. Elsevier, pp. 207–284. doi:10.1016/b978-0-12-384746-1.00006-9.

Tanaka, Y., 2015b. Preparation of ion exchange membranes, in: Ion Exchange Membranes. Elsevier, pp. 3–28. doi:10.1016/b978-0-444-63319-4.00001-8.

Tietze, U., Schenk, C., Gamm, E., 2015. Electronic Circuits. Springer-Verlag GmbH. URL: https://www.ebook.de/de/product/25535233/ulrich_tietze_christoph_schenk_eberhard_gamm_electronic_circuits.html.

Tsouris, C., Mayes, R., Kiggans, J., Sharma, K., Yiacoumi, S., DePaoli, D., Dai, S., 2011. Mesoporous carbon for capacitive deionization of saline water. Environmental Science & Technology 45, 10243–10249. doi:10.1021/es201551e.

UNESCO, 2006. Water : a shared responsibility. United Nations Educational, Scientific and Cultural Organization (UNESCO) Berghahn Books, Paris, France and New York, U.S.A.

UN: The General Assembly, 2015. Transforming our world: the 2030 agenda for sustainable development. Resolution A/RES/70/01 17th session. URL: https://www.un.org/en/development/desa/population/migration/generalassembly/docs/globalcompact/A_RES_70_1_E.pdf.

VDI-Gesellschaft, 2013. VDI-Waermeatlas. Springer Berlin Heidelberg. doi:10.1007/978-3-642-19981-3.

Vogel, C., Meier-Haack, J., 2014. Preparation of ion-exchange materials and membranes. Desalination 342, 156–174. doi:10.1016/j.desal.2013.12.039.

Voltea Inc., 2021. Capdi case studies. URL: https://voltea.com/resources/. accessed on: 17-05-2021.

Walton, N.R., 1989. Electrical conductivity and total dissolved solids—what is their precise relationship? Desalination 72, 275–292. doi:10.1016/0011-9164(89)80012-8.

Wang, L., Biesheuvel, P., Lin, S., 2018a. Reversible thermodynamic cycle analysis for capacitive deionization with modified donnan model. Journal of Colloid and Interface Science 512, 522–528. doi:10.1016/j.jcis.2017.10.060.

Wang, T., Su, D., Shanmukaraj, D., Rojo, T., Armand, M., Wang, G., 2018b. Electrode materials for sodium-ion batteries: Considerations on crystal structures and sodium storage mechanisms. Electrochemical Energy Reviews 1, 200–237. doi:10.1007/s41918-018-0009-9.

Westermann, T., 2010. Modellbildung und Simulation. Springer Berlin Heidelberg. doi:10.1007/978-3-642-05461-7.

WHO, 2017. Guidelines for drinking-water quality. World Health Organization, Geneva. URL: https://www.who.int/publications/i/item/9789241549950.

Zhang, C., He, D., Ma, J., Tang, W., Waite, T.D., 2018. Faradaic reactions in capacitive deionization (CDI) - problems and possibilities: A review. Water Research 128, 314–330. doi:10.1016/j.watres.2017.10.024.

Zhao, R., Biesheuvel, P., Miedema, H., Bruning, H., van der Wal, A., 2010. Charge efficiency: A functional tool to probe the double-layer structure inside of porous electrodes and application in the modeling of capacitive deionization. The Journal of Physical Chemistry Letters 1, 205–210. doi:10.1021/jz900154h.

Zhao, R., Biesheuvel, P.M., van der Wal, A., 2012. Energy consumption and constant current operation in membrane capacitive deionization. Energy & Environmental Science 5, 9520. doi:10.1039/c2ee21737f.

Zhao, R., Porada, S., Biesheuvel, P., van der Wal, A., 2013a. Energy consumption in membrane capacitive deionization for different water recoveries and flow rates, and comparison with reverse osmosis. Desalination 330, 35–41. URL: https://doi.org/10.1016/j.desal.2013.08.017, doi:10.1016/j.desal.2013.08.017.

Zhao, X., Wei, H., Zhao, H., Wang, Y., Tang, N., 2020. Electrode materials for capacitive deionization: A review. Journal of Electroanalytical Chemistry 873, 114416. doi:10.1016/j.jelechem.2020.114416.

Zhao, Y., Wang, Y., Wang, R., Wu, Y., Xu, S., Wang, J., 2013b. Performance comparison and energy consumption analysis of capacitive deionization and membrane capacitive deionization processes. Desalination 324, 127–133. URL: https://doi.org/10.1016/j.desal.2013.06.009, doi:10.1016/j.desal.2013.06.009.

Nomenclature

Abbreviations

Ω	Calculation domain
0VC	Zero voltage charge
0VD	Zero voltage discharge
AEM	Anion exchange membrane
amD	Amphoteric modified DONNAN model
BC	Boundary condtition
C	Concentrate phase
CC	Constant current
CCCD	Constant current charge and discharge
CDI	Capacitive deionization
CEM	Cation exchange membrane
COMSOL	*COMSOL Multiphysics™ v5.6*
CPU	Central processing unit
CV	Constant voltage
CVCD	Constant voltage charge and discharge
D	-dimensional
DAE	Differntial algebraic equation -interface
DK	Development kit
ECI	Electrostatic-Interface
EDLC	Electrostatic double layer capacitors
eq.	Equation
FBV	FRUMKIN-BUTLER-VOLMER
FCDI	Flow capacitive deionization
FEM	Finite element method
fig.	Figure
GCS	GOUY-CHAPMAN-STERN (model)
glEQ	Global ODEs and DAEs -interface

gPDE	General Form PDE-Interface
HC	Half cycle
IEM	Ion exchange membrane
imD	Improved modified DONNAN model
MCDI	Membrane capacitive deionization
mD	Modified DONNAN model
MF	Microfiltration
NF	Nanofiltration
NPP	NERNST-PLANCK-POISSON
NR	Not recorded
ODE	Ordinary differential equation -interface
P	Purify phase
PDE	Partial differential equation
POeq	Poisson Equation-Interface
PP	Pre-purify phase
RAM	Random-access memory
RC	Resistor-capacitor
Ref	Reference
RO	Reverse osmosis
RSM	Response surface methodology
rV	Reversed voltage
SAC	Salt adsorption capacity
SD	Standard deviation
SDM	Solution-diffusion model
sec.	Section
SHE	Standard hydrogen electrode
SPF	Single Phase Flow-Interface
tab.	Table
TDS	Total dissolved solids
TOC	Total organic carbon
TSA	Total salt adsorption
TSS	Total suspended solids
UF	Ultrafiltration
Z	Impedance

Greek variables

α	Charge dependence of STERN capacitance	$F\,m^3\,mol^{-2}$
δ	Thickness	m
δ_v	Wall layer thickness	m
ϵ	Permittivity	-
ϵ	Turbulance dissipation rate (in sec. 3.3.2)	-
η	Efficiency	-
η	Viscosity (in sec. 2.1)	$kg\ m^{-1}\ s^{-1}$, $N\ s\ m^{-2}$
η_{rem}	Salt removal	-
η_{SAC}	Percentaged usable amount of the salt adsorption capacity	-
η_{vol}	Water recovery	-
γ	Volumetric amount	-
Γ_{salt}	Salt adsorption capacity	$mg\,g^{-1}$
κ	Electrical conductivity	$mS\,cm^{-1}$
Λ	Charge efficiency	-
λ	Heat coefficient	$W\ m^{-2}\ K^{-1}$
λ_D	DEBYE length	m
$\lambda_{current}$	Current efficiency	-
λ_B	BJERRUM length	m
μ	Chemical potential	-
ν	Kinematic viscosity (in sec. 2.2)	$m^2\ s^{-1}$
ω	Membrane charge sign	-
ϕ	Electrical potential	V
π	Osmotic pressure	bar
ρ	Density	$kg\ m^{-3}$
Σ	Specific charge	$C\ g^{-1}$
σ	Charge density	$C\ m^{-3}$
$\tau_{xx}, \tau_{yy}, \tau_{zz}$	Normal stress	Pa, $kg\ m^{-1}\ s^{-2}$
$\tau_{xy}, \tau_{xz}, \tau_{yz}$	Shear stress	Pa, $kg\ m^{-1}\ s^{-2}$
ξ_m	Molar conductivity	$cm^2\ \Omega^{-1}\ mol^{-1}$

Indices

∞	Bulk
T	Thermal
$x,\ y,\ z$	x-, y-, z-direction

AC	Active carbon
att	Attractive
c	Concentrate
chem	Chemical
conc	Concentrate
crit	Critical
D	DONNAN
dil	Diluate
elchem	Electrochemical
ext	External
f	Feed
i	Ion species
init	Initial
j	Amphoteric region
M	Membrane
max	Maximum
mi	Micropore
min	Minimum
mod	Module
mol	Molar
NaCl	Sodium chloride
O	Oxidized
p	Permeate
PS	Power supply
R	Reduced
rect	Rectangular
rm	Ramp
s	Salt
sat	Saturated
St	STERN
tot	Total
vol	Volumetric
W	Water
We	Water electrolysis

Latin variables

Δm_s	Total salt adsorption	g
$\dot{m}$	Mass flow	kg s^{-1}
$\dot{n}$	Molar flow	mol s^{-1}
$\dot{V}$	Volume flow	m^3 s^{-1}
$\vec{n}$	Normal vector	-
$\vec{p}$	Impulse	N s, kg m s^{-1}
A	Area	m^2
A_E	External area of active carbon electrode	m^2
A_M	Membrane area	m^2
b	Width	m
C	Capacity	F
c	Concentration	g L^{-1}, mol m^{-3}
$C_\mathrm{St,0}$	STERN capacity in zero charge	F mL^{-1}
$C_\mathrm{St,vol}$	Volumetric STERN capacity	F mL^{-1}
D	Diffusion coefficient	m^2 s^{-1}
E	Electrical field (in sec. 2.1)	V m^{-1}
E	Energy	J, kWh
e	Specific energy (in sec. 3.3.2)	J kg^{-1}
E°	Standard electrode potential	V
e_0	Elementary charge	$1.6022 \cdot 10^{-19}$ C
E_att	Micropore ion correlation energy	kT mol m^{-3}
F	Faraday constant	96485.3 C mol^{-1}
f	Frequency	s^{-1}
g	Gravitational accelaration	9.81 m s^{-1}
h	Height	m
I	Electrical current	A
J_F	Faradaic current	m s^{-1}
J_mass	Mass flux	kg A^{-1} s^{-1}
J_mol	Molar flux	mol A^{-1} s^{-1}
K	Conductivity-concentration conversion factor	-
K	Electrostatic attraction force (in sec. 2.1.2)	N
k	Kinetic energy of turbulence (in sec. 3.3.2)	J kg^{-1}
k_b	Boltzmann constant	$1.381 \cdot 10^{-23}$ J K^{-1}
k_O , k_R	Kinetic oxidation-, reduction rate	m s^{-1}

L	Hydraulic diameter	m
M	Molar mass	g mol^{-1}
m	Mass	kg
n	Amount of substance	mol
n_{me}	Amount of mesh elements	-
p	Porosity	-
p	Pressure (in sec. 2 and 3)	Pa, bar
Q	Electrical charge	C
Q	Heat (in sec. 3.3.2)	J
q	Charge of ion	C
q	Specific heat (in sec. 3.3.2)	J kg^{-1}
R	Electrical resistance (in sec. 4)	Ω
R	Universal gas constant	8.314 J K^{-1} mol^{-1}
r_1	Ion radius	m
Re	Reynolds number	-
S_{E}	External specific area of active carbon material	m^2 g^{-1}
SEC	Specific energy consumption	kWh m^{-3}
T	Temperature	K
t	time	s
U	Voltage	V
u	Ion mobility	m^2 V^{-1} s^{-1}
u	Velocity fraction (in sec. 3.3.2)	m s^{-1}
V	Volume	m^3
v	Velocity	m s^{-1}
v	Velocity fraction (in sec. 3.3.2)	m s^{-1}
W	Work, power	J
w	Velocity fraction (in sec. 3.3.2)	m s^{-1}
X	Membrane capacity	m m^{-3}
x	Spacial coordinate	-, m
y	Spacial coordinate	-, m
y^+	Characteristic wall coordinate	-
z	Spacial coordinate (in sec. 3.3.2)	-, m
z	Valency	-

Appendices

A Datasheet: C-modules from Voltea Inc.

MODULES

From the Inside-Out

The composition of Voltea's CapDI Modules is the **game-changing** piece of our patented technology. Our modules are comprised of electrode stacks, where ion removal takes place by means of an electric field.

Our modules operate on a range of flows and feed water salinities, allowing implementation into a host of applications. Simple electrical terminals and water connections allow easy installation and service.

The composition of our smallest and pilot-testing Development Kit (DK) Systems include a Custom Module or VS-Series Module, while our largest Industrial Series (IS) Systems include our Industrial Series (IS) Modules, shown here. Our DiUse PoU Systems couple with the DiUse Module, and the DiEntry Module is used in our DiEntry PoE Systems.

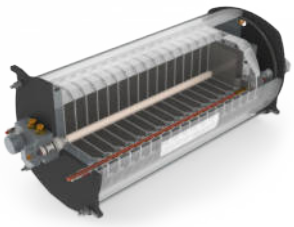

IS Module (Internal Views)

Voltea's Innovative Modules

There are four module sizes for Voltea's Systems, all depending on flow rate, feed salinity and targeted purified water quality. These modules have a different number of electrode "stacks" in each configuration.

CapDI System Modules are configured for both high temperature and ambient temperature applications.

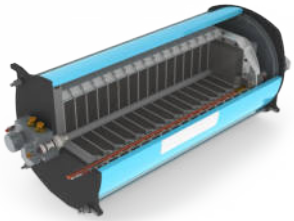

IS Module (Internal View)

Custom Module

DiUse Module

DiEntry Module

IS Module

CapDI MODULE TECH SPECS

Module	Custom	DiUse	DiEntry	IS
Length	28 cm (11”)			
Width	28 cm (11”)			
Height	32 cm (13”)	35 cm (14”)	53 cm (21”)	70 cm (28”)
Weight	20 kg (44 lbs)	25 kg (55 lbs)	50 kg (110 lbs)	60 kg (132 lbs)
Feed Inlet Coupling	1/2” union	3/8” push fit	1/2” push fit	1/2” union
Product Outlet Coupling	1/2” union	3/8” push fit	1/2” push fit	1/2” union
Electrical Connections	2 x M8 fine threaded copper rods			
	Operational Requirements			
Instant Flow Rate*	0,2 - 5 L/min (0.05 - 1.3 gpm)	0,4 - 6,3 L/min (0.1 - 1.7 gpm)	1,2 - 15 L/min (0.3 - 4 gpm)	0,1 - 1,3 m^3/hr (0.4 - 5.8 gpm)
Net Produced Flow*	0,1 - 3 L/min (0.03 - 0.8 gpm)	0,2 - 4 L/min (0.05 - 1.1 gpm)	0,8 - 12 L/min (0.2 - 3.2 gpm)	0,1 - 0,8 m^3/hr (0.4 - 3.5 gpm)
Maximum Pressure	10 bar (145 PSI)			
Water Temperature	5 - 60 °C (40 - 140 °F)			

**Flows are unimpeded and may be limited by system specs. Ranges modeled on 320 ppm TDS at 50% removal.*

B Datasheet: Development Kit (DK) from Voltea Inc.

CapDI©

Voltea CapDI
Membrane Capacitive Deionization

We specialize in tunable water purification that is designed to remove total dissolved salts (TDS) from a variety of water sources, ranging from tap water and brackish groundwater to industrial process water. CapDI achieves this at a lower economic cost and reduced environmental impact than any other available technology.

Voltea's CapDI technology purifies water types ranging from residential consumer appliances to large-scale industrial plants. Our systems are modular, allowing easy expansion to meet any increased water demands.

CapDI Benefits

- Automated cleaning
- Remote monitoring available
- High water recovery, up to 90 %
- Tunable TDS reduction, up to 90 %
- Complete system monitoring and feedback
- Dynamic Control - controlled output water quality
- Customizable system sizing to reach client needs
- Operation at high temperatures, up to 60 °C (140 °F)
- Low energy usage, 0,4 - 0,8 kWh/m^3 (1.5 - 3.0 kWh/kgal)
- Patented Membrane Capacitive Deionization Technology

Quality Assurance

- CE Certified
- UL on request
- Factory Acceptance Test on request
- Systems and modules quality control tested
- Voltea Remote Monitoring and Control package

Feed Water Quality

PARAMETER	UNIT	RANGE	INTERMITTENT
Removal Limit	Δppm	0 - 2000	
Total Dissolved Solids (TDS)	ppm	0 - 4000	
Total Organic Carbon	ppm	< 15	
Chemical Oxygen Demand	ppm	< 50	< 100
Turbidity	NTU	< 4	< 100
Fats, Oils, Greases	ppm	< 0.5	
Total Suspended Solids (TSS)	ppm	< 4	< 20
Free Chlorine	ppm	< 1	< 25
pH	-	2 - 10	1 - 12
Iron total	ppm	< 0.5	
Total Hardness ($CaCO_3$)*	ppm	< 1000	
M Alkalinity (as $CaCO_3$)*	ppm	< 1000	
Pre-filtration	µm	5	
Temperature	°C	1 - 60	
Chemicals	-	Contact Voltea	

* Limits depend on set TDS reduction and water recovery

WWW.VOLTEA.COM

DK

CapDI DK System Development Kit

Design and Scope of Supply

- Two 5 µm filters
- CapDI DK User Manual
- Laptop control and monitoring software
- On-site installation and training package
- Reduced size industrial or appliance design CapDI Modules
- Built-in monitoring; flow, pressure, conductivity, module voltage, current

DK Features

- In-line 10" slim-line filter housing
- Laptop with intuitive control program
- System monitoring and data recording
- Data analysis and calculation templates

In/Out Conductivity Meters	0 - 10 mS/cm
Total Flow Meter	0 - 10 L/min (0.1 - 2.6 gpm)
System Pressure	0 - 2,5 bar (0 - 36 PSI)
Module Voltage	0 - 3 V
Module Current	0 - 240 A

Performance	Flow Rate Capacity*	0,2 - 2,5 L/min (0.1 - 0.7 gpm)
	Salt Removal	25 - 90 %
	Water Recovery	40 - 90 %
System Specification	System Power Requirements	Single - Phase (110 - 240 V AC / 50 - 60 Hz)
	System Dimensions (L x W x H)	75 x 50 x 60 cm (2'6" x 1'8" x 1'11")
	Service Space	0,8 m (2'7") from edge of system
	Weight**	52 kg (114 lbs)
	Feed Inlet Coupling	10 mm tubing push-in connection
	Product Outlet Coupling	10 mm tubing push-in connection
	Power Output to Modules	(Low Range: 1 - 60 A / 0 - 10 V DC) (High Range: 5 - 240 A / 0 - 3 V DC)
	Compatible Modules	(Low Range: VS-1, VS-2, Custom) (High Range: Custom)
System Requirements	Water Feed***	Test barrel
	Water Temperature***	1 - 60 °C (34 - 140 °F)
	Operating Ambient Air Temperature****	< 35 °C (< 95 °F)
Inputs/ Outputs	Control	Voltea laptop control program
	Data Output	txt. file format for Voltea analysis template

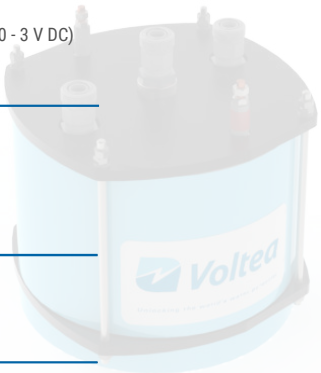

*Actual performance will depend on module used and settings
**Weight without modules
***Please contact Voltea if unavailable
****If higher than this, additional cooling may be required